Studies on Confined Guest Molecules by ^{2}H and DNP enhanced ^{13}C solid-state NMR

Untersuchungen an eingeschlossenen Gastmolekülen mittels ^{2}H und DNP verstärkter ^{13}C Festkörper-NMR Spektroskopie

Zur Erlangung des Grades eines Doktors der Naturwissenschaften (Dr. rer. nat.)
Genehmigte Dissertation von Sonja Carina Döller aus Aschaffenburg
Tag der Einreichung: 02. November 2023, Tag der Prüfung: 22. Januar 2024

1. Gutachten: Prof. Dr. Gerd Buntkowsky
2. Gutachten: apl. Prof. Dr. Torsten Gutmann
3. Gutachten: Prof. Dr. Ralf Ludwig

Darmstadt, Technische Universität Darmstadt

TECHNISCHE UNIVERSITÄT DARMSTADT

Fachbereich Chemie
Eduard-Zintl-Institut für Anorganische und Physikalische Chemie
Arbeitsgruppe Prof. Buntkowsky

Studies on Confined Guest Molecules by ^{2}H and DNP enhanced ^{13}C solid-state NMR
Untersuchungen an eingeschlossenen Gastmolekülen mittels ^{2}H und DNP verstärkter ^{13}C Festkörper-NMR Spektroskopie

Accepted doctoral thesis by Sonja Carina Döller

Date of submission: 02. November 2023
Date of thesis defense: 22. Januar 2024

Darmstadt, Technische Universität Darmstadt

Bitte zitieren Sie dieses Dokument als:
URN: urn:nbn:de:tuda-tuprints-265810
URL: http://tuprints.ulb.tu-darmstadt.de/26581
Jahr der Veröffentlichung auf TUprints: 2024

Dieses Dokument wird bereitgestellt von tuprints,
E-Publishing-Service der TU Darmstadt
http://tuprints.ulb.tu-darmstadt.de
tuprints@ulb.tu-darmstadt.de

Die Veröffentlichung ist urheberrechtlich geschützt
https://rightsstatements.org/page/InC/1.0/

Courage is resistance to fear, mastery of fear, and not the absence of fear.

Mark Twain

Erklärungen laut Promotionsordnung

§ 8 Abs. 1 lit. c PromO

Ich versichere hiermit, dass die elektronische Version meiner Dissertation mit der schriftlichen Version übereinstimmt.

§ 8 Abs. 1 lit. d PromO

Ich versichere hiermit, dass zu einem vorherigen Zeitpunkt noch keine Promotion versucht wurde. In diesem Fall sind nähere Angaben über Zeitpunkt, Hochschule, Dissertationsthema und Ergebnis dieses Versuchs mitzuteilen.

§ 9 Abs. 1 PromO

Ich versichere hiermit, dass die vorliegende Dissertation selbstständig und nur unter Verwendung der angegebenen Quellen verfasst wurde.

§ 9 Abs. 2 PromO

Die Arbeit hat bisher noch nicht zu Prüfungszwecken gedient.

Darmstadt, 02. November 2023

Sonja Carina Döller

List of Publications

Parts of this work have been published previously:

Scientific publications as first author

1. S. C. Döller, M. Brodrecht, T. Gutmann, M. Hoffmann and G. Buntkowsky, Deuterium NMR Studies of the Solid–Liquid Phase Transition of Octanol-d_{17} Confined in SBA-15. *J. Phys. Chem. C*, **2021**, *127*, 12125–12134. DOI: 10.1021/acs.jpcc.1c05873.
2. S. C. Döller, T. Gutmann, M. Hoffmann and G. Buntkowsky, A Case Study on the Influence of Hydrophilicity on the Signal Enhancement by Dynamic Nuclear Polarization. *Solid State Nucl. Magn. Reson.*, **2022**, *122*, 101829–101837. DOI: 10.1016/j.ssnmr.2022.101829.
3. S. C. Döller, M. Brodrecht, T. Gutmann, M. Hoffmann and G. Buntkowsky, Direct and Indirect DNP NMR Uncovers the Interplay of Surfactants with Their Mesoporous Host Material. *J. Phys. Chem. C*, **2023**, *127*, 12125–12134. DOI: 10.1021/acs.jpcc.3c01946.

Scientific publications from collaborations

4. N. B. Haro Mares, M. Brodrecht, T. Wissel, S. C. Döller, L. Rösler, H. Breitzke, M. M. Hoffmann, T. Gutmann and G. Buntkowsky, Influence of APTES-Decorated Mesoporous Silica on the Dynamics of Ethylene Glycol Molecules - Insights from Variable Temperature ^{2}H Solid-State NMR. *J. Phys. Chem. C*, **2023**, *127*, 19735–19746.

Review articles

5. G. Buntkowsky, S. C. Döller, N. B. Haro Mares, T. Gutmann and M. Hoffmann, Solid-State NMR Studies of Non-Ionic Surfactants Confined in Mesoporous Silica. *Z. Phys. Chem.*, **2022**, *127*, 939–960.

Conference contributions

6. S. C. Döller, M. Brodrecht, M. Hoffmann and G. Buntkowsky, Deuterium NMR Studies of Octanol-d_{17} Confined in SBA-15 at Low Temperatures and Around Its Melting Point. 42nd FGMR Annual Discussion Meeting, online. *Book of Abstracts*, **2021**.
7. S. C. Döller, M. Brodrecht, M. Hoffmann and G. Buntkowsky, Deuterium NMR Studies of the Solid-Liquid Phase Transition of a Nonionic Model Surfactant Confined in the Pores of Mesoporous Silica. AMPERE NMR School in Zakopane, Poland. *Book of Abstracts*, **2022**.
8. N. B. Haro Mares, M. Brodrecht, S. C. Döller, L. Rösler, H. Breitzke, T. Gutmann, M. Hoffmann and G. Buntkowsky, Study of Motions in Ethylene Glycol Confined in SBA-15 at low Temperatures via ^{2}H Solid State NMR. AMPERE NMR School in Zakopane, Poland. *Book of Abstracts*, **2022**.
9. S. C. Döller, M. Hoffmann and G. Buntkowsky, Uncovering the Dynamics of Surfactants – A Combined ^{2}H and DNP NMR Approach. EUROMAR in Utrecht, The Netherlands. *Book of Abstracts*, **2022**.

Danksagung

Das Anfertigen einer Dissertation ist eine monumentale Unternehmung, welche ohne die Unterstützung zahlloser Menschen niemals gelungen wäre.

An erster Stelle möchte ich mich bei Prof. Dr. Gerd Buntkowsky für die Möglichkeit bedanken, in seiner Gruppe meine Doktorarbeit anzufertigen. Vielen Dank dafür, dass du mir dieses sehr interessante Thema anvertraut hast. Durch dein in mich gelegtes Vertrauen und die daraus resultierenden Freiräume konnte ich dieses Thema zu meinem eigenen machen.

Außerdem möchte ich mich bei apl. Prof. Dr. Torsten Gutmann für seine Geduld bei der Einarbeitung in das für mich neue Spektrometer und sein ständiges Bemühen, alle aufkommenden Fragen zu beantworten, bedanken. Ohne deine Unterstützung hätte die Lösung einiger Fragestellungen wahrscheinlich signifikant mehr Zeit verschlungen. Danke für viele konstruktive Diskussionen, unzählige Stunden technischer Unterstützung, für zahlreiche Beschleuniger auf unseren Arbeitskreiswanderungen und natürlich für die Bereitschaft, die Aufgabe des Zweitgutachters zu übernehmen.

Prof. Markus Hoffmann danke ich für die kontinuierlich erfreuliche und erfolgreiche Zusammenarbeit. Danke auch für die Möglichkeit, dich in Brockport zu besuchen, für die herzliche Aufnahme in deiner Famile während meiner Zeit dort, für die sehr interessante Einführung in die DOSY NMR und für das Korrekturlesen dieser Arbeit. Danke an dieser Stelle auch an die State University Brockport dafür, dass ich ihre Labore nutzen durfte.

Vielen Dank an Dr. Hergen Breitzke für die technische Unterstützung in den zahllosen Fällen, in denen das Gerät mal wieder nicht das getan hat, was es sollte. Danke auch für deinen Wahlspruch in diesen Momenten: Keine Panik, keine Hektik. Was jetzt kaputt ist, ist später auch noch kaputt.

Dr. Martin Brodrecht und Till Wissel danke ich sowohl für die Synthese des in dieser Arbeit verwendeten hochporösen Silicas als auch für die Beantwortung jeglicher Fragen, welche zu diesen Materialien aufgekommen sind.

Als nächstes möchte ich mich bei Dr. Laura Wienands, Jonas Lins, Mark Höfler und Franziska Theiß für die sehr gute Atmosphäre im Büro D209 bedanken. Ob es fachliche Diskussionen bezüglich der spezialisiertesten NMR- oder DNP-relatierten Probleme oder Aktivitäten nach Feierabend waren, es hat mir jeden Tag Freude bereitet, für diese ins Büro zu kommen.

Auch meinen Kollegen Felix Dietrich, Jan Kergaßner, Edina Šić, Bingyu Zang, Dr. Yuliya Miloslavina und Dr. Millena Lograd dos Santos sowie allen ehemaligen Mitgliedern der Gruppe möchte ich für die angenehme Arbeitsatmosphäre danken. Spezieller Dank gilt außerdem meiner Kollegin Nadia Berenice Haro Mares für die gute Zusammenarbeit auf unserem gemeinsamen Projekt.

Danke auch an alle, die mich während meines Studiums begleitet haben. Ohne euch hätte es weniger entspannte Abende, weniger Hochdrucklernen im Lernzentrum und weniger gemeinsames Hoffen und Beten nach Klausuren gegeben. Auch wenn sich unsere Wege teilweise getrennt haben, bin ich um jede Bekanntschaft und Freundschaft froh, die ich während des Studiums machen bzw. schließen durfte.

Abschließend möchte ich mich bei meinen Freunden und meinem Partner bedanken. Ohne euch alle wäre die anstrengende Studienzeit nicht vorstellbar gewesen. Danke, dass ich mit euch Erfolge feiern und Rückschläge verarbeiten durfte.

Zu guter Letzt vielen Dank an meine Eltern. Sie haben mein naturwissenschaftliches Interesse von Anfang an gefördert und mir das Studium der Chemie erst ermöglicht. Danke!

Zusammenfassung

Die Transformation der chemischen Industrie zu nachhaltigeren Forschungs- und Produktionsmethoden ist eines der größten Vorhaben des laufenden Jahrhunderts. Ein wichtiger Ansatz, um diesen Wandel zu ermöglichen, ist die Verwendung nachhaltiger und ungiftiger Lösungsmittelsysteme.

In der vorliegenden Arbeit wurden die Wechselwirkungen von Analytmolekülen mit Oberflächen mit Hilfe festkörperkernspinresonanzspektroskopischer Methoden untersucht. Der Schwerpunkt lag dabei auf Polyethylenglycolen und deren amphiphilen Derivaten. Diese amphiphilen Derivate können als Tenside eingesetzt werden und ermöglichen so die Durchführung von Reaktionen in wässrigen Medien durch Bildung kleiner, lipophiler Mikro- oder Nanoreaktoren. Polyethylenglycole selbst eignen sich als nicht flüchtige und ungiftige Ersatzstoffe für herkömmliche organische Lösungsmittel.

Die Polyethylenglycole sowie die Tenside *n*-Octanol, Triton-X 100 und Hexaethylenglycolmonodecylether wurden sowohl pur als auch im Kontakt mit mesoporösen Siliziumdioxidmaterialien untersucht. Die Wechselwirkungen von Molekülen wie Tensiden mit festen Grenzflächen sind noch nicht ausreichend erforscht, da ihre Untersuchung mit den üblichen spektroskopischen Methoden schwierig ist. ^{2}H Festkörper-NMR Spektroskopie sowie mit dynamischer Kernpolarisation (DNP) verstärkte ^{13}C Festkörper-NMR Spektroskopie wurden eingesetzt, um die Wechselwirkungen der Moleküle untereinander und mit der Siliciumdioxidoberfläche zu analysieren. Zusätzlich zu den regulären DNP verstärkten spektroskopischen Methoden wurde auch direkte und indirekte DNP NMR Spektroskopie angewandt.

n-Octanol, eingeschlossen in SBA-15, wurde als Modellsystem für komplexere Tenside sowie zur Nachahmung biologischer Membranen verwendet. Durch die Analyse der ^{2}H-NMR-Spektren, die sowohl aus dem Bulk als auch aus dem eingeschlossenen System gewonnen wurden, konnte die Ausrichtung von *n*-Octanol in der mesoporösen Silika SBA-15 aufgeklärt werden. Darüber hinaus wurde das Schmelzverhalten der Octanolphase in den Poren durch dynamische Differenzkalorimetriemessungen dokumentiert. Dies führte zu der Feststellung, dass trotz des Einschlusses der Moleküle in den Poren und des daraus resultierenden begrenzten Platzangebots keine Glasbildung stattfindet. Stattdessen bilden sich Kristallite, die aufgrund der Wechselwirkungen mit den Porenwänden unterschiedliche Größen und damit unterschiedliche Schmelztemperaturen aufweisen, was zu einem allmählichen Schmelzprozess führt.

n-Octanol wurde auch als Modellsystem für die Entwicklung eines neuen Ansatzes zur Analyse von Daten aus NMR-Spektren verwendet, die durch direkte/indirekte DNP verstärkt wurden. Vier verschiedene handelsübliche Radikale (AMUPol, TOTAPOL, bTbK und AsymPol) wurden in Verbindung mit *n*-Octanol

verwendet, um zu klären, wie sich die Polarisation in der Probe ausbreitet. Mit dem neu entwickelten Ansatz konnten die erhaltenen Spektren quantitativ ausgewertet werden. Dies war bisher aufgrund des notwendigen Vergleichs verschiedener Proben mit möglicherweise variablen Radikalkonzentrationen oder Probenmengen nur eingeschränkt möglich. So konnte gezeigt werden, dass die Hydrophilie ein Schlüsselfaktor dafür ist, wie die in der DNP NMR Spektroskopie verwendeten Radikale mit den Analytmolekülen wechselwirken und wie die Polarisation übertragen wird. Diese Ergebnisse illustrieren, dass die Wahl des Polarisationsmittels eine wesentliche Rolle bei der Sicherstellung eines optimalen Polarisationstransfers und damit der maximal möglichen Hyperpolarisation des beobachteten Kerns bei DNP-verstärkten NMR Messungen spielt.

Mit Hilfe der direkten/indirekten DNP und unter Anwendung des neu entwickelten Analyseansatzes wurden anschließend die Anordnungen von Polyethylenglycolen sowie von Tensiden in zwei verschiedenen mesoporösen Silikaten untersucht. Auch der mögliche Einfluss der Porengröße auf das Verhalten der Analytmoleküle sollte betrachtet werden. Es konnte gezeigt werden, dass im Bereich der untersuchten Porenradien diese keinen Einfluss auf das Verhalten des Analyten haben. Dennoch konnte durch quantitative Analyse dokumentiert werden, dass die amphiphilen Tenside im Vergleich zu den hydrophilen Polyethylenglycolen unterschiedliche Anordnungen in den Poren der Silikamaterialien bevorzugen. Die Tenside richten sich mit ihren hydrophilen Kopfgruppen in Richtung der Porenwände aus. Das hydrophile Radikal AMUPol wurde ebenfalls entlang der Porenwand lokalisiert. Die Polyethylenglycole hingegen zeigen einen höheren Vermischungsgrad mit dem verwendeten Radikal und ein Knäuelverhalten aufgrund intramolekularer Wechselwirkungen, was zu einer gleichmäßigen Übertragung der Polarisation über alle Kohlenstoffatome führt.

Die Ergebnisse dieser Arbeit zeigen, dass die Konkurrenz der intra- und intermolekularen Wechselwirkungen mit denjenigen an der entsprechenden Oberfläche das Verhalten der eingeschlossenen Moleküle stark beeinflusst. Dies ist von großer Bedeutung für eine Vielzahl von Systemen an Fest-Flüssig-Grenzflächen, wie z. B. heterogene Katalysatoren, chromatographische Anwendungen oder *drug delivery* Systeme. Darüber hinaus wird die Anwendbarkeit der direkten/indirekten DNP NMR Spektroskopie auf Systeme an der Fest-Flüssig-Grenzfläche erweitert und die Vergleichbarkeit der erhaltenen Spektren durch einen neuartigen Ansatz zur Quantifizierung der Daten erheblich verbessert.

Abstract

The transformation of the chemical industry towards more sustainable methods of research and manufacturing is one of the largest undertaking of the current century. One key approach to enable this transformation is the utilization of sustainable and non-toxic solvent systems.

In the present work, the interactions of analyte molecules with surfaces were investigated by means of solid-state Nuclear Magnetic Resonance (ssNMR) spectroscopic methods. The focus was laid on polyethylene glycols and their amphiphilic derivatives. These amphiphilic derivatives can be utilized as surfactants and thus allow reactions to be conducted in aqueous media by forming small, lipophilic micro- or nanoreactors. Polyethylene glycols themselves are suitable as non-volatile and non-toxic substitutes for conventional organic solvents.

The polyethylene glycols as well as the surfactants *n*-octanol, Triton-X 100 and hexaethylene glycol monodecyl ether were investigated both in bulk and in contact with mesoporous silica materials. The interactions of molecules such as surfactants with solid interfaces are not sufficiently understood since their study is challenging with standard spectroscopic methods. Solid-state ^{2}H NMR spectroscopy as well as solid-state ^{13}C NMR spectroscopy enhanced by Dynamic Nuclear Polarization (DNP) were used to analyze the interactions of the molecules with each other as well as with the silica surface. In addition to regular spectroscopic methods enhanced by DNP, direct and indirect DNP NMR spectroscopy was also applied.

n-Octanol confined in SBA-15 was used as a model system for more complex surfactants as well as to emulate biological membranes. By analyzing the ^{2}H NMR spectra obtained from the bulk as well as the confined system, the alignment of *n*-octanol in the mesoporous silica SBA-15 could be elucidated. In addition, the melting behavior of the octanol phase in the pores was documented by differential scanning calorimetry (DSC) measurements. This lead to the determination that glass formation does not occur despite the confinement of the molecules within the pores and the resulting limited space available. Instead, crystallites are formed, which show various sizes and thus different melting temperatures due to the interactions with the pore walls, causing a gradual melting process.

n-Octanol was also used as a model system for the development of a new approach to analyze data obtained from NMR spectra enhanced by direct/indirect DNP. Four different commercially available radicals (AMUPol, TOTAPOL, bTbK and AsymPol) were analyzed in *n*-octanol to elucidate how the polarization spreads through the sample. Using the newly developed approach, the spectra obtained could be evaluated quantitatively. This was previously possible only to a limited extent due to the necessary comparison of

different samples with potentially variable radical concentrations or sample quantities. It could thus be shown that hydrophilicity is a key factor in how radicals used in DNP NMR spectroscopy interact with analyte molecules and how polarization is transferred. These findings illustrate that the choice of polarizing agent plays an essential role in ensuring an optimal polarization transfer and therefore the maximum amount of enhancement possible for DNP enhanced NMR measurements.

With the help of direct/indirect DNP and through applying the newly developed analytical method, the arrangements of polyethylene glycols as well as of surfactants in two different mesoporous silicates were subsequently investigated. The potential influence of the pore size on the behavior of the analyte molecules was to be tested as well. However, such an influence could not be observed. Nevertheless, by quantitative analysis, it was possible to document that the amphiphilic surfactants prefer different arrangements in the pores of the silica materials compared to the hydrophilic polyethylene glycols. The surfactants align themselves with their hydrophilic head groups in the direction of the pore walls. The hydrophilic radical AMUPol was localized along the pore wall as well. The polyethylene glycols, on the other hand, show a higher degree of mixing with the radical used and a tendency to coil due to intramolecular interactions, which leads to the uniform transfer of the polarization across all carbon atoms.

The findings of this work illustrate that the competition of the intra- and intermolecular interactions with those at the corresponding surface strongly influences the behavior of the confined molecules. This is of high relevance for a plethora of systems at the solid-liquid interface like heterogeneous catalysts, chromatographic applications or drug delivery systems. In addition, the applicability of direct/indirect DNP NMR spectroscopy to systems at the solid-liquid interface is expanded and the comparability of the obtained spectra is greatly improved through a novel approach to quantification of the data.

Contents

1 Introduction

The inception of industrial-scale chemical processes has allowed for significant economic evolution over the past 150 years. However, due to the intrinsic nature of many processes and chemicals, it has also lead to problems like environmental pollution and waste management issues. Additionally, many commodity chemicals are derived from a petroleum-based value chain, making their production not sustainable.[1]

To tackle these challenges and to provide a reliable framework for future chemists and chemical engineers, the twelve principles of Green Chemistry were developed by Anastas and Warner in 1998.[2] In addition to specifications concerning waste prevention, atom economy and the utilization of renewable feedstocks, they contain proposals concerning the reduction of toxicity of all utilized chemicals by means of less-toxic replacements. As solvents account for approximately 50 – 80 % of the mass in a typical chemical reaction,[3] making the switch to non-toxic and renewable solvents is a key step towards establishing more sustainable processes.

Alternatives like supercritical fluids or ionic liquids have been proposed, all with unique advantages and drawbacks. For more information on these systems, reference is made to the literature.[4,5]

As water is abundant, cheap and non-toxic, it has been of interest as a sustainable solvent for over thirty years.[6] However, a plethora of molecules of major interest are lipophilic organic molecules, restricting the applicability of water as a solvent due to their limited solubility. One potential way to face this challenge is the inclusion of surface active agents (surfactants) in the reaction mixture. The surfactants form micelles above their critical micellar concentration, establishing lipophilic environments in the otherwise aqueous medium.[7] These so-called micro- or nanoreactors allow for the implementation of many reactions which would otherwise be conducted in organic solvents. This includes, for example, reactions like nucleophilic aromatic substitutions,[8] cross-coupling reactions,[9–11] metathesis reactions,[12,13] aldol reactions[14] or the formation of amides and peptides.[15,16] The nature of the surfactant can be tuned to the individual requirements of the desired reaction. Additionally, many surfactants can be produced starting from sustainable resources.[17]

For systems incompatible with water due to potential decomposition, low molecular mass polyethylene glycols (PEGs) have been of continuous interest. PEGs are non-volatile, limiting the exposure of the operator to chemicals, non-toxic, non-flammable and have remarkable solvation properties.[18] PEGs are able to solvate metal cations similar to crown ethers, allowing for their application as phase transfer

catalysts[19,20] and show a high solubility of salts like KI, KNO_3, CH_3COOK, KCN or $K_2Cr_2O_7$.[21,22] Additionally, PEGs are capable of acting as solvents for many organic molecules, allowing for reactions like nucleophilic substitutions,[23–25] Diels-Alder-reactions,[23] cross-coupling reactions[26] and oxidation or reduction reactions.[21,27–29]

Besides the utilization of inherently less dangerous and polluting chemicals, the prevention of waste and the application of selective catalysis are fundamental principles of Green Chemistry which go hand in hand.[2] Catalysts allow for new, efficient pathways to products of chemical reactions, often reducing unwanted by-products and therefore circumventing the need for their disposal.[30] As homogeneous catalysts generally achieve higher activities and selectivities, they play an important role in the synthesis of fine chemicals and pharmaceuticals.[31] However, most homogeneous catalysts feature a heavy metal ion at their center and rely on ligands to stabilize the catalytically active species, most of which are synthetically difficult to access and therefore expensive. In addition, homogeneous catalysts are difficult to recycle as they are usually removed from the reaction mixture in subsequent purification steps and discarded instead of recovered.[30] A possible solution to these issues is the immobilization of homogeneous catalysts on insoluble support materials like cellulose,[31] polymer resins[32] or porous silica materials,[33] within polymers[34] or on the walls of reactors.[35] This greatly increases the ease of recovery for these catalytic systems as they can be separated from the reaction mixture by mechanical processes like filtration or centrifugation, allowing for the reuse of the catalysts.

Especially porous silicas are versatile support materials for otherwise homogeneous catalytic systems. They are thermally as well as chemically stable, allowing for their use under most reaction conditions.[36] The size of the silica particles, their pore size along with their surface area and the properties of the pore walls themselves can all be fine-tuned by controlling the parameters during their synthesis.[37] This means that a plethora of catalysts can be supported by silica materials, enabling countless different reactions.[38]

Despite the benefits that the immobilization catalysts on support materials can bring, new challenges also arise. In contrast to the homogeneous case, the interactions of the substrate and the solvent with the support material have to be taken into account for heterogeneous catalysts in addition to those between the substrate and the active centers.[39] To probe these interactions, various characterization methods like Raman,[40] infrared,[41] UV-Vis[42] and fluorescence spectroscopy[43] as well as X-ray[44] and neutron-scattering-based techniques[45] are available. However, these techniques do not necessarily enable the observation of sorbates and of support materials on a molecular level and often suffer from background issues caused by the (amorphous) bulk support material.[46]

Nuclear Magnetic Resonance (NMR) based techniques have become established methods to study these systems. This includes the added benefit that NMR techniques are able to monitor dynamic processes like phase transitions or the activation of potential non-translational degrees of freedom like librations or rotations.[47] This is usually achieved through ^2H ssNMR,[48,49] relaxation time measurements[50,51] or NMR diffusometry.[52]

To counteract the low sensitivity of NMR spectroscopy, hyperpolarization techniques like dynamic nuclear polarization (DNP) are commonly employed in the solid state. The application of DNP enhanced ssNMR additionally allows for the observation of molecular dynamics through the introduction of direct and indirect DNP enhanced ssNMR.[53–57] This technique enables the selective observation of highly mobile groups, like rotating methyl groups, which facilitates spectral assignments in crowded spectra[55] and allows for the further elucidation of host-guest interactions at the solid-liquid interface.[48]

The main focus of this work was the investigation of solvents and surfactants relevant for green chemistry in combination with mesoporous host systems, namely the periodic mesoporous silica (PMS) materials Santa Barbara Amorphous 15[58] (SBA-15) and Mobil Composition of Matter 41 (MCM-41).[59] Both PMS exhibit highly ordered hexagonal pores with tuneable pore sizes. They are both routinely applied as molecular sieves,[60] in drug-delivery,[61] or as catalyst support material,[62] making them suitable model host materials.

As guest molecules, PEGs as well as surfactants of the type C_nE_m were chosen. This class of surfactants features a lipophilic group consisting of aliphatic or aromatic hydrocarbons C_n and a polar moiety composed of ethylene glycol units of variable length E_m which is attached through an ether bond. In the PEG family, PEG 200, meaning a PEG with an average molecular mass of 200 g mol^{-1}, as well as pentaethylene glycol were investigated in order to probe potential influences of polydispersity on the sorption properties of PEGs. As surfactants, three model substances were chosen. Hexaethylene glycol monodecyl ether ($C_{10}E_6$) was selected as representative of the class of aliphatic surfactants, Triton X-100 (Triton) was chosen as aromatic surfactant and *n*-octanol was utilized as exemplary surfactant of the type C_8E_0.

To understand these molecules' properties and their sorption behavior in PMS, they were investigated utilizing ssNMR techniques. Two different methods were thereby applied. ^{2}H ssNMR served as a probe for local dynamics within the individual surfactant molecule while DNP enhanced ^{13}C ssNMR aided in elucidating the conformation of the molecules within the mesopores as well as in revealing the interactions of the polarizing agents with the surfactants.

The following two chapters will provide an overview over the methods and concepts applied in this work. A key focus is placed on NMR spectroscopic methods. Furthermore, the technique of DNP enhanced NMR spectroscopy is introduced and its primary theoretical background is presented. Subsequently, the specialized method of direct/indirect DNP employed in this study is established. The results of the investigations performed are presented thereafter, and finally, a summary and an outlook on future projects are outlined.

2 Nuclear Magnetic Resonance

Ever since its introduction by Edward Mills Purcell and Felix Bloch in 1945 and 1946 respectively,[63,64] nuclear magnetic resonance (NMR) spectroscopy has been a powerful analytical tool, indispensable to the modern chemist. From the routine applications of liquid-phase NMR spectroscopy for structure or purity determinations[65] to the more complex methods enabling applications such as the investigation of dynamics,[66] the analysis of protein structures,[67,68] the detection of chemical exchange,[69] the determination of molecular conformations[70] as well as the documentation of aging processes of battery cells,[71] NMR spectroscopy is applied. As a diagnostic tool in clinical research and daily practice, magnetic resonance imaging (MRI) allows for the non-invasive visualization of tissues like the brain,[72] the lungs[73] or various malign grows[72–75] in addition to the possibility of following processes within the body in real time.[76] As there is excellent literature on the topic of the physical basics of NMR spectroscopy,[77–81] they are only briefly presented here. The following chapters will focus on an overview of the concepts and techniques relevant to this work.

2.1 Principles of Nuclear Magnetic Resonance Spectroscopy

NMR spectroscopy relies on the fact that most nuclei possess an angular momentum, the spin I ($I_{^1\mathrm{H}} = \frac{1}{2}$, $I_{^2\mathrm{H}} = 1$, $I_{^{13}\mathrm{C}} = \frac{1}{2}$). This spin state is 2I+1-fold degenerate under standard conditions. However, when the nucleus is brought into a suitably large magnetic field B_0, the degeneracy is broken. This leads to the inception of different nuclear spin energy levels as shown in Figure 2.1. Each level is described by the corresponding spin magnetic quantum number m_I, with m_I = -I, -I+1,..., I-1, I. The energy of each level can be calculated according to eq. 2.1.

$$E = -\hbar\gamma B_0 m_\mathrm{I} \tag{2.1}$$

The gyromagnetic ratio γ is a nucleus-dependent factor describing the ratio of its magnetic moment μ to its spin I. The energy difference ΔE between these levels is called nuclear Zeeman splitting[82] and is field-dependent according to eq. 2.2.

$$\Delta E = \hbar\gamma B_0 \text{ or } \Delta E = \hbar\omega_0 \tag{2.2}$$

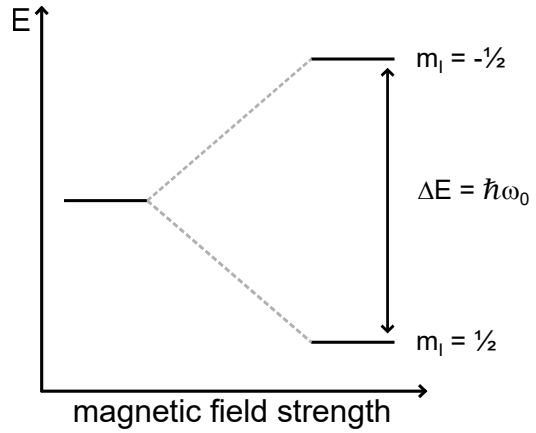

Figure 2.1: Visualization of the nuclear Zeeman effect[82] for a nucleus with $I = \frac{1}{2}$. The Zeeman effect leads to a splitting of otherwise degenerate nuclear spin states in a suitably big magnetic field.

The nuclear spins precess around the B_0 field axis (the z-axis, by convention) with the nuclear Larmor frequency ω_0. The direction in which the spin processes is dependent on the sign of γ. In order to induce transitions between the different nuclear spin levels, radio frequency pulses must be radiated onto the sample according to the resonance condition (eq. 2.3). These transitions can occur in both directions, leading to either absorption or stimulated emission of a photon.

$$\omega_0 = \gamma B_0 \tag{2.3}$$

The angle with which a spin precesses around B_0 is not constant; it fluctuates due to small fluctuating fields in the spin's environment. However, due to the external magnetic field, this wandering motion is not completely isotropic as it is slightly more probable for the nuclear spin to adopt a low-energy orientation. This leads to a slight excess of spin orientations with magnetic moments parallel to B_0.

In thermal equilibrium, the sum of these nuclei's magnetic moments leads to a small net longitudinal magnetization M_z of the sample. However, this longitudinal spin magnetization is significantly smaller than the sample's typical diamagnetism caused by the electrons. Hence, nuclear longitudinal magnetization is usually not studied.

Instead, the longitudinal magnetization is deflected from its initial position around B_0 through irradiation of the sample with RF pulses according to eq. 2.3, leading to x- and y-components of the magnetization. Since the spins keep precessing, this transverse magnetization also precesses around B_0. As a rotating magnetic moment generates a rotating magnetic field, an oscillating electric current is induced in the NMR coil by this transverse magnetization. The oscillating current is detected as a function of time, resulting in the free-induction decay (FID). Through a subsequent Fourier transform[83] from the time- to the frequency-domain, the NMR spectrum is obtained.

2.2 Relaxation Time Constants

If an ensemble of spins is transferred out of the thermal equilibrium (e.g. by a RF pulse), the spin ensemble will start relaxing back into its equilibrium state once the source of the excitation is halted. In NMR spectroscopy, two main relaxation processes are of relevance: First of all, the re-establishing of the equilibrium magnetization, called spin-lattice or longitudinal relaxation; secondly, the loss of phase coherence of the ensemble of spins caused by fluctuating microscopic magnetic fields around the spins, named spin-spin or transversal relaxation. Both of these processes are characterized by distinctive relaxation time constants, T_1 and T_2 respectively.[77] As these time constants are dependent on the interactions of the observed nuclei with each other and their environment, they differ significantly for liquid and solid samples. For liquids, T_1 is in the order of milliseconds to minutes, with T_2 usually being of a similar length. In solids, T_1 can range from seconds to hours, while T_2 is significantly shortened by the fluctuating microscopic magnetic fields around the spins in the sample caused by its pronounced anisotropy, leading to T_2 values as short as microseconds.[84,85]

Since a plethora of information can be obtained from the investigation of the relaxation time constants,[77] a number of NMR experiments have been developed to measure them. For the determination of the longitudinal relaxation time, saturation recovery experiments are usually employed in the solid state. Established in 1974,[86] they allow for the determination of T_1 time constants independent of the line width of the investigated signal. The pulse sequence of a standard saturation recovery experiment features an initial train of 90° RF pulses, thus eliminating any longitudinal magnetization M_z. Subsequently, the system is given a period of time τ to equilibrate, after which the accrued magnetization is read out with another 90° RF pulse (compare Figure 2.2a). τ is incremented, leading to a set of spectra acquired for different evolution times. Utilizing equation 2.4, the value for T_1 can then be determined for each nucleus of interest.

$$M_{z_t} = M_{z_0} \cdot \left[1 - e^{-\frac{\tau}{T_1}}\right] \tag{2.4}$$

For the determination of T_2 time constants, a Hahn echo experiment is usually applied.[87,88] In this type of experiment, a 90° RF pulse is first applied to the sample, flipping the vector of the magnetization into the *xy*-plane, leading to transversal M_{xy} magnetization. Afterwards, the system is allowed to evolve during a period of time τ, which leads to a dephasing of the spins due to local field inhomogeneities. Subsequently, a 180° RF pulse is applied, leading to a refocusing of the spins and thereby to the creation of an echo, which is observed after another period of τ (compare Figure 2.2b).

The incrementation of τ leads to a set of spectra with a gradually decreasing echo amplitude. Using equation 2.5, the T_2 time constant can then be determined.

$$M_{\mathrm{xy_t}} = M_{\mathrm{xy_0}} \cdot e^{-\frac{\tau}{T_2}} \tag{2.5}$$

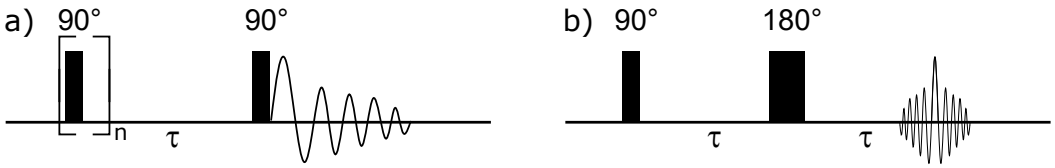

Figure 2.2: Standard pulse sequences used to investigate relaxation time constants. a) Saturation recovery pulse sequence consisting of a pulse train of 90°-pulses and a subsequent 90°-pulse to read out the built-up magnetization. The saturation recovery pulse sequence is used to determine T_1. b) Spin echo pulse sequence comprising a 90°-pulse and a successive 180°-pulse to refocus the magnetization. An echo formation is observed 2τ after the first pulse. This pulse sequence enables the determination of T_2.

2.3 Deuterium NMR Spectroscopy

2.3.1 The Quadrupolar Interaction

Most NMR active nuclei in the periodic table (> 75 %) have a spin quantum number $I > \frac{1}{2}$ and therefore are quadrupolar nuclei.[89] While $I = \frac{1}{2}$ nuclei have a symmetric charge distribution, quadrupolar nuclei like ^{2}H display an asymmetric charge distribution (See Figure 2.3).

The quadrupole moment eQ is given as charge times area, with e representing the elementary charge and Q determining the shape of the asymmetric charge distribution. Q is a characteristic value for each nucleus. Depending on its value, the nucleus may be dubbed cigar-shaped (compare Figure 2.3a) or disc-shaped (Figure 2.3b).

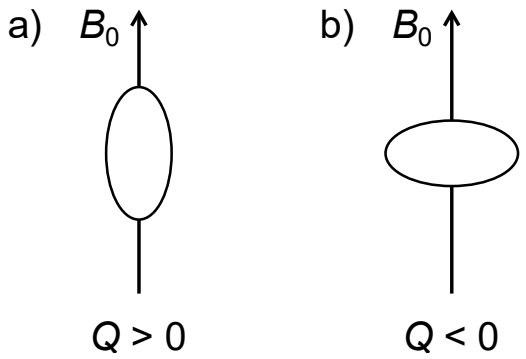

Figure 2.3: Schematic illustration of the charge distribution for a quadrupolar nucleus with a) Q > 0 and b) Q < 0.

The quadrupolar moment of the nucleus interacts with the local electric field gradient (EFG) which is a property of the local electronic environment. In order to quantify the interaction of the nucleus with the largest component of the EFG tensor $\tilde{\mathbf{V}}$, V_{ZZ}, the quadrupolar coupling constant C_{Q} is used, as defined by equation 2.6. Additionally, the asymmetry parameter η is defined as the deviation from axial symmetry of the EFG, utilizing the other tensor compounds of $\tilde{\mathbf{V}}$, V_{XX} and V_{YY} (equation 2.7).[90] η is defined between 0 and 1.

$$C_{\mathrm{Q}} = \frac{eQV_{\mathrm{ZZ}}}{h} \tag{2.6}$$

$$\eta = \frac{V_{\mathrm{XX}} - V_{\mathrm{YY}}}{V_{\mathrm{ZZ}}} \text{ with } V_{\mathrm{ZZ}} > V_{\mathrm{YY}} > V_{\mathrm{XX}} \tag{2.7}$$

Due to the quadrupolar interaction, the splitting of the energy levels of the nucleus caused by the Zeeman interaction is perturbed. This leads to a shift in the energy levels, as shown in Figure 2.4a for ^{2}H, the

nucleus of interest in this work. As ^{2}H only shows a first-order quadrupolar interaction, the second-order quadrupolar interaction will not be described here. Due to the shifted energy levels, two different symmetrical signals with the modified frequencies $\omega_0 \pm \omega_Q$ can be distinguished in the spectrum around the initial Larmor frequency ω_0. Indeed, for a single crystal, only these two signals are observed for each magnetically nonequivalent site (compare Figure 2.4b). For powders, a characteristic Pake pattern[91] is observed, consisting of the contributions of the statistically distributed crystallites and their relationship to B_0 as described by the angle θ (compare Figure 2.4c and d). By observing the distance of the two singularities (in a Pake pattern with a small η value) or by measuring the distance between the signals (in a single crystal aligned along Q_{zz}), C_Q can be determined. For signals corresponding to strongly asymmetrical $\tilde{\mathbf{V}}$, a numerical simulation of the data can be necessary in order to determine C_Q. For a full analytical description of the influence of the quadrupolar interaction on the energy levels of the nucleus, as well as for information on second-order quadrupolar interactions, reference is made to the literature.[92–95]

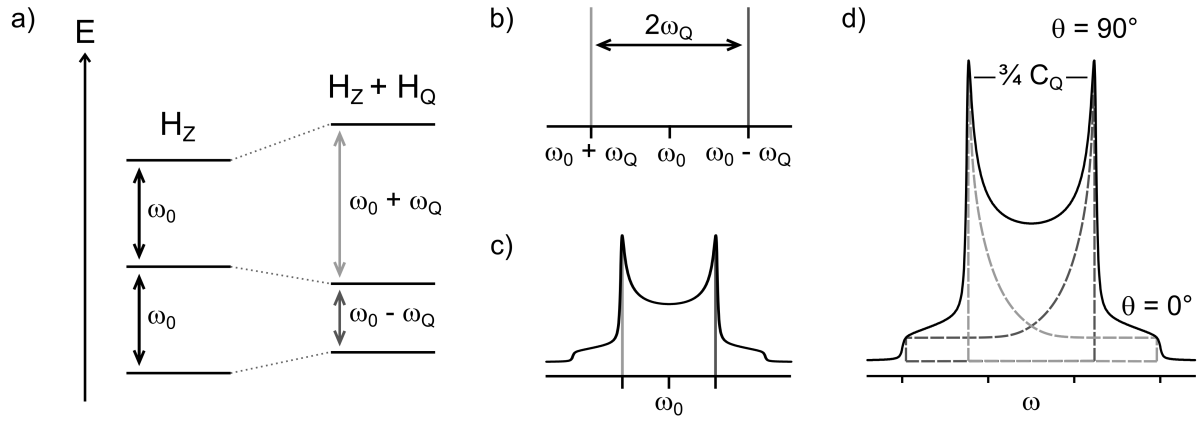

Figure 2.4: Schematic representation of the processes taking place when a quadrupolar nucleus is placed within a magnetic field. a) Modification of the initial Larmor frequency ω_0 due to the perturbation of the Zeeman interaction Hamiltonian $\mathcal{H}_Z$ by the contribution of the first-order quadrupolar interaction $\mathcal{H}_Q$. b) Signals arising from the two modified frequencies $\omega_0 \pm \omega_Q$ for a single crystal. c) Characteristic Pake pattern line shape obtained for powders. d) Magnified Pake pattern including the contributions of both transitions. Their intensities depend on the angle θ of the crystallite to B_0. The measurements of the distance between the singularities of the Pake pattern (for small η values) or between the two signals observed for a single crystal aligned along Q_{ZZ} allows for the calculation of the quadrupolar coupling constant C_Q.

Since the spectral shape obtained in ^{2}H NMR depends strongly on the relationship of the nucleus to the EFG, it is highly sensitive to dynamic processes and can therefore be utilized to probe motions on a molecular level. Thus, ^{2}H NMR spectroscopy can aid in elucidating binding situations, sorption kinetics and rotational as well as translational movement while being specific to the probed compound.[96]

2.3.2 The Solid Echo Pulse Sequence

NMR spectroscopy relies on the application of RF pulses to the sample in order to nutate the magnetization away from its orientation along B_0. However, after the pulse is applied, a certain time has to elapse before the measurement can commence in order not to saturate the receiver with any residues of the applied RF field. This so-called dead time t_d can lead to the signal having partially decayed before the receiver is ready to read out the magnetization.[97]

In order to solve this issue for fast-relaxing nuclei like ^{2}H, the solid echo pulse sequence was proposed by Powles and Mansfield in 1962.[98] As shown in Figure 2.5, it features two 90°-pulses separated by the echo delay time τ. The two pulses themselves are phase-shifted by 90°. This leads to the formation of an echo after the second increment of τ. If τ is chosen appropriately ($T_2 > \tau > t_\mathrm{d}$), the signal maximum is therefore shifted out of the dead time, making the observation of the full signal decay feasible.

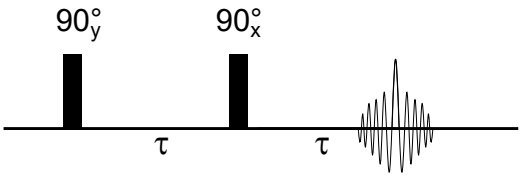

Figure 2.5: Solid echo pulse sequence as introduced by Powles and Mansfield.[98] The two applied 90°-pulses are phase-shifted by 90° and spaced apart by τ. An echo formation is observed 2τ after the first pulse. The pulse phases were chosen exemplary.

2.4 Magic Angle Spinning

In liquid-phase NMR, many anisotropic interactions of the nuclei with each other as well as the interactions of the nuclei with the electric field gradient are averaged due to molecular tumbling. Therefore, they are not observable in that case, leading to narrow line widths and well-resolved spectra. As molecular tumbling is restricted or even impossible in the solid state, interactions like the dipolar coupling, the chemical shift anisotropy or the quadrupolar coupling are of relevance when measuring NMR spectra of those samples.[99] These effects cause unwanted broadening of the observed signals, rendering the obtained spectra difficult to interpret and analyze. Equations 2.8 to 2.10 display the Hamiltonians $\mathcal{H}_\mathrm{CS}$, $\mathcal{H}_\mathrm{D}$ and $\mathcal{H}_\mathrm{Q}$ and therefore the orientation dependence for the chemical shift, the heteronuclear dipolar interaction as well as the first-order quadrupolar interaction, respectively.[100]

$$\mathcal{H}_\mathrm{CS} = \left(\omega_0\sigma_\mathrm{iso} + \frac{\omega_0\delta_\sigma}{2}\left[\left(3\cos^2\theta - 1\right) - \eta_\sigma \sin^2\theta\cos 2\phi\right]\right)\cdot \hat{\mathrm{I}}_\mathrm{Z} \tag{2.8}$$

$$\mathcal{H}_{\mathrm{D}} = \frac{\mu_0 \gamma_{\mathrm{I}} \gamma_{\mathrm{S}} \hbar}{4\pi r_{\mathrm{IS}}^3} \cdot \frac{(3\cos^2\theta - 1)}{2} \cdot 2\hat{\mathrm{I}}_{\mathrm{IZ}}\hat{\mathrm{I}}_{\mathrm{SZ}} \tag{2.9}$$

$$\mathcal{H}_{\mathrm{Q}} = \frac{eQV_{\mathrm{ZZ}}}{4I(2I-1)\hbar} \left[(3\cos^2\theta - 1) - \eta \sin^2\theta \cos 2\phi\right] \cdot \left(3\hat{\mathrm{I}}_{\mathrm{Z}}^2 - \hat{\mathrm{I}}^2\right) \tag{2.10}$$

Here, σ_{iso} is the isotropic chemical shift, δ_σ is the chemical shielding anisotropy, η is the shielding asymmetry, γ is the gyromagnetic ratio of the corresponding nucleus and θ as well as ϕ describe the orientation in respect to B_0.

To counter the unwanted line broadening caused by anisotropic interactions, magic angle spinning (MAS) is frequently used. First described in 1958,[101] MAS consists of a very fast sample rotation (speeds of tens of kHz are common) around the magic angle, $\theta_{\mathrm{M}} = 54.74°$. MAS leads to the vanishing of the anisotropic portion of the chemical shift, as well as of the heteronuclear dipolar and first-order quadrupolar interaction, thanks to their angular dependence as described in eq. 2.11 in cases where the spinning frequency exceeds the strength of the interaction.

$$3\cos^2\theta_{\mathrm{M}} - 1 = 0 \tag{2.11}$$

In cases where the spinning speed does not exceed the strength of the interaction, spinning sidebands are observed in addition to the signal of the isotropic chemical shift. These sidebands differ in frequency by the spinning frequency and trace the envelop usually observed in the static case. Figure 2.6 demonstrates this for the example of frozen *n*-octanol-d_{17} measured at three different spinning frequencies.

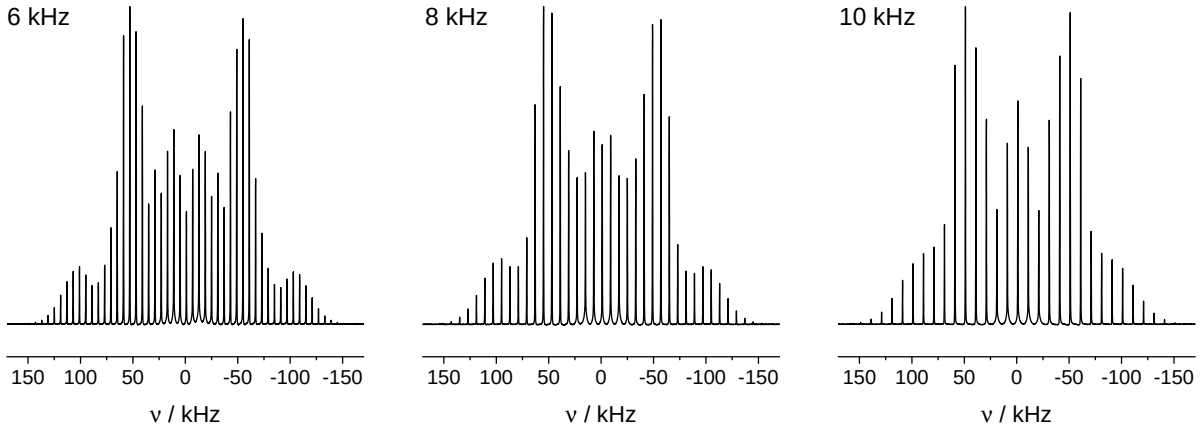

Figure 2.6: Three ^{2}H MAS ssNMR spectra of the sample *n*-octanol-d_{17} at spinning speeds of 6 kHz, 8 kHz and 10 kHz.

As the quadrupolar interaction is too strong to be averaged out at these relatively low spinning frequencies, the shape of the characteristic Pake pattern is still discernible. While the spinning frequency is varied, the sidebands move, while the signal associated with the isotropic chemical shift remains at the same frequency, facilitating its assignment.

Figure 2.7 illustrates the technique of MAS NMR spectroscopy as it is usually applied in the NMR spectrometer. The sample is packed into a rotor and inserted into the probe head of the utilized NMR spectrometer. There, the sample is held and spun by variable gas streams consisting of either compressed air, nitrogen gas or helium gas, depending on which temperatures need to be reached.

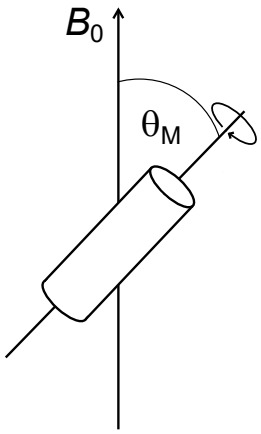

Figure 2.7: Schematic representation of MAS. The rotor containing the sample is spun around its own axis rapidly while tilted at θ_M = 54.74° in relation to B_0.

2.5 Cross Polarization

The observation of protons in a typical NMR experiment of an organic compound is quite simple, as they offer a high natural abundance, a high gyromagnetic ratio $\gamma_{^1\mathrm{H}}$ and short relaxation times, enabling the quick acquisition of numerous scans. However, more advanced NMR experiments regularly require the observation of heteronuclei (e.g. nitrogen, carbon, silicon, phosphorus). These heteronuclei usually have smaller gyromagnetic ratios, are oftentimes less abundant and frequently show long relaxation times, making their observation challenging. To tackle these problems, cross polarization (CP) is usually employed in the solid state.[102]

CP enables the polarization transfer from easily-observed nuclei *I* (usually protons or fluorine) to harder-to-observe heteronuclei *S* by exploiting the magnetic dipolar coupling D_{IS} of the two spins. As opposed to liquid phase NMR, where heteronuclei can benefit from indirect enhancement through the Nuclear Overhauser effect[103] (NOE) whenever the corresponding protons are saturated for the purpose of decoupling, the two spins need to be brought into contact with each other for CP to proceed. By bringing two differently polarized spin systems into contact, a common spin temperature can be established after some time.

In order for two spins I and S to come into contact with each other and therefore to exchange polarization, the Hartmann-Hahn condition[104] needs to be fulfilled (eq. 2.12). It describes a state in which the energy difference between the two levels giving rise to the NMR signal are equal for both nuclei in their respective rotating frame, leading to energy-maintaining flip-flop processes and therefore to polarization transfer between the two nuclei.

$$\gamma_{\mathrm{I}} \cdot B_{\mathrm{I}} = \gamma_{\mathrm{S}} \cdot B_{\mathrm{S}} \tag{2.12}$$

For a non-rotating sample, the spinning frequency is $\omega_{\mathrm{R}} = 0$, meaning that no modifications are necessary. For the CP MAS case, the Hartmann-Hahn condition is modified with the spinning frequency ω_{R} as depicted in equation 2.13. This is necessary since the dipolar interaction is modulated by MAS. The best enhancement of the S-spin is observed for the cases of $n = \pm 1, 2$.

$$\gamma_{\mathrm{I}} \cdot B_{\mathrm{I}} = \gamma_{\mathrm{S}} \cdot B_{\mathrm{S}} \pm n\omega_{\mathrm{R}} \tag{2.13}$$

In order to achieve a matching of energy levels according to equations 2.12 or 2.13, two magnetic fields in the shape of two spin-lock pulses B_1 and B_2 are applied to the respective nuclei in the so-called contact time. Figure 2.8 displays a typical pulse sequence for a CP MAS solid-state NMR experiment as well as the energy levels of interest if Hartmann-Hahn matching is applied for the example of ^{1}H $\rightarrow$ ^{13}C CP experiments.

Since MAS leads to an averaging of the dipolar coupling, fast spinning of a sample can hinder the efficient polarization transfer from the abundant to the dilute nucleus *via* CP.[105] To counter this, a ramped pulse

is usually applied (either nucleus is possible), therefore allowing the B_1-field to cover more frequencies and facilitating the fulfillment of the Hartmann-Hahn condition for all observed nuclei.[106]

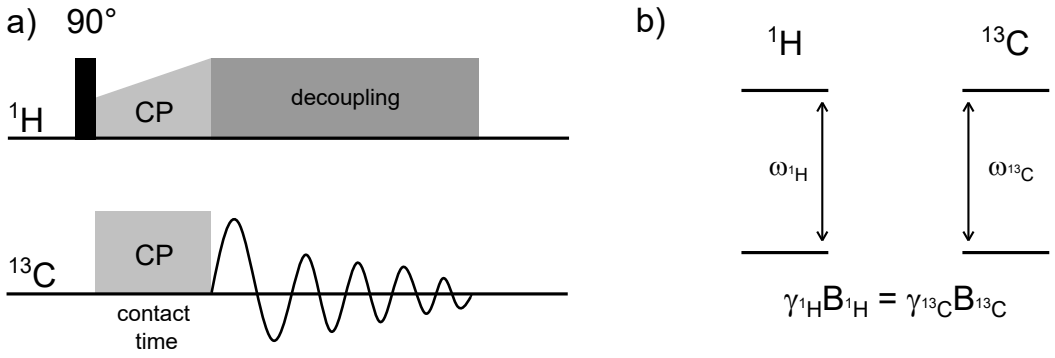

Figure 2.8: a) Pulse sequence utilized in ^{1}H $\rightarrow$ ^{13}C CP MAS experiments. b) Energy levels of the involved nuclei ^{1}H and ^{13}C when the Hartmann-Hahn condition is fulfilled, in the rotating frame.

For ^{1}H $\rightarrow$ ^{13}C CP experiments, one of the typical applications of CP in solid state NMR, a maximum theoretical enhancement factor of 4 can be expected on the carbon nuclei, resulting from the ratio of the two gyromagnetic ratios $\gamma_{^1\mathrm{H}}$ and $\gamma_{^{13}\mathrm{C}}$.[105]

2.6 Solid-State Heteronuclear Correlation Spectroscopy

Solid-state Heteronuclear Correlation (HETCOR) spectroscopy allows for the two-dimensional detection of spatial correlations between nuclei (usually an abundant nucleus like ^{1}H and a dilute heteronucleus like ^{13}C or ^{29}Si) through CP. As it provides information on the orientation of molecules to each other and on the connection of nuclei, it is commonly used to probe the interactions of small molecules with their host material[48,107,108] as well as to verify surface modifications of e.g. silica materials[109,110] or cellulose.[111]

The pulse sequence was originally devised in 1977 and demonstrated on liquid samples.[112] For the application to solid samples, a method to decouple the strong proton homonuclear dipolar coupling (up to multiple hundreds of kHz) needed to be introduced in order for the proton dimension to reach sufficient resolution.[113] In 1996, frequency-switched Lee-Goldburg[114] (FSLG) homonuclear decoupling was proposed for solid-state HETCOR spectroscopy.[115] The corresponding pulse sequence is illustrated in Figure 2.9 for the example of ^{1}H and ^{13}C. Other combinations of nuclei like ^{1}H and ^{29}Si[48] or ^{19}F and ^{13}C[116] are possible as well.

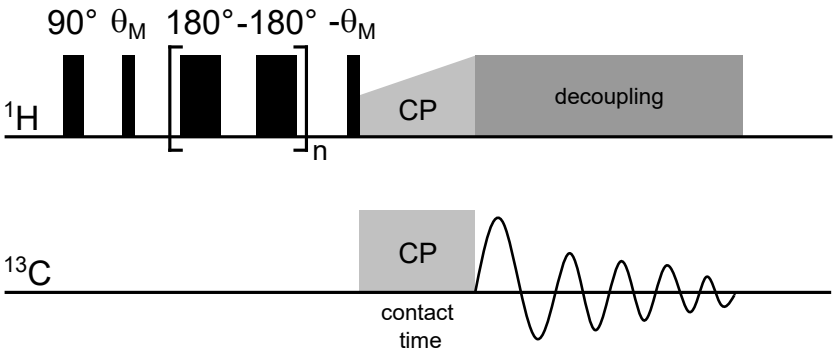

Figure 2.9: Pulse sequence utilized for solid-state FSLG HETCOR NMR measurements with detection on the heteronucleus for the example of ^{1}H and ^{13}C. The spacing of the pulses on the proton channel does not reflect the actual pulse spacing. All pulses are in direct succession.

The solid-state FSLG HETCOR pulse sequence consists of three parts. First, the FSLG sequence is applied on the proton channel during the evolution time. Subsequently, the CP takes place during the mixing time, before the X-channel magnetization is read out under heteronuclear decoupling, further enhancing the signal quality. The FSLG sequence itself consists of the application of an off-resonance RF pulse according to the LG condition[114] in the rotating frame (LG irradiation) which induces an effective field inclined at θ_{M} to B_0. This causes the proton spins to precess around this new axis, leading to an effective decoupling of the homonuclear dipolar coupling. Additionally, the LG irradiation is phase- and frequency switched, further increasing the efficiency of the decoupling scheme. To bring the magnetization back into the xy-plane, a second θ_{M} pulse is applied afterwards, enabling CP according to the Hartmann-Hahn condition as described by eq. 2.12 or eq. 2.13.

2.7 Hyperpolarization Methods

2.7.1 Sensitivity Issues

While NMR spectroscopy is a method which is highly applicable to a plethora of scientific problems, it suffers from an intrinsic lack of sensitivity.[117] This results from the Zeeman interaction being relatively weak for most nuclei under typical NMR conditions, leading to an almost equal population of the spin states α and β along with a small population difference P.[118] For $I = \frac{1}{2}$ nuclei, P can be expressed as a function of γ_{N}, B_0 and T, as shown in equation 2.14.

$$P = \frac{N_\alpha - N_\beta}{N_\alpha + N_\beta} = \tanh\left(\frac{\hbar\gamma_{\mathrm{N}}B_0}{2k_{\mathrm{B}}T}\right) \approx \frac{\hbar\gamma_{\mathrm{N}}B_0}{2k_{\mathrm{B}}T} \tag{2.14}$$

Under typical NMR conditions, P amounts to approximately 100 ppm.[118] According to equation 2.14, P can be enhanced by increasing B_0 or lowering T. However, such modifications to the experimental setup are often cumbersome, costly and only lead to a relatively moderate improvement of P. Additional methods of increasing the signal-to-noise ratio include polarization transfer schemes like CP or Insensitive Nuclei Enhancement by Polarization Transfer (INEPT)[119] as well as the application of specialized equipment like cryoprobes[120] or microcoils.[121] However, the observed sensitivity enhancement is limited, as no additional non-equilibrium nuclear polarization can be created. Therefore, hyperpolarization methods (methods to create non-equilibrium nuclear polarization) are of great interest for the NMR community as they allow for an enhancement of NMR signals of multiple orders of magnitudes.

The following chapter will give an overview of commonly used hyperpolarization methods, e.g. Parahydrogen Induced Polarization (PHIP), Signal Amplification by Reversible Exchange (SABRE), Spin-Exchange Optical Pumping (SEOP) and Chemically Induced DNP (CIDNP). As DNP enhanced NMR is the method of interest in this work, a separate chapter is dedicated to the technique, its theoretical description and different applications.

2.7.2 Parahydrogen Induced Polarization

PHIP was first observed by Bryndza after storing hydrogen-containing samples in LN_2 while completing his PhD thesis.[122] However, as the phenomenon was unknown at the time, the observed signal enhancement was attributed to CIDNP.[123] Subsequently, PHIP was predicted by Bowers and Weitekamp in 1986[124] and demonstrated by Eisenschmid as well as Bowers in 1987.[125,126] PHIP relies on a polarization transfer to a substrate *via* a reaction with parahydrogen (p-H_2). At room temperature, hydrogen gas consists of 75 % orthohydrogen (o-H_2) and 25 % p-H_2. In order to convert the more abundant spin isotope o-H_2 to p-H_2, cooling to low temperatures and the utilization of a catalyst is required to speed up the symmetry-forbidden transition.[127] This leads to an enrichment of p-H_2 of over 99 % at 20 K.[128] After the conversion and in the absence of a catalyst, the p-H_2 can be stored for multiple weeks.[129] Conveniently, $I = 0$ for molecular p-H_2, rendering it invisible in the NMR spectrum before it is actually applied to hyperpolarize a substrate.

After the enrichment of p-H_2, it is reacted with an unsaturated bond, chemically modifying the corresponding substrate. Assuming that the substrate is not symmetric around the bond of relevance, the pairwise hydrogenation breaks up the symmetry of the p-H_2 molecule, leading to two non-equivalent protons. The non-thermal spin polarization of the p-H_2 is conserved, producing hyperpolarized signals of the hydrogenated product. This enhancement can bridge several orders of magnitude, regularly producing enhancement factors larger than 1000.[130] Additionally, the polarization of p-H_2 can be transferred to neighboring heteronuclei *via* transfer schemes like INEPT[131] or field-cycling.[132]

In the solid state, PHIP is usually not employed. Experimental as well as theoretical works have shown that ssNMR of p-H_2 adsorbed on a solid surface is possible[133–135] but the technique has yet to find a broad field of application.

2.7.3 Signal Amplification by Reversible Exchange

While PHIP works exceptionally well to enhance NMR signals, it is limited to unsaturated substrates and, due to the chemical reaction taking place, irreversible, meaning that a new sample has to be prepared for each measurement. To tackle these limitations, SABRE was introduced in 2009 by Duckett and coworkers.[136] Like PHIP, SABRE makes use of the non-equilibrium polarization of p-H_2 but does not require a direct hydrogenation of the substrate, therefore significantly expanding the set of suitable analyte molecules. All molecules which readily and reversibly coordinate to a catalyst are potentially suitable for hyperpolarization *via* SABRE. However, this still excludes a multitude of possible substrates.

SABRE employs homogeneous transition metal (usually iridium) catalysts which coordinate the p-H_2 as well as the substrate. This forms a network of spin-spin coupled (J-coupled) nuclei, allowing for the polarization transfer from the p-H_2 to the substrate. In order for the transfer to operate efficiently, the J-coupling interaction of the active complex needs to be in the order of the chemical shift difference of the p-H_2 and the target nucleus of the substrate. Hence, SABRE transfers are usually carried out in low fields to make sure that the spin-spin coupling is the dominant interaction[128,137] or special techniques like LIGHT-SABRE (Low-Irradiation Generation of High Tesla-SABRE) are employed.[138] Like PHIP, SABRE is not usually applied in the solid state. However, immobilized SABRE catalysts have been demonstrated in the literature.[139]

2.7.4 Spin-Exchange Optical Pumping

In order to hyperpolarize noble gas atoms like ^{129}Xe or ^{3}He, SEOP is applied. In SEOP, a vapor of alkali metal atoms (e.g. rubidium) is produced. Circularly polarized light is irradiated on these atoms, polarizing their valence electrons.[140] Once the alkali metal atoms collide with noble gas atoms in the chamber of the polarizer, the alkali metal atoms transfer some of their electron spin polarization to the noble gases, thereby hyperpolarizing their nuclei.[141] This hyperpolarization can then be read out with an NMR or MRI magnet.

Since the method conveniently hyperpolarizes inert noble gases, it is applied to facilitate the visualization of lung tissue in MRI without risking the health of the patient. Additionally, ^{129}Xe is capable of diffusing through the cell membranes of the respiratory system, dissolving in aqueous tissue and blood, allowing for the study of the neighboring structures.[142] As its chemical shift is highly sensitive to its surroundings, hyperpolarized ^{129}Xe can also be used as a probe to characterize porous solids like zeolites,[143] mesoporous silica[144], metal-organic frameworks[145] or porous carbon materials.[146]

2.7.5 Chemically Induced Dynamic Nuclear Polarization

CIDNP was first reported by Bargon in 1967[147] when enhanced emissive spectral signals were recorded for rapid radical reactions observed by NMR spectroscopy. While the name implies a polarization transfer similar to regular DNP experiments, the effect can be more suitably explained by the radical pair mechanism.[148,149]

Usually, in CIDNP experiments, energy is introduced into the sample containing a photosensitive dye employing light (photo-CIDNP). This leads to the excitation of the dye molecules into a singlet excited state, which may change into the more long-lived triplet excited state through intersystem crossing. Subsequently, the dye is brought into contact with an electron donor molecule, forming a triplet correlated radical pair. This radical pair can now either recombine to form the recombination products or separate, diffuse through the sample as free radicals and eventually form the escape products. Nuclei which are hyperfine coupled to the radicals are influenced by the triplet-singlet conversion, in turn leading to nuclear polarization and therefore enhanced NMR signals.[150] Thermal excitation without a dye is possible as well but has been become less common since the inception of photo-CIDNP.[147,151]

In solutions, CIDNP has been applied to probe the surface structure of proteins,[152] to examine protein-ligand interactions[153] or to elucidate reaction mechanisms of chemical reactions which lead to radical formation.[154] In solids, CIDNP has been utilized to probe active centers in proteins or photosynthetic reaction centers.[155–158]

3 Dynamic Nuclear Polarization

In 1953, DNP was first observed by Carver and Slichter[159] after it had been predicted for metals with conducting electrons by Overhauser just a few months before.[160] The team discovered that the NMR signal of lithium metal could be enhanced nearly 100-fold by saturating the $\alpha \rightarrow \beta$ transition of the electrons of the investigated ^{7}Li. Shortly after, an almost 20-fold enhancement of proton signals was reported utilizing a free radical as the source of hyperpolarization, proving that the effect named after Overhauser had a wider field of application than first expected.[161]

Despite the strong enhancements that could be observed, DNP enhanced NMR spectroscopy remained a niche topic since the availability of the necessary high-frequency gyro- or klystrons necessary to produce high-energy microwaves was scarce, limiting DNP enhanced NMR spectroscopy to low magnetic fields. While there were some works published in the 1980s,[162] it took until the 1990s for the first high-field setups to be developed by the group of Robert Griffin. These setups also allowed for the use of MAS, further enhancing the resulting signal-to-noise ratio and reaching enhancement factors of up to 40 for ^{13}C.[163,164] After the release of the first commercial DNP instrument in 2009, DNP enhanced NMR spectroscopy became accessible for a wide range of users, leading to a significant increase of publications concerning the topic and a plethora of possible applications.[165]

The following chapter aims to give an overview on the technique of DNP enhanced NMR spectroscopy. First, the instrumentation and the theoretical background of DNP enhanced NMR spectroscopy, including the underlying transfer mechanisms of the polarization from the electron to the nucleus, are explained. Subsequently, the specialized DNP technique applied in this work is introduced.

3.1 Instrumentation

DNP enhanced NMR spectroscopy requires specialized instrumentation. Figure 3.1 shows a scheme representing the instruments utilized in this work. The spectrometer frequency is 400 MHz (9.4 T), requiring a microwave (µw) frequency of 263 GHz to excite the electron paramagnetic resonance (EPR) transitions of the electrons in the sample. The low-temperature MAS unit has two purposes. It produces the nitrogen gas necessary to spin and temper the sample within the probe by evaporating liquid nitrogen (LN_2), enabling the execution of measurements at approximately 100 K. It also contains the MAS control

panel, allowing for the adjustment of the spinning frequency. The µw transmission line connects the gyrotron with the probe, guiding the µw into the sample.

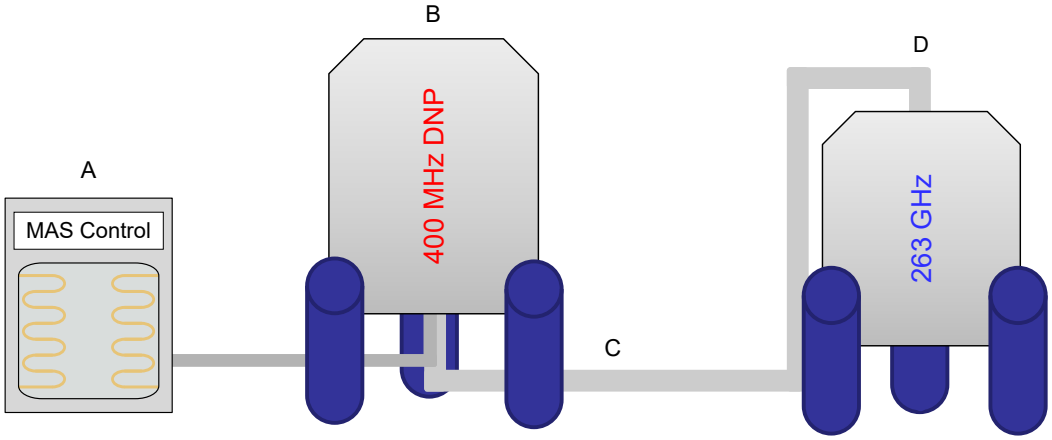

Figure 3.1: Schematic representation of the instrumentation used in this work. A: Low-temperature MAS unit. The unit contains the MAS controls as well as a cooling tank containing LN_2. This tank features three chambers with heat exchangers, evaporating the LN_2 and supplying cold gas for the bearing, driving and variable-temperature gas streams used to spin and temper the sample. B: Solid state NMR spectrometer system equipped with a 3.2 mm low temperature H/X/Y triple resonance probe. The magnet is sweepable, allowing for the matching of DNP matching conditions. C: µw transmission line, connecting the gyrotron (D) with the probe. D: µw source in the form of a gyrotron.

3.2 Theoretical Considerations of DNP Enhanced NMR spectroscopy

DNP uses the fact that, thanks to a much larger gyromagnetic ratio, electron polarization is about three orders of magnitude higher than that of nuclei. This results in a thermal spin polarization of about 6 % which is enhanced as T is lowered.[118] Once this polarization is transferred to the nucleus *via* DNP, the maximum possible enhancement ϵ_{max} calculated from the ratio of the µw on and µw off spectra is given by the ratio of the electron and nuclear gyromagnetic ratios, γ_{e} and γ_{N}, according to equation 3.1, assuming that both spectra were acquired at the same temperature.

$$\epsilon_{\mathrm{max}} = \left| \frac{\gamma_{\mathrm{e}}}{\gamma_{\mathrm{N}}} \right| \tag{3.1}$$

For ^{1}H, $\epsilon_{\mathrm{max}} \approx 660$ is obtained. For nuclei with smaller gyromagnetic ratios, an even larger theoretical maximum enhancement can be reached. In practice, the enhancement ϵ is obtained as the ratio of the

polarizations P_e and P_N of the electron and the nucleus. Figure 3.2a shows the spin polarization for an electron as well as for a proton as functions of the temperature. The resulting DNP enhancement factor is displayed in Figure 3.2b. The polarization is calculated according to equation 2.14, the theoretical maximum enhancement is obtained as the ratio of P_e and P_N. The decreasing theoretical maximum enhancement at lower temperatures is caused by the electron reaching its maximum polarization $P_\mathrm{e} = 1$ while the polarization of the nucleus increases further.

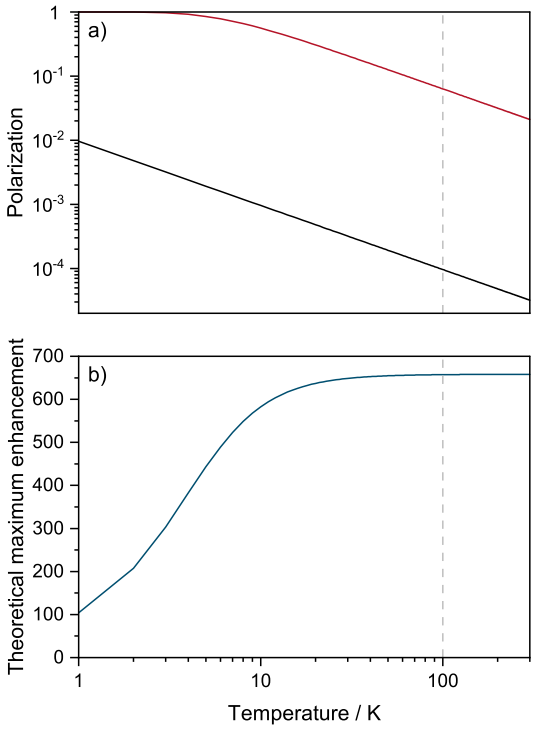

Figure 3.2: a) Theoretical polarization for electrons (—) as well as for protons (—) calculated according to eq. 2.14. b) ϵ resulting from the ratio of the respective spin polarizations of the proton and the electron. The gray dashed line marks the temperature at which DNP enhanced NMR spectroscopy is usually conducted, $\approx$ 100 K.

For DNP to proceed, the paramagnetic polarizing agent (PA, e.g. a stable organic radical[166–169] or a suitable, open-shell transition metal ion[170,171]) is irradiated with microwaves, inducing spin-transitions in the coupled electron-nucleus system and allowing for the transfer of the electron polarization to a hyperfine-coupled nucleus. The nature of the mechanism behind this transfer depends heavily on factors like the utilized PA or the temperature of the sample. The four mechanisms which might be active are the solid effect (SE), the cross effect (CE), the Overhauser effect (OE) and thermal mixing (TM). All of these effects rely on a hyperfine-coupled electron-nucleus system, yet they proceed in discernibly different manners and with varied efficiencies. However, the DNP effects are not mutually exclusive, meaning that polarization can be transferred through multiple DNP pathways simultaneously. The subsequent section aims to give an overview over the possible DNP mechanisms, including their theoretical description and typical fields of application. Please note that the following descriptions are valid for the static case. In the

case of MAS NMR spectroscopy, the description of the DNP effects becomes rather complicated as nuclear and electron energy levels as well as interactions are periodically modulated by the sample rotation. For information on DNP enhanced NMR spectroscopy and polarization transfer under MAS, reference is made to the literature.[172–175]

3.2.1 The Overhauser Effect

As the first DNP effect to be discovered,[159,160] the Overhauser effect has been well-understood for multiple decades. It relies on electron-nucleus cross relaxation (CR), which only occurs when the hyperfine interaction (HFI) between the two particles, e.g. the Fermi contact interaction and dipole-dipole coupling, is time-dependent in a stochastical manner due to the electrons or the nucleus being sufficiently mobile. In this process, the modulation of the HFI needs to be larger than the electron Larmor frequency, which is directly proportional to B_0, to enable the desired CR. This condition is usually fulfilled in metals with conducting electrons or in solutions containing free, unpaired electrons (e.g. alkali metals dissolved in ammonia).[159,176]

The reliance on these dynamics and the detrimental contribution of high field strengths explain why the OE was thought to be impossible to observe in frozen dielectrics under usual DNP conditions.[177] Hence, it took until 2012 for the first description of the effect in a typical DNP NMR sample containing an analyte and a molecular PA.[168] Since then, instrumentation and PAs have improved, making the routine application of OE DNP enhanced NMR spectroscopy feasible.[178–181] Especially water is an ideal probe molecule in ^{1}H OE DNP since it is capable of closely approaching a PA's nitroxide moiety to form short-lived contacts, leading to enhancements in the order of two magnitudes at high fields.[182,183]

The principle behind OE DNP enhanced NMR spectroscopy can be explained using a two-spin system in which $S = \frac{1}{2}$ and $I = \frac{1}{2}$ for the electron and the nuclear spin, respectively, as shown in Figure 3.3. First, the EPR single quantum (SQ) transitions (ω_S) are saturated by µw irradiation. Subsequently, cross relaxation between the electron and the nucleus takes place, transferring the non-equilibrium electron polarization to the nucleus. Depending on whether the zero quantum (ZQ) or double quantum (DQ) relaxation is active, negative (ϵ_neg) or positive (ϵ_pos) enhancement is observed, presuming that the auto-relaxation of the nucleus is slower than the polarization buildup via the CR.

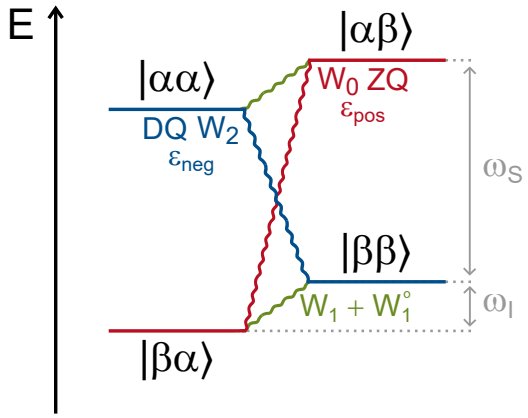

Figure 3.3: Four-level system of an e-n spin system with $S = \frac{1}{2}$ and $I = \frac{1}{2}$ in which the OE DNP mechanism is active. The energy levels are dominated by the electron and nuclear Larmor frequencies with ω_S and ω_I, respectively. µw irradiation of a suitable wavelength is used to induce SQ EPR transitions along ω_S. Due to stochastically time-dependent HFI, CR in the form of ZQ (red) and DQ transitions (blue) is induced between the electron and nuclear spin states, leading to enhancement of the NMR signal corresponding to the nucleus along ω_I. Nuclear SQ transitions giving rise to an NMR signal are displayed in green. The factors denoted with W_i refer to the corresponding transition probabilities in the Solomon equation (eq. 3.2).

The quantitative description of the obtained enhancement in OE DNP enhanced NMR spectroscopy can be derived from Solomon's theory describing relaxation processes in a two-spin system.[184] Equation 3.2 displays the corresponding steady state solution of the Solomon equation.

$$1 - \epsilon = \underbrace{\frac{2W_1 + W_2 + W_0}{2W_1 + W_2 + W_0 + W_1^\mathrm{o}}}_{f} \cdot \underbrace{\frac{W_2 - W_0}{2W_1 + W_2 + W_0}}_{\xi} \cdot s \cdot \epsilon_\mathrm{max} \tag{3.2}$$

The leakage factor f describes the efficiency of all HFI-induced polarization transfer pathways with respect to the entirety of the nuclear relaxation. The coupling factor ξ gives the ratio of the electron-nuclear CR and nuclear autorelaxation. Both utilize transition probabilities W_i of the ZQ ($i = 0$), SQ ($i = 1$) and DQ ($i = 2$) transitions. Additionally, the probability of nuclear relaxation unrelated to HFI, W_1^o, is used (compare Figure 3.3). The efficacy of the excitation of the EPR transition is given by the saturation factor s.[185]

3.2.2 The Solid Effect

Discovered in 1957,[186,187] the solid effect (SE) was the first DNP transfer mechanism reported for dielectric solids. Like the OE, it relies on a two-spin electron-nucleus-system, making its application viable when an intrinsic radical is used[188] or when a metal ion serves as PA.[189] As it does not rely on time-dependent

HFI, the dynamics of the analyte molecules are not of interest in order to obtain SE DNP. Instead, a local B-field transverse to B_0 is induced by the HFI, inducing partial state mixing of nuclear and electron states and allowing for the weak excitation of ZQ and DQ transitions in the spin system.

For the SE to proceed efficiently, the system consisting of the hyperfine coupled electron S and nucleus I must be excited with µw irradiation according to the matching condition (eq. 3.3), meaning that the µw frequency $\omega_{\mu w}$ must be the sum or the difference of the electron and nuclear Larmor frequencies, ω_S and ω_I. Otherwise, the observed state-mixing will not lead to the desired polarization transfer from the electron to the nucleus.

$$\omega_{\mu w} = \omega_S \pm \omega_I \tag{3.3}$$

In the laboratory frame, the states of the hyperfine coupled electron-nucleus-system behave according to Figure 3.3. However, when transforming the system into the rotating frame, the nuclear state mixing becomes more clear, as shown in Figure 3.4a and b.

To obtain efficient polarization transfer, PAs with narrow EPR transitions, like triarylmethyl-type radicals[190] or 1,3-bisphenylene-2-phenylallyl (BDPA) and its derivatives[191,192] as well as high-spin metal ions[189] are typically utilized in SE DNP.

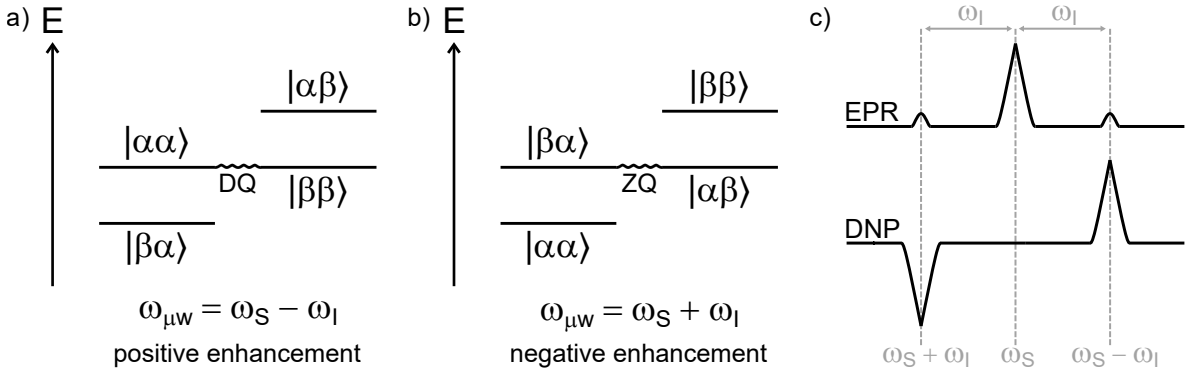

Figure 3.4: Four-level system of an e-n spin system with $S = \frac{1}{2}$ and $I = \frac{1}{2}$ in which the SE DNP mechanism is active, in the rotating frame. HFI induce state mixing, which, depending on which matching condition is fulfilled, can be utilized to transfer polarization *via* a) DQ or b) ZQ transitions. For a schematic illustration of the system in the laboratory frame, consider Figure 3.3. The relationship between the EPR spectrum of the utilized PA and the enhancement observed in the DNP enhanced NMR spectrum is shown in c).

Due to the necessity of state mixing for polarization transfer, which becomes increasingly difficult with increasing nuclear and electron Zeeman interactions, the SE is ineffective at high magnetic fields. The enhancement obtainable by SE DNP is described by equation 3.4, utilizing the maximum possible enhance-

ment factor $\epsilon_{\max}$, the magnetic field strength B_0, the µw field $B_{\mu w}$, the number of radicals N_e, the EPR transition line width of the PA δ and the T_1 of the involved nucleus.[193]

$$\epsilon_{SE} \propto \epsilon_{\max} \cdot \left(\frac{B_{\mu w}}{B_0}\right)^2 \cdot \frac{N_e}{\delta} \cdot T_{1_N} \tag{3.4}$$

3.2.3 The Cross Effect

The cross effect (CE) is the most effective DNP effect in dielectric solids described to date. First observed in 1963 in doped polyethylene samples under static conditions,[194,195] it took until 1976 for a reasonable description of the CE to be established.[196,197] Unlike the SE, the CE relies on allowed transitions in a hyperfine-coupled three-spin electron-electron-nucleus system. From the matching condition (equation 3.5), it becomes apparent that the EPR transition of the utilized PA needs to experience an inhomogeneous broadening of the order of ω_I, as the two coupled electrons need to differ in their Larmor frequency by the nuclear Larmor frequency.

$$\Delta\omega = \omega_{S_1} - \omega_{S_2} = \pm\,\omega_I \tag{3.5}$$

In order to achieve this, nitroxide biradicals which have been tailored for their use in CE DNP like TOTAPOL,[167] AMUPol,[166] bTbK[198] or TEKPOL[199] are most often used, ensuring a suitable electron-electron distance and therefore coupling. *Bis*-complexes of high-spin metal ions are also able to evoke the CE with less efficiency and are rarely used in practice.[200] For the CE to proceed, two different events must take place within the sample. First, the EPR transition of one of the electrons of the PA is irradiated and therefore saturated. Then, *via* electron-electron-nucleus flip-flop-flip processes, the polarization is transferred to the nucleus, thus hyperpolarizing it. Fulfilling the matching conditions leads to a degeneracy of the participating states connected by three-spin flips. This interaction is driven by the electron-electron coupling. Figure 3.5 illustrates this process.

Similar to the SE, the enhancement achievable through CE DNP can be estimated *via* equation 3.6 utilizing $\epsilon_{\max}$, $B_{\mu w}$, B_0, N_e, δ and T_{1_N}.[193] As the achievable enhancement through the CE is linearly dependent on the inverse of B_0 as compared to the dependence on the inverse square of B_0 of the SE, the CE is more robust when higher fields are utilized, making it the DNP effect of choice for most high-field DNP applications.

$$\epsilon_{CE} \propto \epsilon_{\max} \cdot \left(\frac{{B_{\mu w}}^2}{B_0}\right) \cdot \frac{{N_e}^2}{\delta^2} \cdot T_{1_N} \tag{3.6}$$

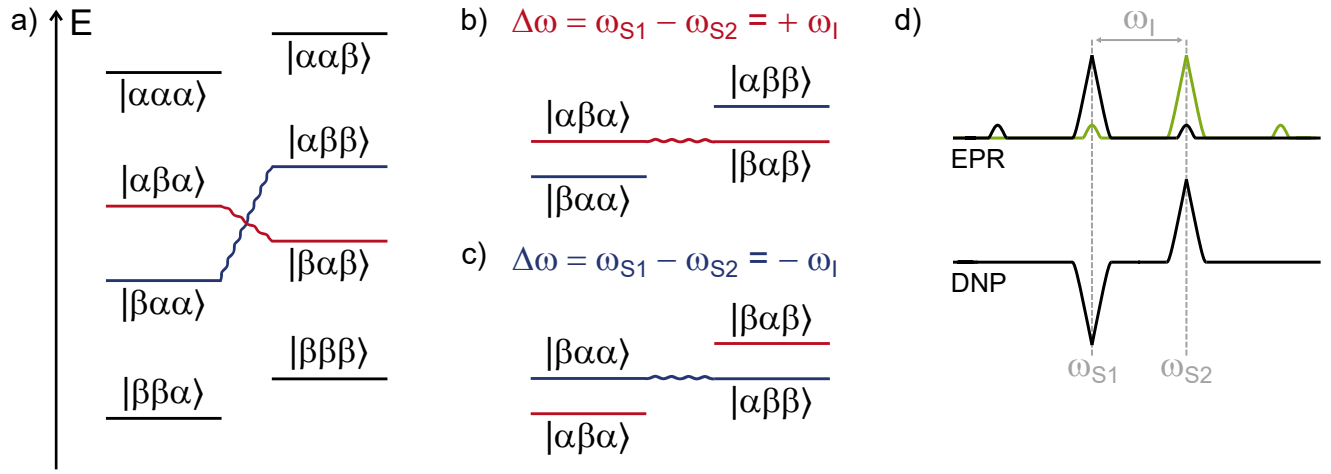

Figure 3.5: a) Eight-level system of an e-e-n spin system with S_1, $S_2 = \frac{1}{2}$ and $I = \frac{1}{2}$ in which the CE DNP mechanism is active. The two possible matching conditions are highlighted. b) and c) Level diagrams for the two CE matching conditions in the laboratory frame. d) Relationship between the EPR spectrum of the utilized PA with the two electrons and the enhancement observed in the DNP enhanced NMR spectrum. The color coding serves to enhance figure legibility.

3.2.4 Thermal Mixing

Thermal Mixing (TM) is an effect similar to the CE which is usually treated utilizing the concept of spin temperature. In this formalism, the electron-nuclear spin system is described as three interacting baths. These baths are the electron Zeeman system (EZS), the electron dipolar system (EDS) and the nuclear Zeeman system (NZS), each of which has its own characteristic spin temperature. Due to µw irradiation of the allowed EPR transitions in the system, a non-equilibrium polarization gradient is produced, cooling the EDS. Subsequently, the thermal contact between the EDS and the NZS cools the nuclear system through electron-electron-nucleus three-spin flips, leading to enhancement of the NMR signal.[201] For this process to proceed efficiently, the homogeneous line width of the EPR transition of the PA needs to be larger than ω_N. As TM is usually active at very low temperatures (< 10 K), it is not of relevance for the DNP NMR investigations presented in this work.[177]

3.3 Direct and Indirect DNP Enhanced NMR Spectroscopy

In 2016, a new effect was observed in ^{13}C direct polarization DNP enhanced NMR spectroscopy of surface active agents (surfactants) and proteins.[53,202] For these samples, it was found that the obtained DNP

enhanced NMR spectra consisted of two sets of resonances with opposite phases. This new effect, dubbed Specific Cross Relaxation Enhancement by Active Motions (SCREAM) DNP[55] or indirect DNP[53] by the groups that first identified it, relies on a NOE-type CR between the hyperpolarized proton reservoir and the observed low-γ heteronucleus (compare Figure 3.6). As this CR is mediated by time-dependent HFI, it is only active for sufficiently mobile molecular groups like rotating amine, ammonium[54] and methyl groups,[202] segments of glass forming molecules which do not crystallize completely under DNP conditions[53] or cyclohexane molecules undergoing ring flips.[203] This allows for their independent observation in crowded spectra as expected for biomolecules or the observation of molecular dynamics in the sample. The direction of the enhancement achieved through the indirect polarization transfer pathway depends on the sign of γ of the observed heteronucleus. Compared to the direct polarization pathway, this means that the indirect polarization pathway leads to opposite phase signals for ^{13}C (positive γ) and signals of the same phase for ^{15}N (negative γ).

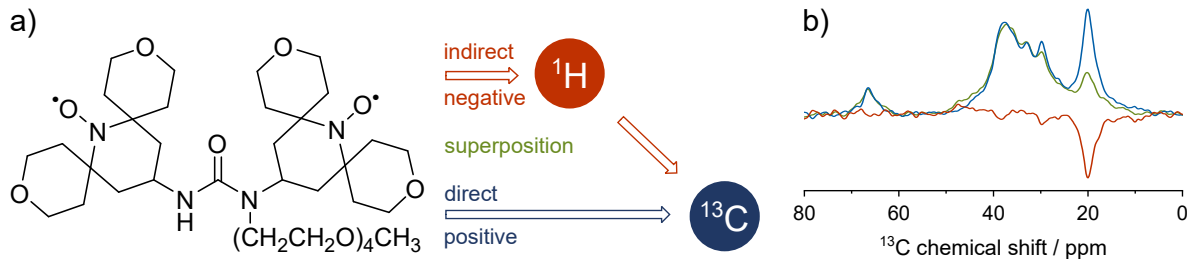

Figure 3.6: a) Overview of the concept of direct and indirect DNP with AMUPol as PA and ^{13}C as target nucleus in a sample of otherwise pure octanol. Two polarization transfer pathways are active, the direct pathway which proceeds from the PA directly to the observed nucleus and the indirect pathway, which proceeds *via* the proton reservoir. This pathway leads to an opposite phase signal enhancement for ^{13}C. b) Spectra as obtained for a sample showing direct and indirect DNP. The color coding is according to the pathways in a).

It was also found that the features corresponding to the NOE-type CR could be suppressed utilizing a pulse train consisting of rotor-synchronized 180°-pulses on the proton channel, confirming that the source of this kind of enhancement is the proton reservoir.[53,202] In addition, this allows for the sole observation of the direct polarization transfer pathway from the radical center of the PA to the observed heteronucleus as shown in Figure 3.7a and 3.7b. By subtracting the direct pathway spectrum from that acquired for the signal superposition, the spectrum corresponding to the indirect polarization transfer pathway is obtained.

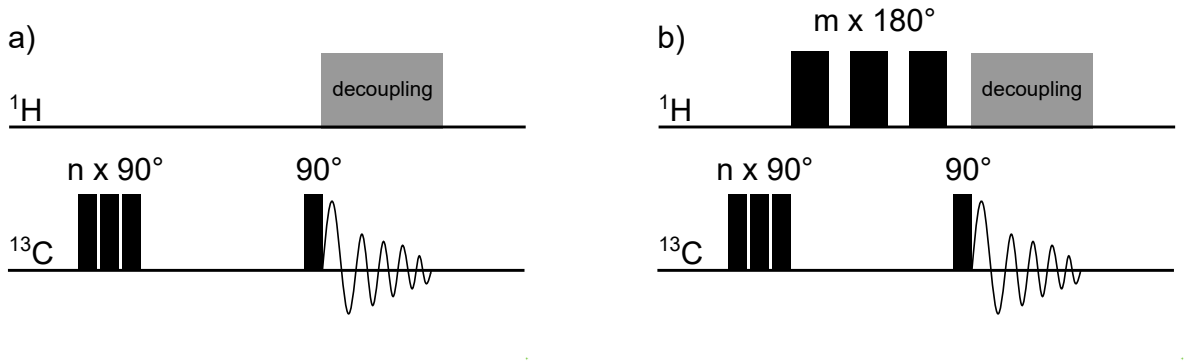

Figure 3.7: a) Pulse sequence utilized for direct polarization DNP enhanced measurements (saturation recovery pulse sequence) leading to a superposition of both polarization transfer pathways. b) Modified saturation recovery pulse sequence employing a train of 180°-pulses to suppress the ^{1}H contribution, leading to the observation of the direct pathway only. The spectrum corresponding to the indirect pathway is obtained as the difference of the spectra acquired in a) and b).

4 Results and Discussion

In the following chapter, the results obtained throughout the course of this work are presented. As the outcome has already been published in peer-reviewed journals, it is presented in this manner. This chapter is divided into three sections according to the systems investigated. Where present, the supporting information documents of the publications are provided as well. They can be found found directly following the corresponding publications.

The first chapter focuses on the application of ^{2}H ssNMR spectroscopy to probe the interaction of *n*-octanol-d_{17} with the PMS SBA-15. The second chapter describes the utilization of direct and indirect DNP enhanced ssNMR measurements carried out in *n*-octanol employing different radicals in order to elucidate polarization transfer patterns within the frozen liquid in dependence on the PAs' hydrophilicity. The third chapter gives an overview on the application of direct and indirect DNP enhanced ssNMR for the elucidation of the orientation and arrangement of PEGs and surfactants within the pores of PMS materials.

4.1 Determination of Octanol-d_{17} alignment in mesoporous SBA-15 through ^{2}H ssNMR Measurements

When molecules are brought in contact with a solid surface, e.g. through confinement in a mesoporous host material, the intra- and intermolecular interactions are in competition with those at the corresponding surface. Depending on the nature of the molecules as well as that of the surface, steric as well as electronic effects may govern these interactions.[39] In order to efficiently design immobilized catalyst systems in compliance with the green chemistry principles, it is necessary to understand and, eventually, fine-tune these interactions.

Deuterium acts as a highly sensitive probe on molecular dynamics. Hence, ^{2}H ssNMR serves as a key spectroscopic method to understand the way guest molecules interact with their mesoporous host materials.[39] However, if too many different deuterium nuclei are present in the sample, the analysis of the spectral shape becomes challenging. Therefore, the choice of analyte molecule is limited by molecular complexity.

In earlier works conducted in the group,[108] *n*-octanol-d_{17} has proven to be an ideal analyte molecule to illustrate the interactions of surfactants of the relatively simple type C_8E_0 with mesoporous silica materials. It offers a hydrophilic moiety, the hydroxy group, which can interact with any hydrophilic sites on the

silica surface. Additionally, *n*-octanol-d_{17} features a lipophilic aliphatic chain which allows for hydrophobic interactions. The amphiphilic nature of the molecule enables it to form micelles,[204] potentially enabling the formation of lipophilic micro- or nanoreactors in which reactions can take place.

In order to probe the interactions of the *n*-octanol-d_{17} with its mesoporous host, variable-temperature ^{2}H ssNMR measurements were conducted. Through these measurements, it could be shown that octanol displays a gradual melting behavior within the PMS. At the same time, supplementary differential scanning calorimetry (DSC) measurements disproved the formation of a glass, making the formation of a pore solid the most viable explanation for the observed behavior.[205] This implies the formation of a multitude of small crystallites with individual, size-dependent melting temperatures. To provide evidence for this hypothesis, the melting activation energies were investigated according to the literature,[206] marking the, to our knowledge, first application of the methodology to phase transitions. Indeed, a broad distribution of melting activation energies could be observed.

Reprinted with permission from S. C. Döller, M. Brodrecht, N. B. Haro Mares, H. Breitzke, T. Gutmann, M. Hoffmann and G. Buntkowsky, *J. Phys. Chem. C*, **2021**, *125*, 25155–25164. Copyright 2021 American Chemical Society.

THE JOURNAL OF PHYSICAL CHEMISTRY C
A JOURNAL OF THE AMERICAN CHEMICAL SOCIETY

pubs.acs.org/JPCC

Article

Deuterium NMR Studies of the Solid−Liquid Phase Transition of Octanol-d_{17} Confined in SBA-15

Sonja C. Döller, Martin Brodrecht, Nadia B. Haro Mares, Hergen Breitzke, Torsten Gutmann, Markus Hoffmann, and Gerd Buntkowsky*

Cite This: J. Phys. Chem. C 2021, 125, 25155−25164

Read Online

ACCESS | Metrics & More | Article Recommendations | Supporting Information

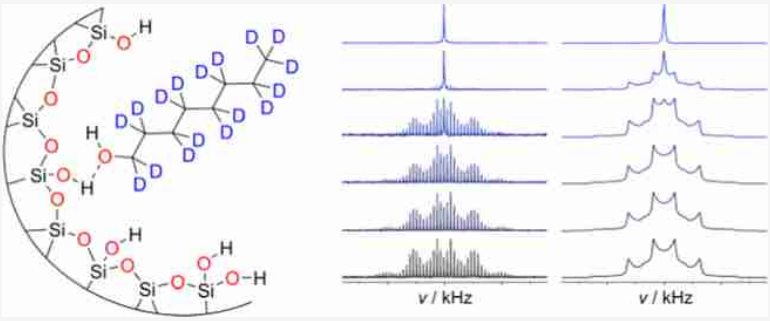

ABSTRACT: The interactions of molecules such as surfactants with solid interfaces are not sufficiently understood since their study is challenging with standard spectroscopic methods. In this work, octanol-d_{17} as a model system confined in the mesopores of SBA-15 is studied by variable temperature deuterium solid-state NMR, and the findings are compared to those of bulk octanol-d_{17}. The magic angle spinning (MAS) as well as the static, nonspinning case, are investigated, showing that the described observations are independent of the applied NMR method. The ^{2}H NMR spectra of both the bulk and the confined octanol-d_{17} show a large and a small quadrupolar Pake pattern below the melting point, suggesting a rigid conformation of the observed molecules with a 3-fold jump motion of the terminal CD_3-group. Apart from the melting of the solid, no other phase transition is observed for either sample. The confined octanol-d_{17} forms a pore solid, exhibiting a melting point 38 K lower than bulk octanol-d_{17}. The interactions of the molecule with the mesoporous SBA-15 bring about a distribution of activation energies for the melting process, resulting in a gradual melting process.

Downloaded via UNIV DARMSTADT on November 18, 2021 at 12:14:22 (UTC).
See https://pubs.acs.org/sharingguidelines for options on how to legitimately share published articles.

INTRODUCTION

Systems consisting of solid−liquid interfaces play a key role in many processes relevant to scientific and industrial applications. Heterogeneously catalyzed reactions,[1] liquid chromatography,[2] membrane-based separation processes,[3] drug delivery systems,[4] and waste-treatment systems,[5] among others, all rely on the interactions of a liquid phase and a solid adsorbent. Especially silica-based solid phases have been of interest due to their easy synthesis, their ordered structures, large surface areas, and the facile functionalization of their surfaces, allowing an adjustment of the material to the specific task.[6] These properties make silica-based systems ideal as model systems to investigate surface interactions and dynamics at a molecular level. Mesoporous systems, such as the class of Santa Barbara Amorphous[7] (SBA) and the family of M41S phases,[8] have been used as host materials to a plethora of guest molecules.[9−17]

One of the most interesting classes of guest molecules is surfactants. Due to their amphiphilic nature, they form aggregates like micelles and mono- as well as bilayer lamellae on their own[10,18−21] and in aqueous solution.[22−26] Typically, if the surfactants interact with a solid, different aggregates are formed compared to the behavior in their bulk solution without the influence of a surface.[27,28] However, despite the relevance and countless applications of these systems, the corresponding interactions are not fully understood and notoriously hard to probe at a molecular level, impeding the optimization of the utilized methods of analysis.[29] Recently, there have been advances in the fields of infrared,[30] Raman,[31] UV−vis,[32] and fluorescence emission spectroscopy,[33] as well as X-ray[34] and neutron-scattering[35]-based techniques to investigate adsorption on surfaces. Nonetheless, these techniques do not necessarily enable the observation of molecules confined in pores and their dynamics as closely as needed to gather a

Received: July 1, 2021
Revised: October 20, 2021
Published: November 4, 2021

ACS Publications

© 2021 American Chemical Society

deeper understanding of the interactions taking place. Consequently, ^{2}H solid-state NMR (ssNMR) has become an established method to study these systems. Due to the deuterium quadrupolar moment, the line shape of ^{2}H ssNMR spectra is highly sensitive to dynamic processes. Therefore, ^{2}H ssNMR spectra directly probe the movement of the compound of interest or dynamics of the structural moieties bearing deuterium at a molecular level, revealing information about rotational and translational movements, the binding situation, or sorption kinetics while being specific to the probed compound.[36]

In this work, octanol-d_{17} is used as a characteristic model compound for the class of linear, nonionic, and aliphatic surfactants. It is structurally similar to lipids found in biological membranes and therefore used as a membrane mimetic.[37,38] The water-octanol partition coefficient is employed as a measure to describe the partitioning of solutes between aqueous (hydrophilic) and organic (lipophilic) phases[13,15,16] and to predict the pharmacokinetic properties of drug molecules.[19−21] Octanol has been shown to interact with the surface of SBA-15 via its hydroxyl group,[10] but little is known about the dynamics of the aliphatic moiety of the molecule, making it an interesting compound for ^{2}H ssNMR studies in confinement at low temperatures and around its melting point. The spectra of bulk octanol-d_{17} are employed as reference to distinguish the effects of the confinement. The data obtained by differential scanning calorimetry (DSC) measurements is used to aid in understanding the observed phase transition. Modeling in accordance with Kissinger[39] and Rössler et al.[40] serves to elucidate the influence of the confinement on the temperature as well as the activation energy profile of the melting process. A detailed discussion on confinement effects on small molecules is beyond the scope of this paper and can be found in a recent review[41] and references therein.

The rest of the paper is organized as follows: first, the Experimental Methods section gives an overview of the synthesis and characterization of the utilized SBA-15 porous material, the sample preparation, the low-temperature DSC methods, as well as the applied ^{2}H NMR methods for obtaining static and magic angle spinning (MAS) spectra. Subsequently, the findings of this work are presented and discussed, starting with the DSC measurements and followed by the NMR investigation. In particular, the influence of confinement on the dynamics of octanol-d_{17} is discussed. A summary of the key findings and their applicability is provided in the Conclusions section.

EXPERIMENTAL METHODS

General. Information on the utilized chemicals can be found in Table S1 in the Supporting Information. All chemicals were used as received. The octanol-d_{17} as well as the mesoporous SBA-15 were stored in a glovebox under argon to prevent wetting of the sample with atmospheric water.

Synthesis of Mesoporous SBA-15. Mesoporous SBA-15 was synthesized via a literature-based protocol.[42,43] Accordingly, 21.3 g (0.017 equiv) of Pluronic123 was dissolved in 574 mL (165 equiv) of deionized water overnight. To the solution, 108.0 mL (6.0 equiv) of 37 wt % HCl was added to yield a HCl concentration of 1.9 mol L^{-1}. The solution was heated to 40 °C and allowed to equilibrate overnight. After that, 47.9 g (1 equiv) of tetraethyl orthosilicate was added slowly while stirring. Stirring was continued for 1 h, which resulted in a white precipitate. The suspension was stirred at 40 °C for 24 h and was then transferred into a Teflon (PTFE) bottle. The bottle was stored under static conditions at 90 °C for 48 h. The white precipitate was washed with deionized water twice and with ethanol once by centrifugation. The leftover template was removed by calcination at 650 °C yielding 11.70 g of SBA-15 mesoporous silica.

Porosity, Pore Volume, and Specific Surface Area of the Mesoporous SBA-15. In preparation of characterizing the synthesized SBA-15 porous material, the wet samples were transferred into a glass burette and predried at mild vacuum (∼10 mbar) overnight. After predrying, the samples were dried using a turbomolecular pump (10^{-6} mbar) overnight. During all drying steps, the samples were heated to 80 °C. The dried samples were directly transferred to a Thermo Fisher Scientific Surfer Brunauer−Emmett−Teller (BET) analyzer, which obtains the porosity, pore volume, and specific surface area of the material by controlled nitrogen adsorption at 77 K. The specific surface area was obtained by the Brunauer−Emmett−Teller[44] (BET) method, analyzing the curve in the p/p^0 range between 0.1 and 0.35. The pore volume was obtained by the Klyachko-Gurvich[45] method, using the p/p^0 value at 0.95. Blank measurements were performed using helium gas. Pore size distributions were obtained by applying the Barrett−Joyner−Halenda[46] (BJH) method, analyzing the adsorption−desorption isotherms in the p/p^0 range between 0.3 and 0.95. Pore sizes were obtained by nonlocal density functional theory (NLDFT) based on the model for the adsorption of nitrogen on silica surfaces with cylindrical pore geometries of Advanced Data Processing (ADP) software (V 6.2.4). The samples used for BET measurements were discarded and not used for ssNMR or DSC measurements. The obtained isotherms are visualized in Figure S1 in the Supporting Information.

Sample Preparation for ssNMR and DSC Measurements. In preparation for the impregnation with octanol-d_{17}, the SBA-15 material (d = 6.4 nm; S = 555 m^2 g^{-1}; V = 0.79 cm^3 g^{-1}) was placed under high vacuum at room temperature for 24 h. The dried silica was then transferred to the glovebox as quickly as possible to avoid the material absorbing water from the atmosphere. Octanol-d_{17} was added to the material to fill approximately 80% of the pore volume, and the material was left in the glovebox overnight to allow the octanol-d_{17} to be absorbed by the mesoporous silica. Of this material, approximately 2 and 6.5 mg were used for the DSC and NMR measurements, respectively. The DSC cubicles as well as the MAS rotors were filled in the glovebox. Examples of the spectra measured before the sample was allotted enough time for the octanol-d_{17} to be absorbed can be found in Figure S2 in the Supporting Information.

DSC Measurements. The DSC measurements were performed in a dynamic mode on the DSC 214 Polyma apparatus by Netzsch using evaporated liquid nitrogen as the cooling agent with an empty crucible serving as the reference. Heating rates of 5, 10, 20, and 40 K min^{-1} were used. The temperature range was set between 100 and 300 K for all compounds. For the analysis according to Kissinger,[39] the peak temperatures of the DSC signals are determined.

Variable-Temperature ^{2}H Solid-State NMR Spectroscopy. *General.* All measurements were carried out on a Bruker Avance III 400 DNP NMR spectrometer operating at 9.4 T (400.13 MHz for ^{1}H, 61.42 MHz for ^{2}H) equipped with a 3.2 mm low-temperature H/X/Y triple resonance probe, which was used in H/Y double mode to obtain a higher Q-factor for ^{2}H on the Y-channel. The temperature was controlled by a

https://doi.org/10.1021/acs.jpcc.1c05873
J. Phys. Chem. C 2021, 125, 25155−25164

Eurotherm 2416 temperature controller with a Pt100 sensor. Typically, 3.2 mm sapphire rotors with Teflon inserts and ZrO_2 drive caps were used. The spectra were measured in the range of 120−260 K. After each temperature step, the sample was allowed 15 min to thermally equilibrate.

Temperature Calibration. For MAS measurements, the temperature of the sample was calibrated according to Bielecki and Burum.[47] For the static measurements, the temperature within the probe head was determined by taking the reading of the auxiliary sensor installed directly in the stator of the probe head. At the observed melting point of octanol-d_{17}, both methods yield a temperature reading that falls within 1.5 K. The temperature uncertainty was therefore taken as 1.5 K.

^{2}H Magic Angle Spinning Measurements. MAS experiments were acquired as onepulse experiments with a pulse length of 2 μs, approximately corresponding to a 30° pulse. 64 scans were acquired with a recycle delay of 1 s. The spectra were analyzed with the program dmfit2015[48] using the integrated option Quad 1st model. To model the shape of the spectra, two Pake patterns and one Lorentzian signal were used throughout the analysis.

^{2}H Static Measurements. The static experiments were performed in resonance with a solid-echo pulse sequence using an echo delay of 40 μs and a pulse length of 2.6 μs, approximately corresponding to a 90°-pulse. 1024 scans were acquired using a recycle delay of 15 s. The obtained data was phase-corrected by maximizing the echo amplitude and symmetrized by deleting the imaginary part of the signal before the Fourier transformation. The simulated spectra in this work were calculated and fitted onto the experimental data with a Matlab script written in house. An example of an original, nonsymmetrized spectrum, including a corresponding fit, can be found in Figure S3 in the Supporting Information.

RESULTS AND DISCUSSION

DSC Measurements. Figure 1 shows the obtained DSC curves for octanol-d_{17} confined in mesoporous SBA-15 for the smallest and largest heating rate. Both curves show characteristic signals at ∼220 K and at ∼258 K, which are assigned to the confined octanol-d_{17} and nonconfined, superfluous bulk octanol-d_{17}, respectively. This result containing the bulk as well as the confined signal was not used for the following analysis but served as an exemplary comparison for the signal line shape only.

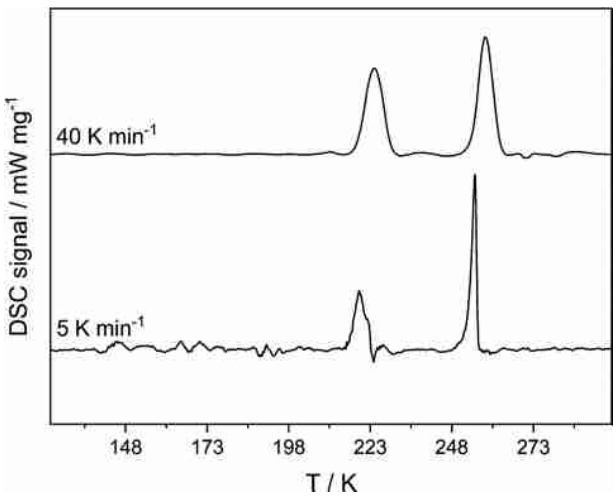

Figure 1. DSC curves for octanol-d_{17} in SBA-15 at 5 and 40 K min^{-1}. Heating rates are indicated in the figure. All curves are normalized to an equal height.

The DSC measurements yield the peak temperature of the sample for the different heating rates. According to Kissinger,[39] these peak temperatures can be used to calculate the activation energy E_A of the observed phase transition using the heating rate ν, the gas constant R, and the observed peak temperature T_p of the sample (eq 1). Since this model is not applicable to crystallization processes occurring under cooling conditions,[49] only the melting behavior of the samples under heating conditions is investigated.

$$\frac{\mathrm{d}\ln\left(\frac{\nu}{T_p^2}\right)}{\mathrm{d}\frac{1}{T_p}} = -\frac{E_A}{R} \tag{1}$$

Figure 2 displays the plots used to determine the activation energy of the phase transitions. The obtained data, including the determined activation energies, are shown in Table 1.

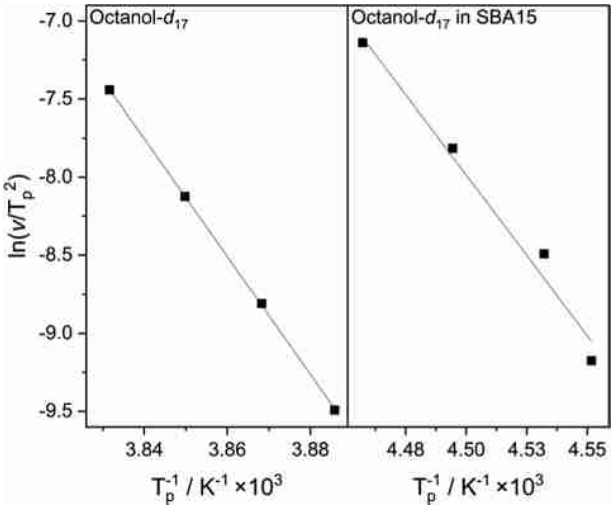

Figure 2. Kissinger plots for bulk octanol-d_{17} and for octanol-d_{17} in SBA-15.[39]

The octanol-d_{17} in SBA-15 melts at a temperature approximately 38 K lower than for bulk octanol-d_{17}, which can be interpreted as a result of confinement.[50] As expected from the observed lower melting point, the activation energy for the solid−liquid phase transition is smaller when octanol-d_{17} is confined. The relatively large error determined for the confined case stems from the observed broad scattering of peak temperatures. No other phase transition can be observed in the DSC measurements for either sample, which is in accordance with the literature.[51] The broader line shape of the melting DSC signature in Figure 1 for the confined octanol-d_{17} compared to the melting DSC signature of the crystalline bulk octanol-d_{17} indicates the presence of a variety of interactions of the guest molecule with the mesoporous SBA-15 surface, leading to different species with different melting points.[52] Considering the pore size of 6.5 nm, a full crystallization of the material in the pores is unlikely. Due to the interactions of the hydroxyl group of octanol-d_{17} with the pore walls, some order is probably established in the octanol-

https://doi.org/10.1021/acs.jpcc.1c05873
J. Phys. Chem. C 2021, 125, 25155−25164

Table 1. T_p and E_A of the Observed Phase Transition for Bulk Octanol-d_{17} and Octanol-d_{17} in SBA-15 for Different Heating Rates[a]

material	T_p in K at 5 K min^{-1}	10 K min^{-1}	20 K min^{-1}	40 K min^{-1}	E_A/kJ mol^{-1}
octanol-d_{17}	257.3	258.5	259.6	261.0	313.6 ± 2.10
octanol-d_{17} in SBA-15	219.7	220.6	222.3	224.4	172 ± 17

[a]Errors for E_A were determined based on the slope uncertainty.

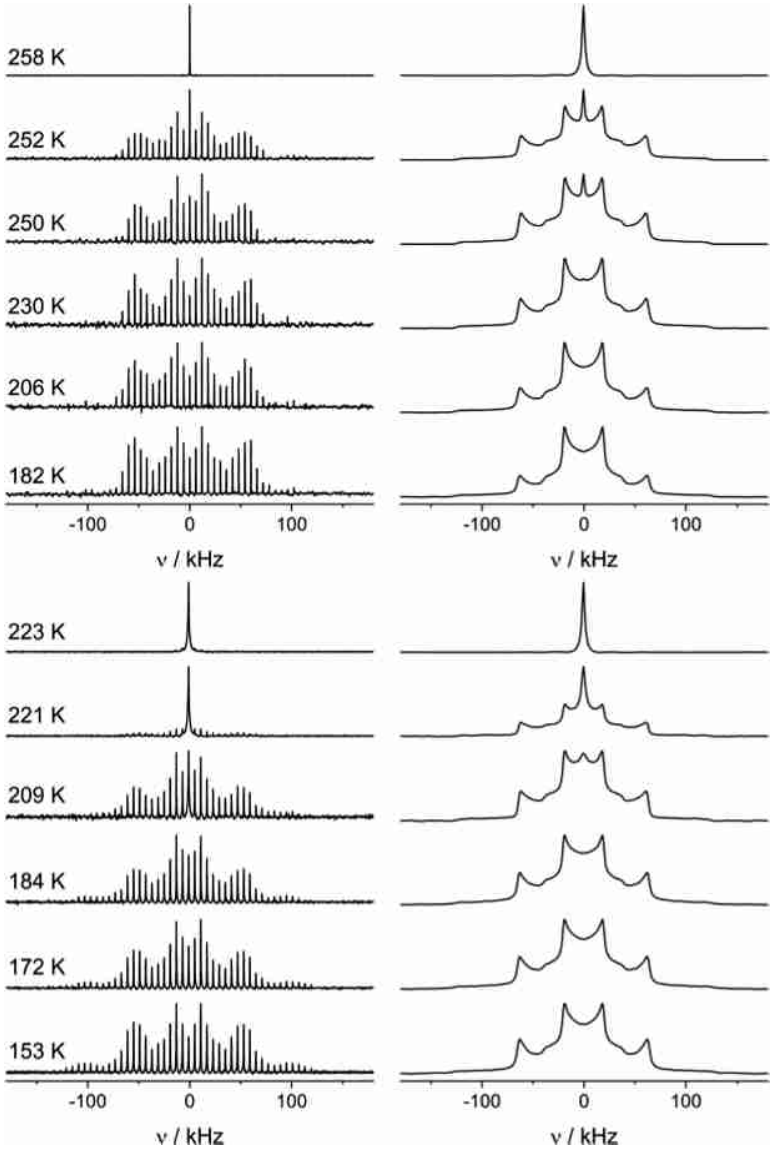

Figure 3. Select ^{2}H MAS NMR spectra (left side) and solid-echo ^{2}H spectra (right side) of bulk octanol-d_{17} (top row) and octanol-d_{17} confined in mesoporous SBA-15 (bottom row). Temperatures are indicated in the figure. All spectra are normalized to an equal height.

d_{17} layer close to the mesoporous material. However, toward the pore center, this order is unlikely to persist, possibly resulting in a strongly disordered, partially amorphous, or glasslike portion of the molecules.[10,52,53]

^{2}H NMR Spectra. Figure 3 shows a selection of the recorded ^{2}H NMR spectra to provide an overview of the effect of temperature on the spectral shapes. In this work, both MAS and static spectra are recorded so that as much information as possible are gathered on the molecular dynamics. Both experiments are echo experiments; however, the echo does not appear on the same time scale in both cases, possibly leading to different parts of the molecular dynamics being observable with different experiments. The MAS experiments have the big advantage that they are much faster compared to the solid-echo experiments (typically about 2 min versus 4 h of measuring time) per spectrum in our systems; the solid-echo experiments are more sensitive toward the detection of faster relaxing species.

https://doi.org/10.1021/acs.jpcc.1c05873
J. Phys. Chem. C 2021, 125, 25155−25164

The line shape of the experimental spectra results from a superposition of different spectral components. For the ^{2}H MAS NMR spectra, a large and a small Pake pattern are visible, with a Lorentzian signal emerging close to the melting point of the respective compound. The static spectra also display the Pake patterns as well as the Lorentzian signal close to the melting point. However, upon fitting these spectra, an additional component can be observed below the temperatures of 195 K for bulk octanol-d_{17} and 170 K for octanol-d_{17} in SBA-15 (shown exemplarily in Figure 4). This signal shows

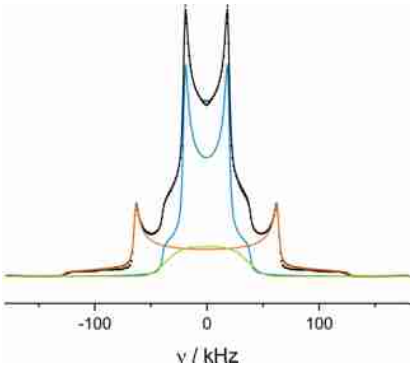

Figure 4. Solid-echo ^{2}H NMR spectrum of bulk octanol-d_{17} at 150 K with the overall fit (black solid line) and the fits of the different components (blue: narrow Pake pattern, orange: broad Pake pattern, green: broad non-Pake signal).

neither a Pake pattern nor a Lorentzian shape. It probably arises due to the dynamics of the corresponding deuterons falling within the NMR time scale at these temperatures, resulting in an intermediate exchange regime and therefore distortion of the signal and intensity loss due to the echo not being refocused by the second pulse.[54,55] The time scale of the echo observation is different in the MAS spectra than in the static spectra, potentially explaining why the signal cannot be observed in the MAS spectra due to motional broadening. This signal possibly corresponds to a less ordered portion of octanol-d_{17}.[10]

The hydroxyl group of the octanol-d_{17} does not produce a signal in the ^{2}H NMR since it is not deuterated. In this work, we refrained from using octanol-d_{18} since we expect the hydroxyl group to be susceptible to exchange processes, resulting in a partial loss of deuterium at this position. This would result in an uncertainty of the extracted numerical values for the determined intensities. Having the hydroxyl group deuterated would also lead to a further complication of the spectral shapes, making it more difficult to describe the dynamics of the aliphatic moiety of the molecules.

Generally, the melting points observed in the NMR experiments agree with those determined by the DSC measurements.

Figure 5 shows the quadrupolar coupling constant, C_Q, which was extracted via numerical modeling from all recorded spectra as a function of temperature T. At 258 and 223 K, respectively, only the Lorentzian signal (i.e., $C_Q = 0$) can be observed, indicating a full melting of the sample.

The large Pake pattern shows $C_Q \approx 170$ kHz just until the melting point, a value typical for an immobile deuteron of a −CD bond.[56] The quadrupolar coupling constant of the smaller Pake pattern is obtained as $C_Q \approx 55$ kHz, suggesting

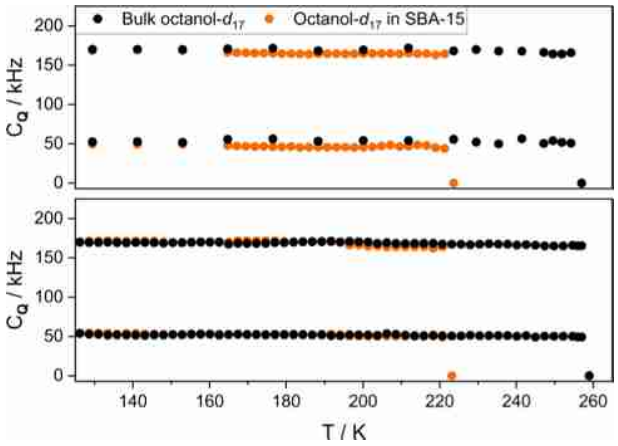

Figure 5. Values of C_Q extracted from the ^{2}H MAS spectra (top) and the static spectra (bottom) for bulk octanol-d_{17} and octanol-d_{17} in SBA-15.

that the motionally narrowed Pake pattern is caused by the CD_3-group moving around its C_3-axis in a 3-fold jump.[57] The determined values for C_Q are similar across both methods, confirming that the samples show an analogous behavior under MAS and static conditions. In addition, the octanol-d_{17} in SBA-15 does not show a considerably different quadrupolar coupling constant than the bulk octanol-d_{17}, suggesting that the vibrational dynamics in confinement are not significantly different than the dynamics in the bulk material. A detailed discussion of the influence of vibrational dynamics on the quadrupolar coupling constant is beyond the scope of this paper and can be found in the literature.[55,58] Interestingly, the quadrupolar coupling constants of the Pake patterns do not change considerably throughout the observed period, indicating that there are no changes in the dynamics of the corresponding molecules up to the melting point. This suggests that the molecules in the bulk octanol-d_{17}, as well as the octanol-d_{17} in SBA-15, are rather rigid, not allowing for an observable rotation of the entire molecule[9] or groups apart from the CD_3-group even at higher temperatures. Such dynamics would drastically alter the line shape, which cannot be observed here.[58] Considering the amphiphilic nature of the octanol-d_{17} molecule and the way it is packed when frozen in bulk[51] and when confined in mesoporous SBA-15,[10] the molecule is probably held in place by interactions of its OH-groups with each other and the OH-groups on the surface of the mesoporous silica. This results in the octanol-d_{17} being bound to the surface via hydrogen bonds with the aliphatic moiety oriented toward the pore center, preventing movement away from the surface and orienting their structure, similar to what was proposed recently by some of us.[10] This local order is transmitted to the inner parts of the pore, which also restricts the motional degrees of freedom of those octanol molecules, with the result that only the CD_3-group can perform fast rotations on the NMR time scale. Overall, it is likely that the majority of the confined octanol is in an aligned relative orientation that differs from bulk octanol based on the average pore size of about 6.5 nm (see Figure S1 in the Supporting Information) and the length of stretched n-octanol of about 1 nm based on the data supplied by crystallography.[51] Specifically, assuming the first two layers next to the pore surface are primarily structured in a bilayer form with the hydroxyl groups of the octanol layer next to surface aligned

https://doi.org/10.1021/acs.jpcc.1c05873
J. Phys. Chem. C 2021, 125, 25155−25164

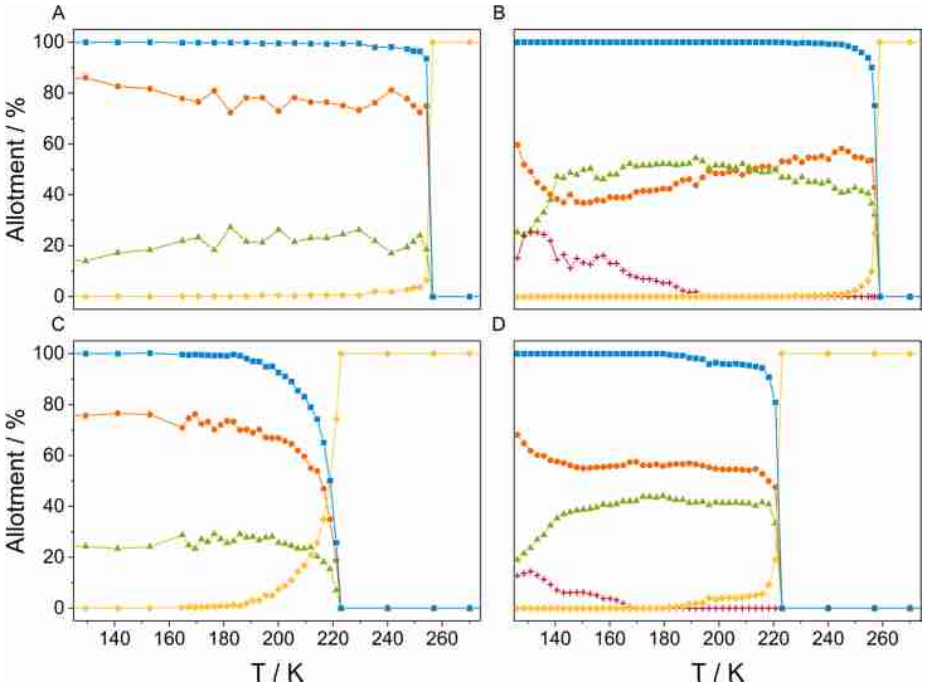

Figure 6. Relative intensities of the different components found in the samples. Orange circles: broad Pake pattern, green triangles: narrow Pake pattern, red crosses: non-Pake signal, yellow rhomb: isotropic signal, and blue squares: sum of the anisotropic signals. The non-Pake signal can only be found in the static spectra. Bulk octanol-d_{17} under MAS conditions (A), bulk octanol-d_{17} under static conditions (B), octanol-d_{17} in SBA-15 under MAS conditions (C), and octanol-d_{17} in SBA-15 under static conditions (D).

toward the surface and with opposite alignment for the second layer to maximize the hydrophobic interactions between the octanol tails, this would leave only a sphere of a diameter of 6.5 − 4 nm = 2.5 nm for the remaining octanol molecules to orient similarly as the bulk octanol does. A more detailed analysis of this model would require molecular dynamics simulations, which are beyond the scope of the present paper.

Fitting each component of the ^{2}H NMR spectra allows for a determination of the relative intensities of the respective components. Figure 6 shows the relative intensities of the solid and the liquid portions of the samples as well as all other observed spectral components (see Figure 6) as a function of the sample temperature T. The integrals of each signal can be used as a quantification of the number of deuterons, which are in the corresponding state of dynamics.

The data of bulk octanol-d_{17} (Figure 6A,B) both show an abrupt decline of the solid portion of the sample at the melting temperature, indicating a relatively quick transition between the solid and liquid phases. The spectra of the confined octanol-d_{17} (Figure 6C,D) both show an earlier onset of the melting process (about 30 K before the actual melting point) with a slow increase of the Lorentzian signal until a full melting of the sample can be observed.

The ratio of the broad and the narrow Pake patterns presented in Figure 6 can be compared to the theoretical ratios that result from the stoichiometry of the utilized octanol-d_{17}. Considering the narrow Pake pattern results from the methyl group of the aliphatic moiety of the molecule, it is expected to make up 17.6% of the observed signal, compared to 82.4% caused by the rest of the aliphatic deuterons. These ratios can only be observed at low temperatures in the bulk MAS spectra (Figure 6A, 130 K). All other spectra show a larger intensity of the signal caused by the methyl group and, in turn, a smaller signal caused by the methylene groups. These differences to the theoretical ratios are attributed to dynamics in the system. As mentioned previously, in the case of octanol-d_{17} under MAS (Figure 6A,C), the non-Pake signal cannot be observed. However, considering the presented ratios, the explanation of a signal corresponding to deuterons in the intermediate exchange regime being broadened and therefore not being observable on the MAS time scale is probable. This suspected broad signal would have its peak around the center of the spectrum, causing the observed increase of intensity (to about 25%) of the narrow Pake pattern.

A similar phenomenon is observed in the case of the static spectra. At low temperatures, they show smaller allotments than expected for the broad Pake pattern of 66% for the bulk and 74% for the confined octanol-d_{17}. However, they also display smaller ratio for the narrow Pake pattern with 13 and 12%, respectively. The rest of the signal is made up of the non-Pake component, which disappears gradually with increasing temperatures while the Lorentzian signal appears. Considering the non-Pake pattern is attributed to deuterons in the intermediate exchange regime and possibly less ordered octanol-d_{17} molecules, it is probable that these disordered molecules become mobile before the more ordered portion of molecules.[10,53] However, the intensity ratios are possibly distorted by parts of the signal not being refocused by the solid-echo pulse sequence, leading to potential loss of intensity.[55] Therefore, further investigations into the cause of the deviating intensity ratios in the static case are necessary to confirm the presented conclusion.

The differences in the melting behavior of the confined and bulk samples can be explained by the interaction of the octanol-d_{17} molecules with the surface of the mesoporous SBA-15 and the steric hindrances of the confinement. The

https://doi.org/10.1021/acs.jpcc.1c05873
J. Phys. Chem. C 2021, 125, 25155−25164

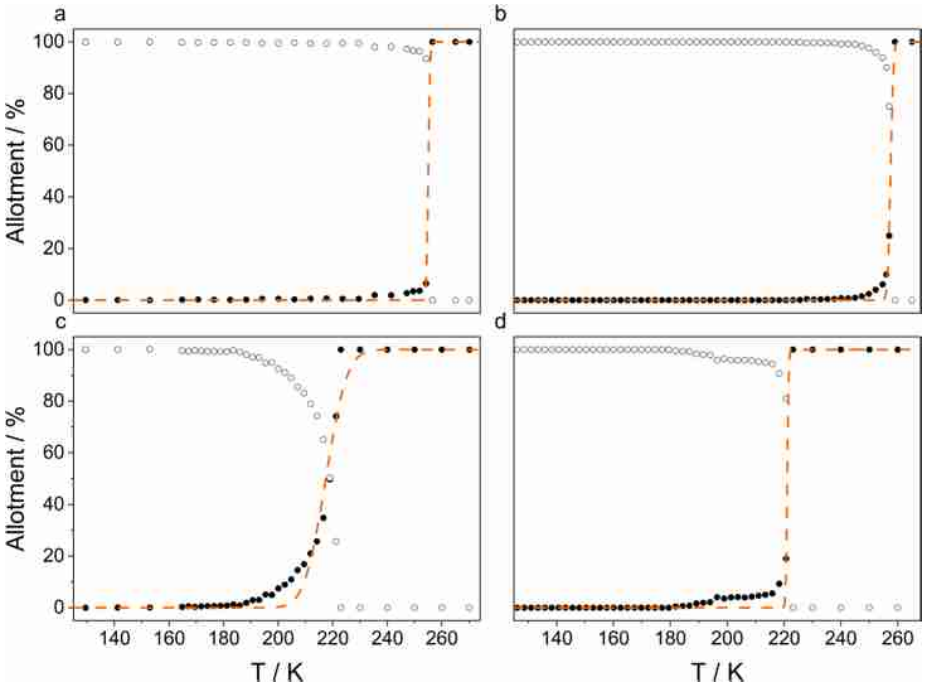

Figure 7. Relative intensities of the anisotropic (white circles) and Lorentzian parts caused by the isotropically moving molecules (solid circles) of the samples, including the calculated fits according to eq 3 (dashed line). Bulk octanol-d_{17} under MAS conditions (a), bulk octanol-d_{17} under static conditions (b), octanol-d_{17} in SBA-15 under MAS conditions (c), and octanol-d_{17} in SBA-15 under static conditions (d). Above the melting temperatures, additional points are extrapolated to stabilize the fitting procedure.

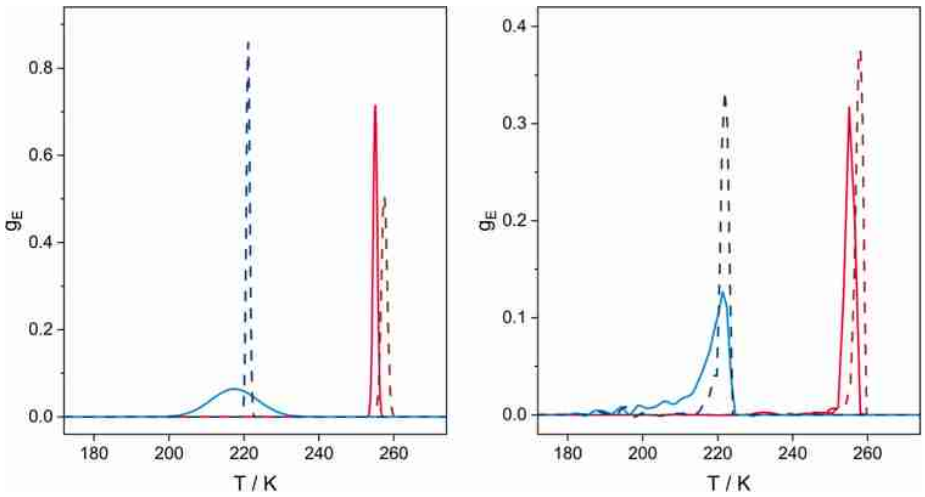

Figure 8. First derivatives of the fitting curves (left) and the experimental data (right) displayed in Figure 7 according to eq 4. Blue: octanol-d_{17} in SBA-15, red: bulk octanol-d_{17}, solid lines: MAS conditions, and dashed lines: static conditions.

confinement creates a distribution of locally different environments for the guest molecules, leading to a broad distribution of activation energies in the melting process. The fraction of molecules with lower activation energies has an earlier onset of their dynamics, therefore causing the observed changes of the intensity curves on the low-temperature side of the curves in Figure 6. We wish to note that similar dynamics occurring below the full melting point of the sample have also been observed for biphenyl.[59] However, considering the line shapes obtained from the DSC experiments, the formation of a continuous glass phase is unlikely,[60] making the formation of a glasslike pore solid the most viable explanation for the observed behavior. In these kinds of solids, the pores of the host material inhibit the formation of large, bulklike crystals, therefore lowering the equilibrium melting point of the confined material, $T_{m,c}$ in accordance with the Gibbs–Thomson equation (eq 2).[52] Equation 2 takes into account the bulk melting temperature, $T_{m,b}$, as well as the surface energy of the solid–liquid interface, σ_{sl}, the enthalpy of melting, H_m, the density of the corresponding solid, ρ, and the radius of the crystal, r, to calculate the melting point suppression ΔT_m.

https://doi.org/10.1021/acs.jpcc.1c05873
J. Phys. Chem. C 2021, 125, 25155−25164

$$\Delta T_m = T_{m,b} - T_{m,c} = T_{m,b}\frac{2\sigma_{sl}}{H_m \rho\, r} \quad (2)$$

In the case of a broad distribution of activation energies, the distribution function can be determined by fitting the relative intensities of the isotropic component according to Rössler et al.,[40] assuming in the simplest case a Gaussian distribution of activation energies g_E and employing the fraction of isotropically moving molecules c_{iso}, the melting point T_0 as the center of gravity, and ΔT as the width of the distribution (eq 3). This approach was previously used to accurately describe the dynamics of, e.g., confined benzene-d_6,[9,40] biphenyl,[59] and hexamethylbenzene-d_{18}[40] molecules.

$$c_{iso} = \int_0^T \frac{1}{\sqrt{2\pi\Delta T^2}}\exp\left(-\frac{(T-T_0)^2}{2\Delta T^2}\right)dT = \frac{1}{2}\mathrm{erf}\left(\frac{1}{\sqrt{2}\,\Delta T}(T-T_0)\right) + \frac{1}{2}\mathrm{erf}\left(\frac{1}{\sqrt{2}\,\Delta T}T_0\right) \quad (3)$$

By calculating the derivative of eq 3, a distribution of activation energies in temperature units (eq 4) is obtained.

$$g_E = \frac{d}{dT}c_{iso} = \frac{1}{\sqrt{2\pi}\,\Delta T}\exp\left(-\frac{(T-T_0)^2}{2\Delta T^2}\right) \quad (4)$$

The corresponding graphical representation of this approach is shown in Figures 7 and 8. While for glasslike systems with a clear separation between rotational and translational degrees of freedom, a direct conversion of the temperature distributions to activation energy distributions is feasible via the two-phase model developed by Rössler et al.,[40] in the present case, these degrees of freedom are coupled. Thus, the applicability of the model by Rössler et al.[40] in the present case is limited, and a detailed interpretation of the distribution curves would necessitate molecular dynamics simulations, which are beyond the scope of this paper. Therefore, Figure 8 displays the corresponding distribution in temperature units. Additionally, the derivative of the experimental data is calculated and plotted to illustrate potential differences between the idealized fit and the measured intensities.

Generally, the data presented in Figures 7 and 8 follow the expectations described earlier. The distributions of activation energies for the bulk octanol-d_{17} (obtained from Figures 7a,b and 8 left, red lines) are narrow, indicating the melting of a crystalline solid.[40] The distribution of activation energies for the confined octanol-d_{17} obtained under MAS conditions is broad (Figure 8 left, blue solid line), denoting a melting process involving species in different environments and possibly a distribution of rigidly and less rigidly ordered molecules.[16,52] On the low-temperature flanks of the obtained melting curves for the confined octanol-d_{17} (Figure 7c,d), there are clear deviations between the experimental and calculated curves, revealing a non-Gaussian distribution of activation energies and again illustrating that the used model may only be used as an approximation.

Additionally, this non-Gaussian distribution is illustrated by the numerical derivative of the experimental data (Figure 8 right), especially for the confined octanol-d_{17} under MAS conditions. For this sample, a shoulder on the low-temperature flank of the main curve is visible, indicating lower melting points for the molecules involved in the premelting process compared to the full melting.

CONCLUSIONS

In this work, DSC and ^{2}H solid-state NMR in combination with numerical modeling of the obtained data were applied to investigate the behavior of octanol-d_{17} in bulk as well as in confinement in mesoporous SBA-15 starting at 125 K, up to the melting point of the respective sample. The composition of the samples and quadrupolar coupling constants at any given temperature were determined for the MAS and the static case and used to elucidate the dynamics of the system. It could be demonstrated that both the bulk as well as the confined octanol-d_{17} are held in place by the interplay of hydrogen bonds and dispersion forces, resulting in the rotation of the CD_3-group around its C_3-axis as the only active motional degree of freedom. Differences occur in the region shortly before the melting point. Bulk octanol-d_{17} shows a behavior typical for crystalline solids, melting at once at its melting temperature. Confined octanol-d_{17} shows a slow melting process with an onset of 30 K before its melting point due to the interactions of the molecule with the rough surface of the mesoporous material, leading to a broad, non-Gaussian distribution of activation energies for the melting process. Additionally, the melting temperature of the confined octanol-d_{17} is about 38 K lower, suggesting a smaller crystallite size than in bulk in accordance with the Gibbs–Thomson equation and therefore the formation of a pore solid[52] with a potentially amorphous portion. The presented findings serve as an example of the dynamics of linear small amphiphilic organic molecules and may be applicable to similar systems like amines or carboxylic acids.

ASSOCIATED CONTENT

Supporting Information

The Supporting Information is available free of charge at https://pubs.acs.org/doi/10.1021/acs.jpcc.1c05873.

Information on utilized chemicals; nitrogen adsorption data; examples of ^{2}H MAS NMR spectra with non-absorbed octanol-d_{17}; and comparison of a symmetrized and a nonsymmetrized static ^{2}H NMR spectrum of bulk octanol-d_{17} (PDF)

AUTHOR INFORMATION

Corresponding Author

Gerd Buntkowsky − *Eduard-Zintl-Institut für Anorganische und Physikalische Chemie, Technische Universität Darmstadt, D-64287 Darmstadt, Germany*; orcid.org/0000-0003-1304-9762; Phone: +49 6151 16 21116; Email: gerd.buntkowsky@chemie.tu-darmstadt.de

Authors

Sonja C. Döller − *Eduard-Zintl-Institut für Anorganische und Physikalische Chemie, Technische Universität Darmstadt, D-64287 Darmstadt, Germany*

Martin Brodrecht − *Eduard-Zintl-Institut für Anorganische und Physikalische Chemie, Technische Universität Darmstadt, D-64287 Darmstadt, Germany*

Nadia B. Haro Mares − *Eduard-Zintl-Institut für Anorganische und Physikalische Chemie, Technische Universität Darmstadt, D-64287 Darmstadt, Germany*

Hergen Breitzke − *Eduard-Zintl-Institut für Anorganische und Physikalische Chemie, Technische Universität Darmstadt, D-64287 Darmstadt, Germany*

https://doi.org/10.1021/acs.jpcc.1c05873
J. Phys. Chem. C 2021, 125, 25155−25164

Torsten Gutmann − *Eduard-Zintl-Institut für Anorganische und Physikalische Chemie, Technische Universität Darmstadt, D-64287 Darmstadt, Germany;* orcid.org/0000-0001-6214-2272

Markus Hoffmann − *Department of Chemistry and Biochemistry, State University of New York College at Brockport, Brockport, New York 14420, United States;* orcid.org/0000-0002-5469-8665

Complete contact information is available at: https://pubs.acs.org/10.1021/acs.jpcc.1c05873

Notes

The authors declare no competing financial interest.

■ ACKNOWLEDGMENTS

Financial support by the Deutsche Forschungsgemeinschaft under Contract Bu-911-24-2 and by the National Science Foundation under Grant No. 1953428 are gratefully acknowledged.

■ REFERENCES

(1) Andanson, J.-M.; Baiker, A. Exploring Catalytic Solid/Liquid Interfaces by in Situ Attenuated Total Reflection Infrared Spectroscopy. *Chem. Soc. Rev.* **2010**, *39*, 4571−4584.
(2) François, I.; Sandra, K.; Sandra, P. Comprehensive Liquid Chromatography: Fundamental Aspects and Practical Considerations—a Review. *Anal. Chim. Acta* **2009**, *641*, 14−31.
(3) Zhou, P.; Yao, L.; Chen, K.; Su, B. Silica Nanochannel Membranes for Electrochemical Analysis and Molecular Sieving: A Comprehensive Review. *Crit. Rev. Anal. Chem.* **2020**, *50*, 424−444.
(4) Murillo-Cremaes, N.; López-Periago, A. M.; Saurina, J.; Roig, A.; Domingo, C. Nanostructured Silica-based Drug Delivery Vehicles for Hydrophobic and Moisture Sensitive Drugs. *J. Supercrit. Fluids* **2013**, *73*, 34−42.
(5) Ahmaruzzaman, M. Industrial Wastes as Low-Cost Potential Adsorbents for the Treatment of Wastewater Laden with Heavy Metals. *Adv. Colloid Interface Sci.* **2011**, *166*, 36−59.
(6) Sun, B.; Zhou, G.; Zhang, H. Synthesis, Functionalization, and Applications of Morphology-controllable Silica-based Nanostructures: A Review. *Prog. Solid State Chem.* **2016**, *44*, 1−19.
(7) Zhao, D.; Feng, J.; Huo, Q.; Melosh, N.; Fredrickson, G. H.; Chmelka, B. F.; Stucky, G. D. Triblock Copolymer Syntheses of Mesoporous Silica with Periodic 50 to 300 Angstrom Pores. *Science* **1998**, *279*, 548−552.
(8) Beck, J. S.; Vartuli, J. C.; Roth, W. J.; Leonowicz, M. E.; Kresge, C. T.; Schmitt, K. D.; Chu, C. T. W.; Olson, D. H.; Sheppard, E. W.; McCullen, S. B.; et al. A New Family of Mesoporous Molecular Sieves Prepared with Liquid Crystal Templates. *J. Am. Chem. Soc.* **1992**, *114*, 10834−10843.
(9) Gedat, E.; Schreiber, A.; Albrecht, J.; Emmler, T.; Shenderovich, I.; Findenegg, G. H.; Limbach, H.-H.; Buntkowsky, G. 2H-Solid-State NMR Study of Benzene-d6 Confined in Mesoporous Silica SBA-15. *J. Phys. Chem. B* **2002**, *106*, 1977−1984.
(10) Kumari, B.; Brodrecht, M.; Breitzke, H.; Werner, M.; Grünberg, B.; Limbach, H.-H.; Forg, S.; Sanjon, E. P.; Drossel, B.; Gutmann, T.; et al. Mixtures of Alcohols and Water confined in Mesoporous Silica: A Combined Solid-State NMR and Molecular Dynamics Simulation Study. *J. Phys. Chem. C* **2018**, *122*, 19540−19550.
(11) Buntkowsky, G.; Breitzke, H.; Adamczyk, A.; Roelofs, F.; Emmler, T.; Gedat, E.; Grünberg, B.; Xu, Y.; Limbach, H.-H.; Shenderovich, I.; et al. Structural and Dynamical Properties of Guest Molecules Confined in Mesoporous Silica Materials Revealed by NMR. *Phys. Chem. Chem. Phys.* **2007**, *9*, 4843−4853.
(12) Hassan, J. Analysis of 2H NMR Spectra of Water Molecules on the Surface of Nano-silica Material MCM-41: Deconvolution of the Signal Into a Lorentzian and a Powder Pattern Line Shapes. *Phys. B* **2012**, *407*, 179−183.
(13) Ben Shir, I.; Kababya, S.; Schmidt, A. Binding Specificity of Amino Acids to Amorphous Silica Surfaces: Solid-State NMR of Glycine on SBA-15. *J. Phys. Chem. C* **2012**, *116*, 9691−9702.
(14) Amitay-Rosen, T.; Vega, S. A Deuterium MAS NMR Study of the Local Mobility of Dissolved Methionine and di-Alanine at the Inner Surface of SBA-15. *Phys. Chem. Chem. Phys.* **2010**, *12*, 6763−6773.
(15) Amitay-Rosen, T.; Kababya, S.; Vega, S. A Dynamic Magic Angle Spinning NMR Study of the Local Mobility of Alanine in an Aqueous Environment at the Inner Surface of Mesoporous Materials. *J. Phys. Chem. B* **2009**, *113*, 6267−6282.
(16) Dosseh, G.; Xia, Y.; Alba-Simionesco, C. Cyclohexane and Benzene Confined in MCM-41 and SBA-15: Confinement Effects on Freezing and Melting. *J. Phys. Chem. B* **2003**, *107*, 6445−6453.
(17) Alba-Simionesco, C.; Coasne, B.; Dosseh, G.; Dudziak, G.; Gubbins, K. E.; Radhakrishnan, R.; Sliwinska-Bartkowiak, M. Effects of Confinement on Freezing and Melting. *J. Phys.: Condens. Matter* **2006**, *18*, R15−R68.
(18) Palombo, F.; Sassi, P.; Paolantoni, M.; Morresi, A.; Cataliotti, R. S. Comparison of Hydrogen Bonding in 1-Octanol and 2-Octanol as Probed by Spectroscopic Techniques. *J. Phys. Chem. B* **2006**, *110*, 18017−18025.
(19) Hu, K.; Zhou, Y.; Shen, J.; Ji, Z.; Cheng, G. Micro-heterogeneous Structure of 1-Octanol in Neat and Water-Saturated State. *J. Phys. Chem. B* **2007**, *111*, 10160−10165.
(20) Franks, N. P.; Abraham, M. H.; Lieb, W. R. Molecular Organization of Liquid n-Octanol: An X-ray Diffraction Analysis. *J. Pharm. Sci.* **1993**, *82*, 466−470.
(21) Huyskens, P.; Ruelle, P. Dynamic Equilibrium Time Fractions or Fractional Lifetimes? The Final Chapter. *J. Mol. Liq.* **2000**, *88*, 87−108.
(22) de Oliveira, C. A. F.; Guimarães, C. R. W.; Bicca de Alencastro, R. Molecular Dynamics Study on Liquid 1-Octanol. Part 2. Water-Saturated 1-Octanol Solution. *Int. J. Quantum Chem.* **2002**, *90*, 786−791.
(23) Chen, B.; Siepmann, J. I. Microscopic Structure and Solvation in Dry and Wet Octanol. *J. Phys. Chem. B* **2006**, *110*, 3555−3563.
(24) Marcus, Y. Structural Aspects of Water in 1-Octanol. *J. Solution Chem.* **1990**, *19*, 507−517.
(25) Zana, R.; Talmon, Y. Dependence of Aggregate Morphology on Structure of Dimeric Surfactants. *Nature* **1993**, *362*, 228−230.
(26) Kancharla, S.; Canales, E.; Alexandridis, P. Perfluorooctanoate in Aqueous Urea Solutions: Micelle Formation, Structure, and Microenvironment. *Int. J. Mol. Sci.* **2019**, *20*, 5761−5778.
(27) Manne, S.; Gaub, H. E. Molecular Organization of Surfactants at Solid-Liquid Interfaces. *Science* **1995**, *270*, 1480−1482.
(28) Lamont, R. E.; Ducker, W. A. Surface-Induced Transformations for Surfactant Aggregates. *J. Am. Chem. Soc.* **1998**, *120*, 7602−7607.
(29) Zaera, F. Probing Liquid/Solid Interfaces at the Molecular Level. *Chem. Rev.* **2012**, *112*, 2920−2986.
(30) Hind, A. R.; Bhargava, S. K.; McKinnon, A. At the Solid/Liquid Interface: Ftir/Atr — the Tool of Choice. *Adv. Colloid Interface Sci.* **2001**, *93*, 91−114.
(31) Zou, S.; Williams, C. T.; Chen, E. K.-Y.; Weaver, M. J. Probing Molecular Vibrations at Catalytically Significant Interfaces: A New Ubiquity of Surface-Enhanced Raman Scattering. *J. Am. Chem. Soc.* **1998**, *120*, 3811−3812.
(32) Raposo, M.; Pontes, R. S.; Mattoso, L. H. C.; Oliveira, O. N. Kinetics of Adsorption of Poly(o-methoxyaniline) Self-Assembled Films. *Macromolecules* **1997**, *30*, 6095−6101.
(33) Serrano, A. G.; Cabré, E. J.; Oviedo, J. M.; Cruz, A.; González, B.; Palacios, A.; Estrada, P.; Pérez-Gil, J. Production in Escherichia Coli of a Recombinant C-terminal Truncated Precursor of Surfactant Protein B (Rprosp-b Delta C). Structure and Interaction With Lipid Interfaces. *Biochim. Biophys. Acta, Biomembr.* **2006**, 1621−1632.

(34) Fenter, P.; Sturchio, N. C. Mineral-water Interfacial Structures Revealed by Synchrotron X-ray Scattering. *Prog. Surf. Sci.* **2004**, *77*, 171−258.
(35) Alba-Simionesco, C.; Dosseh, G.; Dumont, E.; Frick, B.; Geil, B.; Morineau, D.; Teboul, V.; Xia, Y. Confinement of Molecular Liquids: Consequences on Thermodynamic, Static and Dynamical Properties of Benzene and Toluene. *Eur. Phys. J. E* **2003**, *12*, 19−28.
(36) Werner, M.; Rothermel, N.; Breitzke, H.; Gutmann, T.; Buntkowsky, G. Recent Advances in Solid State NMR of Small Molecules in Confinement. *Isr. J. Chem.* **2014**, *54*, 60−73.
(37) de Oliveira, C. A. F.; Guimares, C. R. W.; de Alencastro, R. B. Molecular Dynamics Study on Liquid 1-Octanol. *Int. J. Quantum Chem.* **2000**, *80*, 999−1006.
(38) Sassi, P.; Paolantoni, M.; Cataliotti, R. S.; Palombo, F.; Morresi, A. Water/Alcohol Mixtures: A Spectroscopic Study of the Water-Saturated 1-Octanol Solution. *J. Phys. Chem. B* **2004**, *108*, 19557−19565.
(39) Kissinger, H. E. Variation of Peak Temperature With Heating Rate In Differential Thermal Analysis. *J. Res. Natl. Bur. Stand.* **1956**, *57*, 217−221.
(40) Rössler, E.; Taupitz, M.; Börner, K.; Schulz, M.; Vieth, H.-M. A Simple Method Analyzing 2H Nuclear Magnetic Resonance Line Shapes to Determine the Activation Energy Distribution of Mobile Guest Molecules in Disordered Systems. *J. Chem. Phys.* **1990**, *92*, 5847−5855.
(41) Buntkowsky, G.; Vogel, M. Small Molecules, Non-Covalent Interactions, and Confinement. *Molecules* **2020**, *25*, 3311−3343.
(42) Brodrecht, M.; Breitzke, H.; Gutmann, T.; Buntkowsky, G. Biofunctionalization of Nano Channels by Direct In-Pore Solid-Phase Peptide Synthesis. *Chem. - Eur. J.* **2018**, *24*, 17814−17822.
(43) Wang, X.; Lin, K. S. K.; Chan, J. C. C.; Cheng, S. Direct Synthesis and Catalytic Applications of Ordered Large Pore Aminopropyl-Functionalized SBA-15 Mesoporous Materials. *J. Phys. Chem. B* **2005**, *109*, 1763−1769.
(44) Brunauer, S.; Emmett, P. H.; Teller, E. Adsorption of Gases in Multimolecular Layers. *J. Am. Chem. Soc.* **1938**, *60*, 309−319.
(45) Klyachko-Gurvich, A. L. An Improved Method of Determining Surface Area by the Adsorption of Air. *Bull. Acad. Sci. USSR, Div. Chem. Sci.* **1961**, *10*, 1756−1758.
(46) Barrett, E. P.; Joyner, L. G.; Halenda, P. P. The Determination of Pore Volume and Area Distributions in Porous Substances. I. Computations from Nitrogen Isotherms. *J. Am. Chem. Soc.* **1951**, *73*, 373−380.
(47) Bielecki, A.; Burum, D. P. Temperature Dependence of 207 Pb MAS Spectra of Solid Lead Nitrate. An Accurate, Sensitive Thermometer for Variable-Temperature MAS. *J. Magn. Reson., Ser. A* **1995**, *116*, 215−220.
(48) Massiot, D.; Fayon, F.; Capron, M.; King, I.; Le Calvé, S.; Alonso, B.; Durand, J.-O.; Bujoli, B.; Gan, Z.; Hoatson, G. Modelling One- and Two-dimensional Solid-state NMR Spectra. *Magn. Reson. Chem.* **2002**, *40*, 70−76.
(49) Vyazovkin, S. Is the Kissinger Equation Applicable to the Processes that Occur on Cooling? *Macromol. Rapid Commun.* **2002**, *23*, 771−775.
(50) Xia, Y.; Dosseh, G.; Morineau, D.; Alba-Simionesco, C. Phase Diagram and Glass Transition of Confined Benzene. *J. Phys. Chem. B* **2006**, *110*, 19735−19744.
(51) Shallard-Brown, H. A.; Watkin, D. J.; Cowley, A. R. n-Octanol. *Acta Crystallogr., Sect. E: Struct. Rep. Online* **2005**, *61*, o213−o214.
(52) Jackson, C. L.; McKenna, G. B. The Melting Behavior of Organic Materials Confined in Porous Solids. *J. Chem. Phys.* **1990**, *93*, 9002−9011.
(53) Wallacher, D.; Knorr, K. Melting and Freezing of Ar in Nanopores. *Phys. Rev. B* **2001**, *63*, No. 104202.
(54) Beshah, K.; Olejniczak, E. T.; Griffin, R. G. Deuterium NMR Study of Methyl Group Dynamics in L-alanine. *J. Chem. Phys.* **1987**, *86*, 4730−4736.
(55) Spiess, H.; Sillescu, H. Solid Echoes in the Slow-Motion Region. *J. Magn. Reson.* **1981**, *42*, 381−389.
(56) Millett, F. S.; Dailey, B. P. NMR Determination of Some Deuterium Quadrupole Coupling Constants in Nematic Solutions. *J. Chem. Phys.* **1972**, *56*, 3249−3256.
(57) Polson, J. M.; Fyfe, J. D. D.; Jeffrey, K. R. The Reorientation of t-Butyl Groups in Butylated Hydroxytoluene: A Deuterium Nuclear Magnetic Resonance Spectral and Relaxation Time Study. *J. Chem. Phys.* **1991**, *94*, 3381−3388.
(58) Schmidt-Rohr, K.; Spiess, H. W. *Multidimensional Solid-State NMR and Polymers*; Academic Press: London, 2005.
(59) de Sousa Amadeu, N.; Grünberg, B.; Frydel, J.; Werner, M.; Limbach, H.-H.; Breitzke, H.; Buntkowsky, G. Melting of Low Molecular Weight Compounds in Confinement Observed by 2H-Solid State NMR: Biphenyl, a Case Study. *Z. Phys. Chem.* **2012**, *226*, 1169−1186.
(60) Gill, P.; Moghadam, T. T.; Ranjbar, B. Differential Scanning Calorimetry Techniques: Applications in Biology and Nanoscience. *J. Biomol. Tech.* **2010**, *21*, 167−193.

https://doi.org/10.1021/acs.jpcc.1c05873
J. Phys. Chem. C 2021, 125, 25155−25164

Electronic Supporting Information

Deuterium NMR Studies of the Solid-Liquid Phase Transition of Octanol-d_{17} Confined in SBA-15

*Sonja C. Döller,[a] Martin Brodrecht,[a] Nadia B. Haro Mares,[a] Hergen Breitzke,[a] Torsten Gutmann,[a] Markus Hoffmann,[b] Gerd Buntkowsky[a]**

a) Eduard-Zintl-Institut für Anorganische und Physikalische Chemie, Technische Universität Darmstadt, Alarich-Weiss-Str. 8, D-64287 Darmstadt, Germany

b) Department of Chemistry and Biochemistry, State University of New York College at Brockport, Brockport, NY, 14420, USA

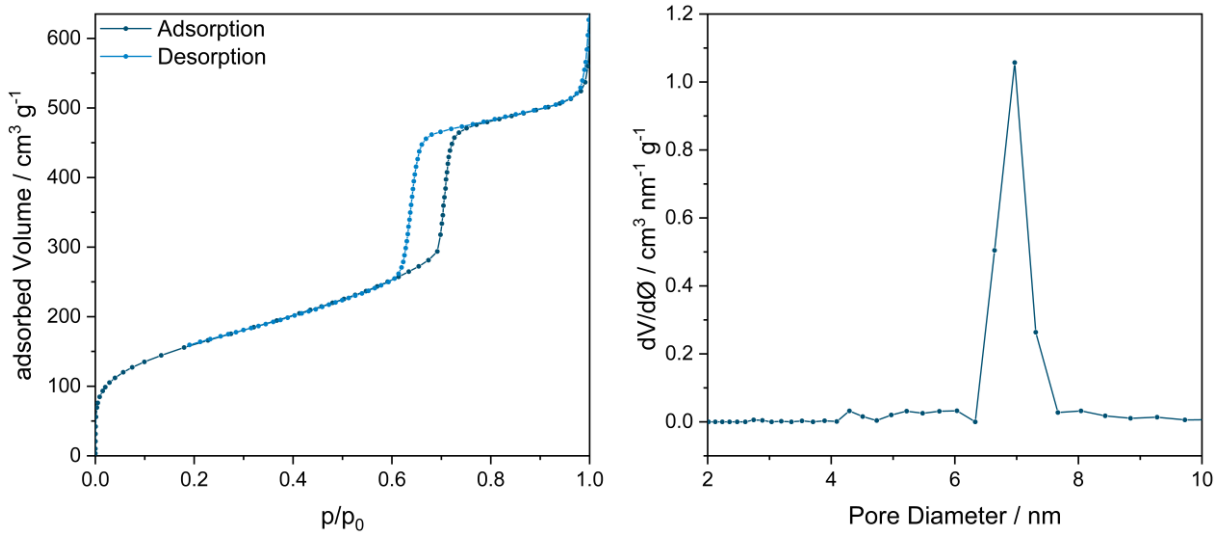

Figure S1: Nitrogen adsorption-desorption isotherms of the synthesized mesoporous SBA-15 (left) and BJH plot of the synthesized mesoporous SBA-15 (right).

Table S1: Information on the utilized chemicals.

Chemical Name	CAS	Source	Mass Fraction Purity
Octanol-d_{17}	153336-13-1	Cambridge Isotopes	> 0.98
Water	7732-18-5	VWR	> 0.99[a]
Tetraethyl orthosilicate	78-10-4	ACROS Organics	0.98
Pluronic P123	9003-11-6	Sigma-Aldrich	Not applicable[b]
HCl (37.0 %)	7647-01-0	Carl Roth	36.5-38.0 %

[a] HiPerSolv CHROMANORM for HPLC - super gradient grade

[b] Average M_n ~5,800; PEG, composition: 30 wt. %; feed ratio: 20:70:20 (EO:PO:EO)

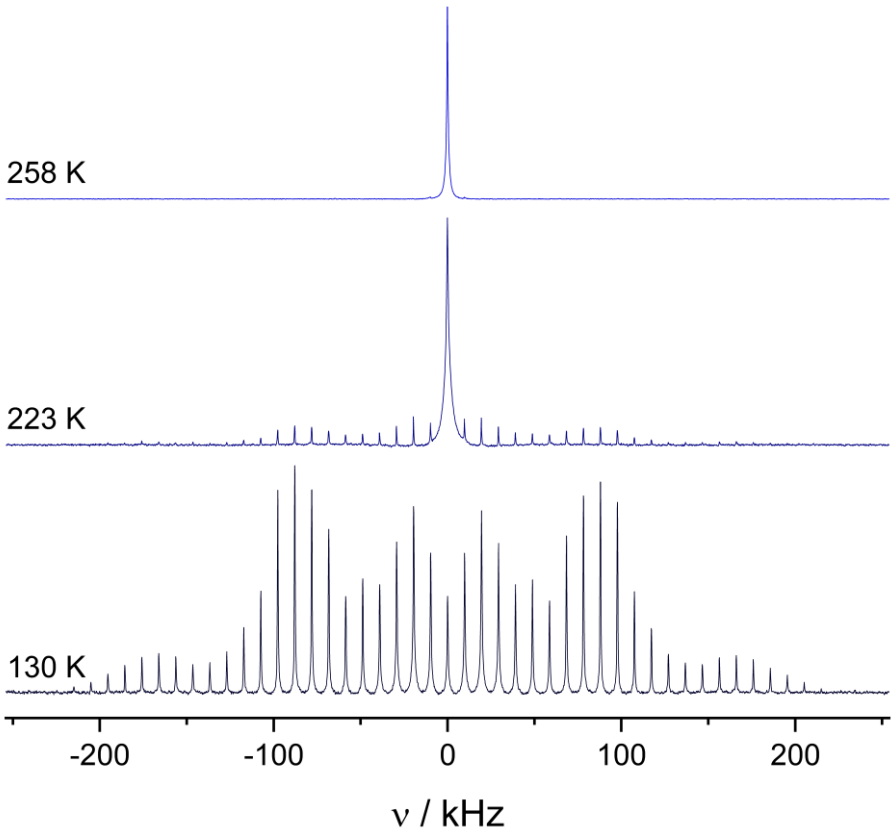

Figure S2: Examples of ^{2}H MAS NMR spectra containing confined and non-confined octanol-d_{17}. Please note the additional signals at the melting point of the confined octanol-d_{17} (223 K), indicating the presence of non-confined octanol-d_{17} in the sample. These signals disappear at the melting point of bulk octanol-d_{17} (258 K).

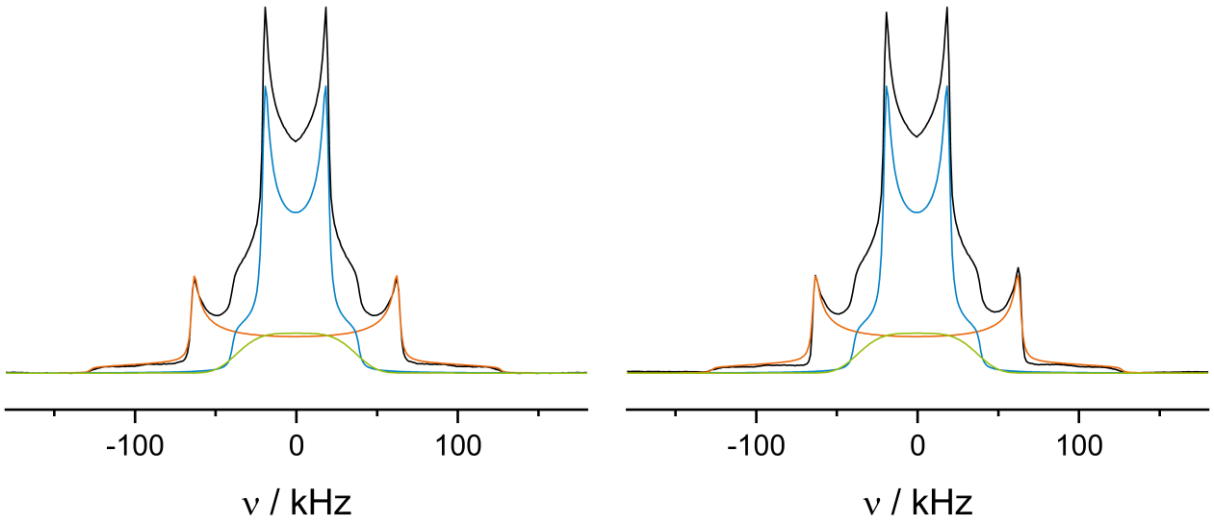

Figure S3: Solid echo ^{2}H NMR spectra of bulk octanol-d17 at 150 K (left: symmetrized spectrum, right: original spectrum) and the fits of the different components (blue: narrow Pake pattern, orange: broad Pake pattern, green: broad non-Pake signal). The overall fit has been omitted for clarity.

4.2 Defining and Quantifying Polarization Transfer Pathways through Direct and Indirect DNP Enhanced NMR Measurements on Bulk Octanol

The utilization of PAs in order to enhance signal intensity in DNP enhanced NMR spectroscopy is an established method. However, the choice of PA is oftentimes governed by the matrix used and not necessarily dependent on which analyte is investigated.[207] This is not ideal as it can actively hinder the successful transfer of polarization by compromising the contact of the analyte with the PA. This is especially apparent in the field of biomolecular ssNMR. Biological systems like peptides, proteins or RNA assemblies are oftentimes highly complex while being notoriously hard to probe with conventional methods due to their low concentration or their reluctance to crystallize.[208] At the same time, the function of these systems is inherently rooted in their structures, making their elucidation a key factor in understanding their operation. Additionally, the development of pharmaceuticals usually relies on insights into the targeted structure in order to enable rational drug design.[209] One possible approach to facilitate the elucidation of biomolecular structures is targeted DNP (tDNP) NMR spectroscopy.[208] In this method, a PA is linked to the investigated structure through either covalent linkers or through non-covalent interactions. This allows for the selective observation of specific molecules in complex environments or the investigation of protein-ligand-interactions.[208] Nevertheless, this approach harbors the risk of accidental modification of the target structure through the introduction of the PA, making its application difficult and not necessarily suitable for all systems.[188]

In this case, the method of direct/indirect DNP enhanced ssNMR can be utilized in order to gather insights into the structure of e.g. proteins[68] or RNA aptamers[56] and the manner in which their ligands bind to them. Previous studies have thereby shown that the polarization transfer pathways show a dependency on the PA, necessitating further investigations into the nature of the phenomenon.[210] Besides its general function as a surfactant and as model for the relationship between lipophilicity and hydrophilicity of a substance, *n*-octanol is routinely used as a membrane mimetic,[211] making it ideally suitable as a model system for investigations of the interactions of PAs with biologically relevant analyte molecules. Hence, it was used in this work in combination with four different, commercially available PAs to elucidate the manner in which polarization spreads through the sample. To compare the different systems, a novel approach for the analysis of direct/indirect DNP enhanced NMR spectra was developed, omitting the need to account for radical concentration or sample amount. This enabled the visualization of the different polarization transfer pathways for the hydrophilic as well as for the hydrophobic moiety of the molecule, providing valuable insights into how the PAs interact with these environments. It could be demonstrated that hydrophilicity plays a key role in how polarization is transferred. It could also be shown that PA rigidity influences the local analyte molecule arrangement, potentially disturbing supramolecular structures. Additionally, buildup times were determined for all PAs and for both the hydrophilic as well as the hydrophobic moiety of the *n*-octanol, confirming the findings of the DNP enhanced ssNMR spectroscopy.

Reprinted with permission from S. C. Döller, T. Gutmann, M. Hoffmann and G. Buntkowsky, *Solid State Nucl. Magn. Reson.*, **2022**, *122*, 101829–101837. Copyright 2022 Elsevier.

Solid State Nuclear Magnetic Resonance 122 (2022) 101829

Contents lists available at ScienceDirect

Solid State Nuclear Magnetic Resonance

journal homepage: www.elsevier.com/locate/ssnmr

A case study on the influence of hydrophilicity on the signal enhancement by dynamic nuclear polarization

Sonja C. Döller [a], Torsten Gutmann [a], Markus Hoffmann [b], Gerd Buntkowsky [a,*]

[a] Eduard-Zintl-Institut für Anorganische und Physikalische Chemie, Technische Universität Darmstadt, Alarich-Weiss-Str. 8, D-64287, Darmstadt, Germany
[b] Department of Chemistry and Biochemistry, State University of New York College at Brockport, Brockport, NY, 14420, USA

ARTICLE INFO

Dedicated to the memory of our friend and colleague Shimon Vega 1943-2021

Keywords:
Solid state NMR
DNP NMR
Low temperature NMR
Dynamics
Surfactants
Octanol

ABSTRACT

In this work, the behavior of four different commercially available polarizing agents is investigated employing the non-ionic model surfactant 1-octanol as analyte. A relative method for the comparison of the proportion of the direct and indirect polarization transfer pathways is established, allowing a direct comparison of the polarization efficacy for different radicals and different parts of the 1-octanol molecule despite differences in radical concentration or sample amount. With this approach, it could be demonstrated that the hydrophilicity is a key factor in the way polarization is transferred from the polarizing agent to the analyte. These findings are confirmed by the determination of buildup times T_b, illustrating that the choice of polarizing agent plays an essential role in ensuring an optimal polarization transfer and therefore the maximum amount of enhancement possible for DNP enhanced NMR measurements.

1. Introduction

The observation of processes that take place in living cells has been an objective of generations of molecular biologists and biochemists. Cells are complex structural units and cellular processes might not proceed the same way as when the corresponding compounds are studied in isolated form. So far, noninvasive procedures such as fluorescence based approaches [1–3], infrared (IR) spectroscopy [4], Raman spectroscopy [5] and nuclear magnetic resonance (NMR) spectroscopy are the most efficient techniques for observing dynamics and chemistry in cells. In-cell NMR spectroscopy has the advantage of being the only technique which allows studying the behavior of cellular components at atomic resolution [6] and therefore continues to be the preferred approach for finding experimental answers to a plethora of different scientific questions [6,7]. However, NMR spectroscopy suffers from its inherently low sensitivity, which is further amplified by the usually low concentrations of the biological compounds of interest as well as the observed heteronuclei, which exhibit a low gyromagnetic ratio [8–10]. Part of this issue is typically overcome with isotopic labelling [6–8], which allows to filter the desired signals against the usually suboptimal signal-to-noise-ratio caused by the biological matrix the probed molecule is located in. However, labelling a molecule with a NMR-active nucleus like ^{13}C or ^{15}N often requires elaborate synthetical efforts [11] which, depending on the location of the label, can be a tedious process. Additionally, at the low concentrations of physiologically relevant molecules, isotopic labelling alone often does not suffice to achieve adequate signal intensity.

Therefore, other specific NMR techniques that enable a sensitivity boost are of interest. Here, dynamic nuclear polarization (DNP) enhanced NMR spectroscopy has proven to be a powerful technique to enhance signals in biological systems [8,9,12,13], allowing for the observation of analytes at low concentration. In this context, dissolution DNP is typically used for investigations of biological samples since it facilitates DNP enhanced NMR experiments at room temperature and thus close to physiological conditions [8,12,14,15]. However, since the process of dissolution DNP is to a great extent irreversible due to the rapid sample dissolution in warm solvents and the polarization slowly decaying without any possibility for a de novo hyperpolarization, many biological samples continue to be investigated by DNP enhanced solid state NMR (ssNMR) at low temperatures (about 100 K). DNP enhanced ssNMR is especially the method of choice for analytes too large for fast molecular tumbling in solution, which also lack a long-range order and therefore cannot reasonably be investigated by X-ray methods [16], such as proteins [13,17–20] or structures that result of a supramolecular

* Corresponding author.
E-mail address: gerd.buntkowsky@chemie.tu-darmstadt.de (G. Buntkowsky).

https://doi.org/10.1016/j.ssnmr.2022.101829
Received 29 June 2022; Received in revised form 25 August 2022; Accepted 7 September 2022
Available online 12 September 2022
0926-2040/© 2022 Elsevier Inc. All rights reserved.

assembly of smaller molecules [21–23].

A polarization agent possessing unpaired electrons, such as mono or bi-radical organic compounds or high spin metal ions, need to be present in the sample for DNP enhanced NMR experiment to induce polarization transfer through cross-relaxation processes to the analyte molecules during DNP enhanced NMR experiments [14].

In recent years, the discovery of the indirect polarization transfer [24,25], which is mediated by spontaneous ^{1}H–^{13}C cross-relaxation within molecular groups displaying sufficient dynamics for the nuclear Overhauser effect (NOE) type effect to operate [26], has made it feasible to investigate dynamics of biological relevant systems such as amino acids [27], aptamers [28], peptides [29] and proteins [29]. Through the application of a specialized pulse sequence, the contribution of the direct and the indirect polarization transfer can be deconvoluted to yield a set of two spectra, showing only the signals caused by the direct or the indirect polarization transfer pathway, respectively [24,25,30]. This allows for the selective enhancement of the signals of mobile groups like methyl [27] and amino groups [30], or for the investigation of molecular dynamics in solids [31,32].

The location of the polarizing agent relative to the analyte molecule and the resulting intermolecular interactions with the analyte play a key role in the way the polarization is transferred to the analyte [33]. Occasionally, the polarizing agent is attached to a certain part of the analyte [34] or its environment [35], although this is not the case in most works [13]. Hence, it is fundamentally important to choose a polarization agent that is able to reach the analyte, ensuring proper interaction between the two to obtain an optimal signal enhancement [36].

In this work, four different commonly employed polarizing agents, namely AMUPol, TOTAPOL, bTbK and AsymPol (see Fig. 1), are investigated *via* DNP enhanced ssNMR towards their behavior in 1-octanol. 1-octanol was chosen because it serves as a membrane mimetic and provides the ideal amphiphilic properties to elucidate the polarizing agents' affinity towards different chemical environments [37,38]. $^{1}H \rightarrow {}^{13}C$ CP MAS ssNMR spectra are recorded to estimate the enhancement factors for each sample. To probe the polarizing agent's location, ^{13}C MAS DNP enhanced ssNMR measurements are performed and the direct and indirect polarization transfer pathways [25] are analyzed for the methylene carbon in proximity to the hydroxyl group, C_1, and the methyl carbon, C_8. Since the ratio of direct *vs*. indirect pathway polarization is directly influenced by the proximity of the radical to the analyte, the location of the radical in relation to the amphiphilic 1-octanol molecule can be derived, therefore allowing the prediction of the respective polarizing agent's affinity towards certain sites of analytes in future samples. The findings of this analysis are then compared to the buildup times (T_b) of the observed carbons for each sample.

The rest of the work is organized as follows: First, the experimental section summarizes the DNP sample preparation and the applied measurement parameters utilized to record ^{13}C CP MAS DNP NMR spectra as well as the aforementioned saturation recovery sequences at different builtup times. Subsequently, the findings of the direct *vs*. indirect polarization transfer pathway analysis as well as the results of the determination of the relevant buildup times T_b times are presented and discussed. The conclusions section provides a summary of the key findings and a discussion of their applicability.

2. Materials and methods

2.1. General

All chemicals were used as received. The anhydrous 1-octanol was purchased from Acros Organics and stored in a glove box under argon to prevent absorption of atmospheric water. AMUPol was purchased from CortecNet, AsymPol was donated to us by the Senker group from Bayreuth University, TOTAPOL was purchased from Dynupol and bTbK was donated to us by Ouari and coworkers from Aix-Marseille University. All radicals were stored in the freezer to prevent degradation.

2.2. Sample preparation for DNP NMR experiments

Apart from bTbK, all utilized polarizing agents were dissolved into the 1-octanol in small glass vials by manual agitation of the closed vial until all solids had dissolved and a clear solution had formed. This process usually took 10–15 min. For bTbK, the obtained suspension was shaken until no further changes in the amount of solid radical was observed. Then, the suspension was filtered through a syringe filter to remove any residual solids, obtaining a clear solution. It is estimated that about half of the solid radical was dissolved in the 1-octanol. No ultrasonication was used to prevent degradation of the polarizing agents [43]. Table 1 summarizes the utilized polarizing agents and the obtained concentrations.

The solutions were then transferred into 3.2 mm sapphire rotors using an Eppendorf pipet. The rotors were sealed with either silicon or

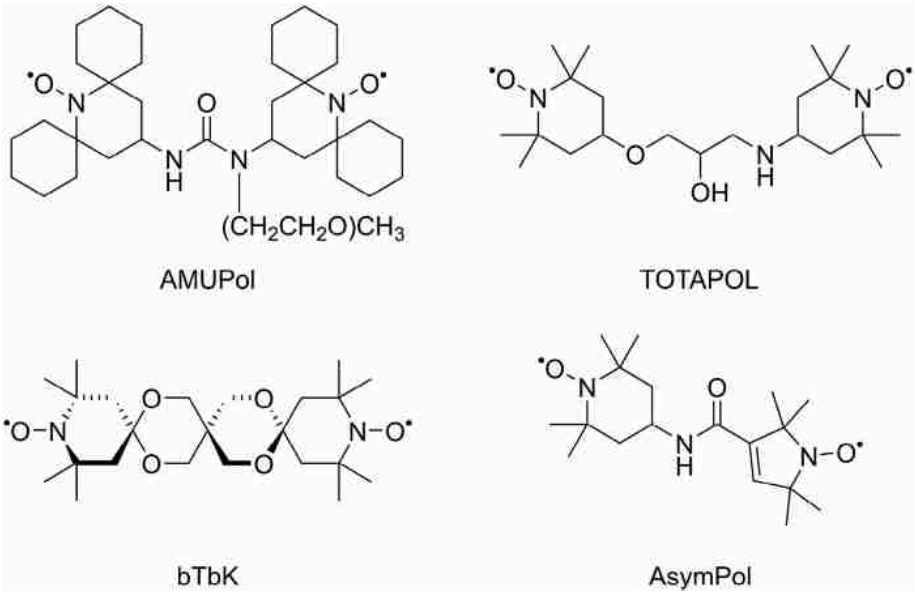

Fig. 1. Structures of the utilized polarizing agents AMUPol [39], TOTAPOL [40], bTbK [41] and AsymPol [42].

Table 1
Polarization agents used in this work, corresponding concentrations and obtained enhancement factors, determined from the $^{1}H \rightarrow ^{13}C$ CP MAS DNP experiments.

Polarizing agent	AMUPol	TOTAPOL	bTbK	AsymPol
Concentration/mM	15, 40	15	7.5*	15
Average ^{13}C enhancement	5.8, 7.5	2.4	4.11	6.4

*estimated concentration of the saturated solution.

homemade rubber plugs and closed with ZrO_2 driving caps.

2.3. DNP enhanced ^{13}C solid state NMR spectroscopy

All ssNMR measurements were carried out on a Bruker Avance III 400 DNP NMR spectrometer operating at 9.4 T (401.63 MHz for ^{1}H, 100.99 MHz for ^{13}C), using a 9.7 T Bruker gyrotron system to generate microwaves (μW) at 263 GHz frequency. The spectrometer was equipped with a 3.2 mm low temperature H/X/Y triple resonance probe which was used in H/C/Y triple mode throughout all measurements. Sample temperatures were nominally 112 K and 120 K for data obtained with and without μW irradiation of the sample, respectively. A MAS rate of 8 kHz was used. Heteronuclear decoupling was performed during data acquisition using the SPINAL-64 decoupling sequence [44].

Enhancement factors for ^{13}C were calculated based on $^{1}H \rightarrow ^{13}C$ cross-polarization (CP) MAS experiments. The contact time in these experiments was set to 2 ms; a ramped pulse was applied on the ^{1}H-channel. Each spectrum was recorded with 16 scans. Average nominal values of the enhancement factors were obtained by scaling the peak maxima of the μW-off spectra to those of the μW-on spectra. These values are given in Table 1.

To determine the buildup times T_b, saturation recovery experiments were employed. ^{13}C magnetization was initially quenched by applying a pulse train consisting of 20 π/2-pulses with a respective pulse length of 3.5 μs and a delay of 5 ms between the pulses. Spectral data was acquired after buildups τ_b of 2, 4, 7.5, 16, 32, 75, 128 and 256 s, recording 128 scans for the shortest τ_b and 64 scans for all other τ_b.

To be able to record the direct polarization transfer path only, the pulse sequence introduced by some of us in earlier work was applied [25]. In this sequence, the standard saturation recovery experiment was modified by the addition of a train of rotor-synchronized π-pulses with a pulse length of 6 μs on the ^{1}H channel. The pulses were spaced 50 ms apart for all buildup times shorter than 32 s, and 500 ms apart for buildup times of 32 s and above.

The obtained spectra for the direct polarization pathway and the superposition of direct and indirect pathways were normalized to an equal number of scans and deconvoluted using Origin Pro 2021 using a Lorentzian line shape to for all signals. In this way, the intensities of the C_1- and C_8-signal of the 1-octanol molecule were determined and further examined, as these peaks are of interest for this work. The amount of indirect polarization was determined by subtracting the direct-pathway-only spectra from the ones obtained from the superposition of both pathways. The obtained signal intensities were plotted against the corresponding τ_b used in the experiment to determine T_b times of the carbons of interest.

3. Results and discussion

3.1. $^{1}H \rightarrow ^{13}C$ CP MAS DNP of 1-octanol

First, $^{1}H \rightarrow ^{13}C$ CP MAS DNP experiments were performed to determine whether signal enhancement is feasible for the four investigated radicals in 1-octanol solution and to estimate the enhancement factors. Exemplary $^{1}H \rightarrow ^{13}C$ CP MAS spectra of AMUPol (15 mM) dissolved in 1-octanol recorded with and without μW irradiation are shown in Fig. 2.

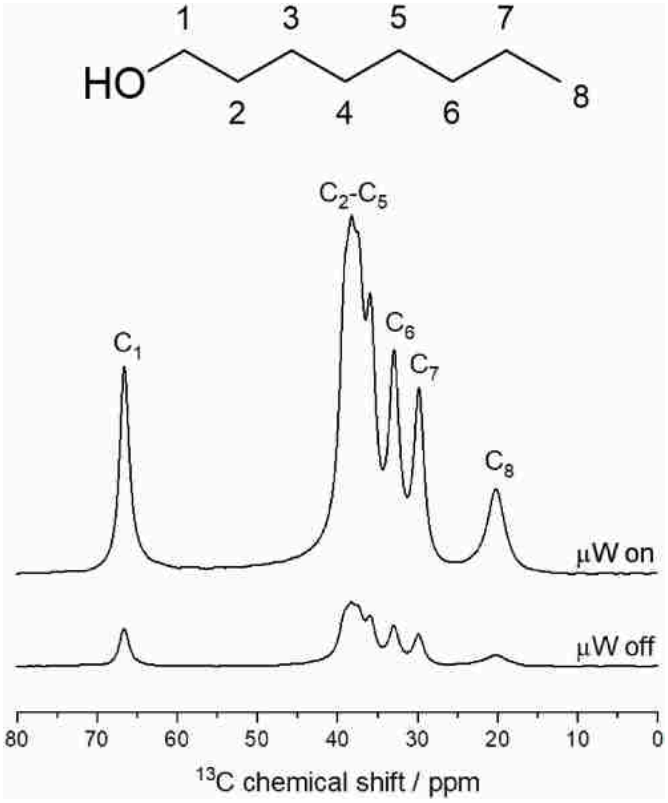

Fig. 2. $^{1}H \rightarrow ^{13}C$ CP MAS spectra recorded with μW on and μW off of AMUPol (15 mM) dissolved in 1-octanol. Also shown is the structure of 1-octanol and the corresponding peak assignments.

In the obtained spectra, the signals are assigned to the 1-octanol carbons according to their chemical surroundings. The signal at 67 ppm is attributed to C_1, which is located closest to the hydroxyl group. The signal at 20 ppm corresponds to the methyl group of the aliphatic moiety of the 1-octanol molecule, C_8 [45]. All other signals between the C_1 and C_8 signals correspond to the methylene groups of the 1-octanol.

For comparison, the signal enhancements obtained for the various

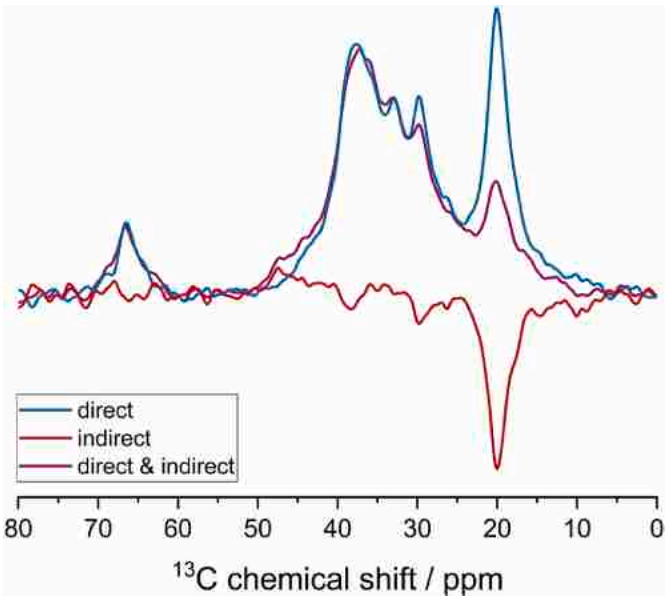

Fig. 3. ^{13}C MAS DNP spectrum of AMUPol dissolved in 1-octanol (15 mM). The direct and the indirect channel as well as their superposition are displayed.

radicals in 1-octanol solution are summarized in Table 1. The largest signal enhancement ($\varepsilon = 7.5$) is observed for AMUPol in 1-octanol (40 mM). Since the signal enhancement usually increases with the radical concentration until the radical concentration is high enough for the paramagnetic quenching of the polarization to prevail [46], this effect is expected. TOTAPOL shows the smallest enhancement factor ($\varepsilon = 2.4$). Due to its aliphatic linker connecting the two nitroxide radical moieties, the TOTAPOL molecule displays a relatively large degree of flexibility [46]. This hinders a more efficient polarization transfer *via* the Cross Effect (CE) [39], the dominant polarization transfer effect for nitroxide biradicals [33]. The more rigid radicals AMUPol, bTbK and AsymPol allow for a more efficient polarization transfer *via* the CE, therefore showing larger enhancement factors. The comparatively small enhancement factors documented in this work (see Table 1) are most probably caused by 1-octanol being a poor glass former, restricting efficient DNP hyperpolarization [47,48].

For all radicals, a largely homogeneous enhancement is observed for all signals. This is explained by the way in which polarization is distributed through the sample in CP experiments. The unpaired electrons of the polarizing agents are polarized by the applied μW radiation. This polarization is transferred to the surrounding nuclei *via* the CE. Subsequently, the thereby created ^{1}H polarization spreads throughout the sample *via* homonuclear ^{1}H–^{1}H spin diffusion [49]. This polarization is then transferred to the ^{13}C nuclei *via* a spinlock pulse [33,50,51].

The efficacy of the homonuclear ^{1}H–^{1}H spin diffusion strongly depends on the proximity of the nuclei to each other, since this process relies on dipole-dipole interactions [49]. Considering the uniform enhancement observed for all signals of 1-octanol, it is assumed that homogeneous ^{1}H–^{1}H spin diffusion takes place in the sample, indicating a statistically uniform distribution of ^{1}H–^{1}H distances in the sample. Contrary cases have been observed for analytes dissolved in either hydrophilic or hydrophobic solvent matrixes [52]. Investigations with an additional analyte and 1-octanol as solvent matrix are beyond the scope of this paper.

In the investigated case, the uniform DNP enhancement renders ^{1}H → ^{13}C CP MAS DNP experiments unsuitable to elucidate the way the radical interacts with the analyte and its position relative to the analyte molecules.

3.2. ^{13}C MAS DNP of 1-octanol – direct vs. indirect polarization transfer

DNP enhanced ^{13}C MAS direct polarization experiments are applied to determine the amount of polarization that is transferred directly to the ^{13}C nuclei *vs.* indirectly through the proton reservoir, allowing for a determination of the spatial proximity of the polarizing agent to certain parts of the analyte. An exemplary ^{13}C MAS DNP spectrum of AMUPol dissolved in 1-octanol (15 mM) is shown in Fig. 3. The direct and the indirect channel as well as the superposition of both are illustrated.

For the methyl group observed at 20 ppm, the indirect polarization transfer pathway is consistently dominant throughout this work. The indirect polarization transfer pathway is aided by molecular motion [25], therefore the indirect polarization transfer for the rotating methyl group is significant [47]. The signal corresponding to C_7 also displays indirect polarization transfer but with less efficiency, showing that this group retains dynamics at low temperatures. All other groups only show negligible indirect polarization transfer pathway. This suggests that the 1-octanol molecules form rather rigid, supramolecular structures when frozen [47].

To allow for an elucidation of the spatial proximity of the polarizing agents to the different chemical groups of the 1-octanol molecule, the ratio of direct *vs.* indirect polarization transfer pathways for the carbon nuclei of interest needs to be determined. Since different samples with varying radical concentrations were investigated in this study, a comparison of the absolute signal intensities obtained by deconvoluting the spectra is not expected to yield reasonable results. Therefore, to ensure comparability between samples, a relative method to evaluate the amount of indirect pathway polarization x_{indirect} is established in this work.

Here, the overall signal intensity is calculated as the sum of the magnitude of signal intensities I_{total} of the direct and indirect pathway signal (I_{direct} and I_{indirect} respectively). Subsequently, I_{indirect} is divided by that sum, according to eq. (1). x_{indirect} therefore represents the percentage of the signal intensity achieved by indirect polarization transfer compared to the total signal intensity.

$$x_{\text{indirect}} = \frac{|I_{\text{indirect}}|}{I_{\text{direct}} + |I_{\text{indirect}}|} = \frac{|I_{\text{indirect}}|}{I_{\text{total}}} \tag{1}$$

Since the value x_{indirect} only depends on the ratio of two signal intensities obtained from the same sample, parameters such as the sample amount or the amount of radical used are removed by the division. Therefore, this approach can be used to compare the dependency of the ratio of the direct *vs.* the indirect polarization pathway for different radicals.

3.3. Analysis of the ratios of direct vs. indirect polarization for different radicals

The analysis of the ratios of direct *vs.* indirect polarization transfer pathways for each radical, buildup time τ_b and carbon of interest is illustrated in Fig. 4. This is done by plotting x_{indirect} as a function of τ_b of the experiment for each radical and for both C_1 and C_8 of the 1-octanol molecule.

Fig. 4a shows x_{indirect} for the methyl carbon of the 1-octanol molecule for the hydrophilic radicals AMUPol and TOTAPOL as a function of τ_b. The polarization builds up very quickly for both radicals, showing that the indirect polarization transfer pathway is highly efficient throughout the entire span of τ_b. Comparing the polarization transfer patterns for different concentrations of AMUPol, an overall slight decrease of the efficiency of indirect polarization transfer is observed with increased concentration. This confirms that the addition of more polarizing agent and therefore the statistic increase of spatial proximity lowers the amount of indirect pathway polarization. This effect is in accordance with what was observed by some of the authors earlier [25]. The AMUPol samples show the most efficient polarization transfer *via* the indirect pathway for the methyl group, illustrating a less efficient polarization transfer *via* the direct pathway in return. This suggests a large distance between the aliphatic moiety of the 1-octanol molecule and the polarizing agent, inhibiting an efficient direct transfer of polarization from the radical to the C_8. It also demonstrates the high amount of dynamics the methyl group retains at low temperatures [27].

In Fig. 4b, the analysis is shown for the methylene carbon neighboring the hydroxyl group of the 1-octanol molecule. For both AMUPol and TOTAPOL, the indirect polarization builds up very quickly, reaching a maximum after 4 s and decaying afterwards as the direct polarization transfer pathway becomes the dominant one. Apparently, the indirect polarization transfer pathway through the proton reservoir proceeds faster than the direct polarization transfer from the radical to the C_1 *via* the CE. This effect is observable despite the suggested closer proximity of the hydrophilic radical to the C_1. In this work, protonated 1-octanol as well as a constant μW-source have been used. The relatively uniform enhancement throughout the 1-octanol molecule observed for the ^{1}H → ^{13}C CP MAS DNP experiments show that hyperpolarization spreads through the proton reservoir evenly. This means that it's highly likely that the proton reservoir surrounding the carbon atoms has been hyperpolarized long before the actual measurements take place. Considering the relatively small concentrations of the utilized polarizing agents, it is statistically more likely for any carbon to be polarized *via* the hyperpolarized proton reservoir. Therefore, the indirect pathway polarization is quicker to hyperpolarize the observed carbon atoms not directly neighboring the polarization agent before dissipating throughout the 1-octanol in the case of longer τ_b.

For both AMUPol concentrations, a much smaller percentage of

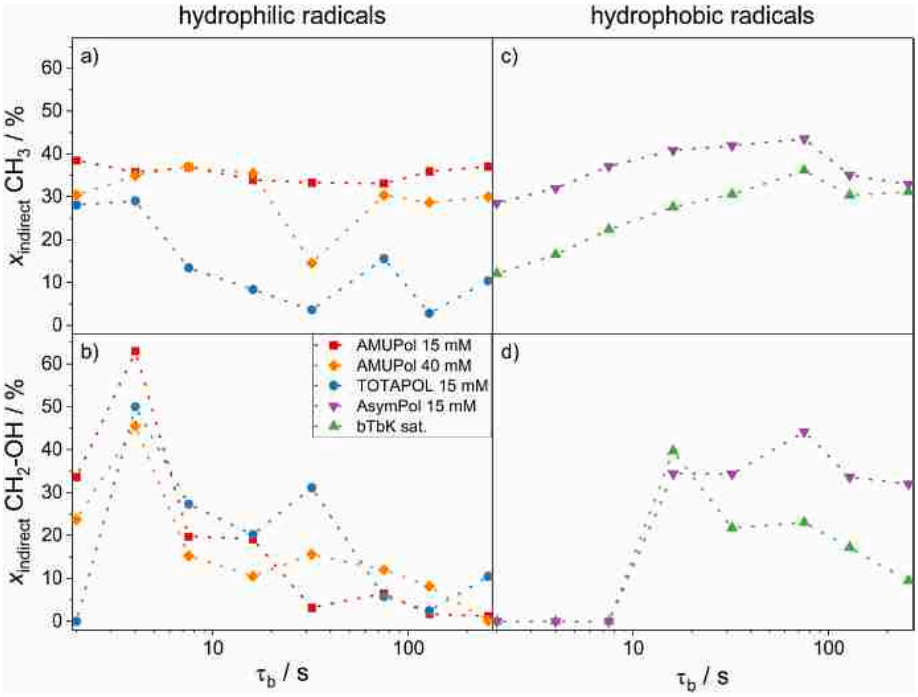

Fig. 4. Ratios of indirect polarization compared to the total signal intensity for the methyl group (panel a and c) and the methylene group neighboring the hydroxyl group of the 1-octanol molecule (panel b and d) as a function of τ_b. The hydrophilic and hydrophobic radicals are displayed separately to facilitate interpretation.

indirect polarization transfer is observed at long τ_b compared to the methyl carbon, pointing to a close spatial proximity of the AMUPol radical to the C_1. Considering that AMUPol is a highly hydrophilic polarizing agent [39], it is to be expected to be found close to the hydroxyl group of the 1-octanol molecule, which explains the presented findings. Additionally, the methylene group is less mobile than the methyl group at the present temperatures [53], generally lowering its affinity towards the indirect polarization transfer pathway.

TOTAPOL shows a generally low affinity for the indirect polarization pathway for both investigated carbons (Fig. 4a and b). TOTAPOL is the most flexible of the investigated polarizing agents (see Fig. 1 for structures of utilized polarizing agents) [40,41,46], which would usually lead to the analyte molecules not being able to approach the radical as closely as possible for more rigid radicals. This would lead to an increase of the observed indirect channel polarization transfer [31]. A possible reason for this behavior might be due to the inherent dynamics of the polarizing agent disturbing the local supramolecular structure formed by the 1-octanol molecules, preventing the analyte molecule from forming the usually observed micelles or ribbons [54–56]. Hence, a more glass-like phase of 1-octanol might form around the TOTAPOL molecules, facilitating the direct polarization transfer and leading to the polarizing agent being distributed more evenly in the relevant part of the solution.

Fig. 4c shows the ratios of the indirect polarization pathway for the methyl group and the hydrophobic radicals, AsymPol and bTbK. Both polarizing agents show comparable ratios of the direct vs. the indirect polarization transfer pathway and a slow increase of the amount of the indirect pathway polarization until a maximum is reached and the indirect polarization transfer pathway becomes less pronounced for long buildup times ($\tau_b \geq 128$ s). bTbK shows less indirect polarization transfer than AsymPol initially. This finding suggests a proximity of the bTbK molecules to the C_8, aiding a direct polarization transfer, which is in agreement to bTbK being the most hydrophobic and therefore most lipophilic polarizing agent investigated in this work [41].

The methylene group neighboring the hydroxyl group generally shows a slow buildup when the hydrophobic radicals are utilized (Fig. 4d). This points to an ineffective polarization transfer to the C_1 and therefore a large distance between the radicals and the methylene group.

It is assumed that the methylene group takes part in the formation of supramolecular structures and therefore is generally less accessible for surrounding molecules [53,57], therefore impeding polarization transfer of any kind. When a hydrophilic polarizing agent is employed, it is probably able to insert itself somewhere close to the C_1 in this supramolecular structure, aiding the polarization transfer. In contrast to that, the investigated hydrophobic polarizing agents are not able to disturb the formation of supramolecular structures at the hydrophilic moiety of the 1-octanol molecule.

After a buildup time of 16 s, the first signal of the C_1 can be observed, which then displays a large amount of indirect polarization transfer. Interestingly, the amount of indirect polarization transfer reduces for bTbK with longer τ_b, again suggesting that the direct polarization transfer pathway becomes more dominant the longer the experimental τ_b is. As the buildup of the indirect polarization seems to be quicker than the one of the direct polarization, it is possible that the decay is caused by the indirect polarization reaching the C_1 and potentially dissipating throughout the 1-octanol molecule before the actual spectrum is measured.

Interestingly, AsymPol does not show the same decay of the indirect polarization as it remains at a relatively constant level after the initial buildup. As AsymPol was computationally devised to have a large electron dipolar coupling between its two radical moieties, its defining feature is a very short polarization buildup time [42]. This short buildup time might lead to a constant repolarization of the proton reservoir, which then repolarizes the investigated C_1 throughout the applied τ_b, therefore leading to a constant amount of indirect polarization reaching the C_1.

3.4. *Investigation of C_1 and C_8 buildup times*

To confirm the findings of the previous analysis, the direct buildup times of the investigated carbons were determined under the influence of the different radicals. Direct polarization transfer can only proceed when the observed carbon is in the vicinity of the radical since natural abundance homonuclear ^{13}C spin diffusion is inefficient [25]. Hence, the length of the direct T_b time of a certain carbon atom in the 1-octanol

molecule can be used to estimate its proximity to the polarizing agents.

Fig. 5 shows the determined direct T_b times for both the methylene carbon C_1 and the methyl carbon C_8. The corresponding buildup curves can be found in Fig. S1 in the Supporting Informations.

The methyl group shows a much quicker buildup than the methylene group for all utilized polarizing agents, a phenomenon which is well-documented and understood to be due to the rotor motions of methyl end groups that remain active even at very low temperatures [14,19,27,31].

AMUPol in 1-octanol (15 mM), the most hydrophilic radical used in this work [39], shows the longest T_b time at the C_8 and the shortest T_b time at the C_1, indicating a spatial proximity of the AMUPol to the hydrophilic end of the molecule. Increasing the concentration of the AMUPol to 40 mM and therefore increasing the average proximity of the polarizing agent to the 1-octanol leads to a slight decrease of the T_b times for the methylene carbon. Since an increased concentration of the radical aids in the polarization transfer, this observation is expected [33]. However, an increased concentration of AMUPol does not lead to a significant decrease of the T_b time for the methyl carbon. It is therefore assumed that the AMUPol molecules strongly favor an orientation towards the hydroxyl group of the 1-octanol, despite the heightened concentration.

BTbK and AsymPol, the hydrophobic polarizing agents investigated in this study [41,42], show significantly shorter T_b times for the C_8 compared to the much longer T_b times for the C_1, demonstrating that the radicals are preferably located towards the aliphatic moiety of the 1-octanol molecule.

TOTAPOL, which is expected to behave similarly to AMUPol since it also falls in the range of hydrophilic polarizing agents, shows T_b times which lie closer to those of the hydrophobic radicals. Due to its dynamics within the linker connecting the two radical moieties and therefore less efficient overall polarization transfer [41], longer T_b times were expected for TOTAPOL at all positions of the 1-octanol molecule. For C_1, this expectation has been confirmed as a long T_b time is observed for this carbon despite the assumption that the hydrophilic TOTAPOL might have an affinity for the position close to the hydrophilic moiety of the 1-octanol. However, for C_8, a shorter T_b time is observed compared to the other hydrophilic radicals. Considering that the observed T_b times for TOTAPOL are not matching the ones observed for AMUPol, a rigid hydrophilic biradical, the hypothesis of TOTAPOL's dynamic disturbing the local structure of the analyte 1-octanol and therefore leading to a more glass-like 1-octanol phase with statistically distributed TOTAPOL molecules might explain the unexpected behavior of the T_b times observed for TOTAPOL.

4. Conclusion

DNP enhanced ssNMR of different radicals dissolved in the amphiphilic 1-octanol was utilized to illustrate the influence of the choice of polarizing agent and its properties on the observed polarization transfer pathways. The polarizing agents AMUPol, bTbK, AsymPol and TOTAPOL were investigated in this work. To achieve comparable results across all samples, independent of radical concentration and amount of sample used, a relative method was established to quantify the proportion of indirectly transferred polarization expressed as a percentage of the total signal intensity. Using this method, it could be shown that the hydrophilicity of the polarizing agents plays a key role in which part of the 1-octanol molecule is polarized *via* which polarization pathway. AMUPol, a hydrophilic polarizing agent, preferably polarizes the hydrophilic moiety of the 1-octanol directly, while bTbk, a hydrophobic polarizing agent, shows a stronger affinity towards directly polarizing the aliphatic part of the 1-octanol. Interestingly, TOTAPOL does not seem to favor the indirect polarization pathway for either of the investigated carbons. This observation is explained with the relatively low rigidity of the TOTAPOL-molecule which allows a high degree of dynamics, therefore disturbing the otherwise rigid supramolecular

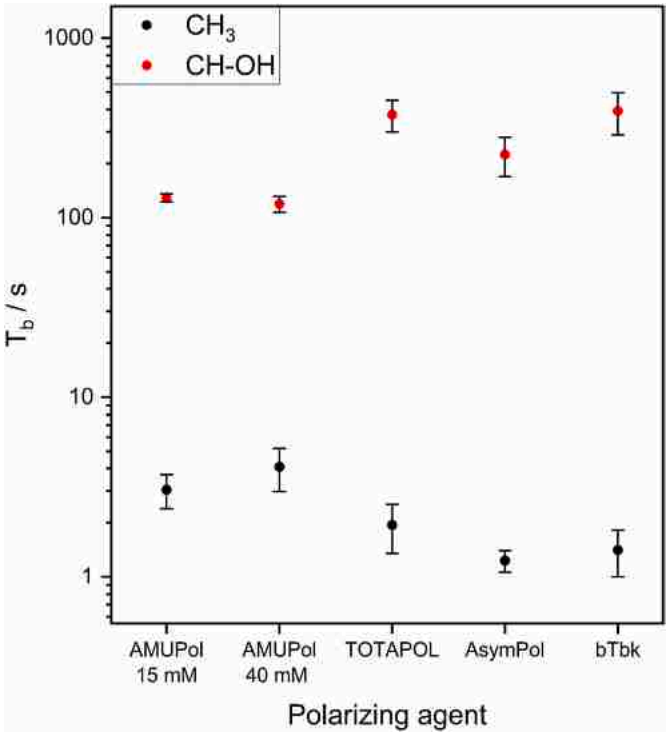

Fig. 5. Determined direct T_b values for the methyl carbon C_8 and the relevant methylene carbon C_1.

organization of the amphiphilic 1-octanol molecules and facilitating the direct polarization transfer in a glass-like 1-octanol phase around the TOTAPOL molecules.

To confirm these findings, T_b times of the carbons of interests were determined *via* the recorded saturation recovery experiments. For the hydrophobic polarizing agents and the methyl carbon of the 1-octanol molecule, short T_b times were observed, indicating a very quick buildup of polarization, suggesting a close proximity of these carbon atoms to the radical. For the methylene group neighboring the hydroxyl group, long T_b times are observed for the hydrophobic polarizing agents. The hydrophilic polarizing agents are shown to lead to shorter T_b times for the methylene group of interest, lowering the time constant by their affinity to the hydroxyl group. For the methyl carbon, longer T_b times are observed compared to the lipophilic polarization agents. Again, TOTAPOL does not follow any trend that might be assumed from its hydrophilic nature, constituting an exception to the trends observed in this study.

The findings presented in this work lay the foundation of enabling informed radical choices for specific samples. Especially in biological samples like cellular components, which consist of large molecules or molecules that are part of supramolecular structures, the presented findings enable researchers to make informed choices of polarizing agent targeting optimum polarization of the nuclei of interest.

Declaration of competing interest

The authors declare that they have no known competing financial interests or personal relationships that could have appeared to influence the work reported in this paper.

Data availability

Data is available in the supplementary information.

Acknowledgements

Financial support by the Deutsche Forschungsgemeinschaft under Contract Bu-911-24-2 and by the National Science Foundation under Grant No. 1953428 are gratefully acknowledged. The authors would also like to thank Prof. Senker and coworkers from Bayreuth University and Dr. Ouari and coworkers from Aix-Marseille University for gifting us the utilized AsymPol and bTbK, respectively.

Appendix A. Supplementary data

Supplementary data to this article can be found online at https://doi.org/10.1016/j.ssnmr.2022.101829.

References

[1] R. Henriques, C. Griffiths, E. Hesper Rego, M.M. Mhlanga, PALM and STORM: unlocking live-cell super-resolution, Biopolymers 95 (2011) 322–331, https://doi.org/10.1002/bip.21586.
[2] L. Stryer, Fluorescence energy transfer as a spectroscopic ruler, Annu. Rev. Biochem. 47 (1978) 819–846, https://doi.org/10.1146/annurev.bi.47.070178.004131.
[3] P. Trigo-Mourino, T. Thestrup, O. Griesbeck, C. Griesinger, S. Becker, Dynamic tuning of FRET in a green fluorescent protein biosensor, Sci. Adv. 5 (2019), eaaw4988, https://doi.org/10.1126/sciadv.aaw4988.
[4] Y. Wang, W. Dai, Z. Liu, J. Liu, J. Cheng, Y. Li, X. Li, J. Hu, J. Lü, Single-cell infrared microspectroscopy quantifies dynamic heterogeneity of mesenchymal stem cells during adipogenic differentiation, Anal. Chem. 93 (2021) 671–676, https://doi.org/10.1021/acs.analchem.0c04110.
[5] R. Smith, K.L. Wright, L. Ashton, Raman spectroscopy: an evolving technique for live cell studies, Analyst 141 (2016) 3590–3600, https://doi.org/10.1039/C6AN00152A.
[6] D.I. Freedberg, P. Selenko, Live cell NMR, Annu. Rev. Biophys. 43 (2014) 171–192, https://doi.org/10.1146/annurev-biophys-051013-023136.
[7] T. Ikeya, P. Güntert, Y. Ito, Protein structure determination in living cells, Int. J. Mol. Sci. 20 (2019), https://doi.org/10.3390/ijms20102442.
[8] S. Meier, M. Karlsson, P.R. Jensen, M.H. Lerche, J.Ø. Duus, Metabolic pathway visualization in living yeast by DNP-NMR, Mol. Biosyst. 7 (2011) 2834–2836, https://doi.org/10.1039/c1mb05202k.
[9] H. Takahashi, I. Ayala, M. Bardet, G. de Paëpe, J.-P. Simorre, S. Hediger, Solid-state NMR on bacterial cells: selective cell wall signal enhancement and resolution improvement using dynamic nuclear polarization, J. Am. Chem. Soc. 135 (2013) 5105–5110, https://doi.org/10.1021/ja312501d.
[10] J.-H. Ardenkjaer-Larsen, G.S. Boebinger, A. Comment, S. Duckett, A.S. Edison, F. Engelke, C. Griesinger, R.G. Griffin, C. Hilty, H. Maeda, G. Parigi, T. Prisner, E. Ravera, J. van Bentum, S. Vega, A. Webb, C. Luchinat, H. Schwalbe, L. Frydman, Facing and overcoming sensitivity challenges in biomolecular NMR spectroscopy, Angew. Chem. Int. Ed. 54 (2015) 9162–9185, https://doi.org/10.1002/anie.201410653.
[11] A. Pardi, Isotope labelling for NMR studies of biomolecules, Curr. Opin. Struct. Biol. 2 (1992) 832–835, https://doi.org/10.1016/0959-440X(92)90107-I.
[12] M.H. Lerche, P.R. Jensen, M. Karlsson, S. Meier, NMR insights into the inner workings of living cells, Anal. Chem. 87 (2015) 119–132, https://doi.org/10.1021/ac501467x.
[13] Ü. Akbey, H. Oschkinat, Structural biology applications of solid state MAS DNP NMR, J. Magnet. Resonance (San Diego, Calif) 269 (2016) (1997) 213–224, https://doi.org/10.1016/j.jmr.2016.04.003.
[14] T. Biedenbänder, V. Aladin, S. Saeidpour, B. Corzilius, Dynamic nuclear polarization for sensitivity enhancement in biomolecular solid-state NMR, Chem. Rev. 122 (2022) 9738–9794, https://doi.org/10.1021/acs.chemrev.1c00776.
[15] J.H. Ardenkjaer-Larsen, B. Fridlund, A. Gram, G. Hansson, L. Hansson, M. H. Lerche, R. Servin, M. Thaning, K. Golman, Increase in signal-to-noise ratio of 10,000 times in liquid-state NMR, Proc. Natl. Acad. Sci. U.S.A. 100 (2003) 10158–10163, https://doi.org/10.1073/pnas.1733835100.
[16] A.Y. Fadeev, T.J. McCarthy, Trialkylsilane monolayers covalently attached to silicon surfaces: wettability studies indicating that molecular topography contributes to contact angle hysteresis, Langmuir 15 (1999) 3759–3766, https://doi.org/10.1021/la981486o.
[17] M. Hong, W.F. DeGrado, Structural basis for proton conduction and inhibition by the influenza M2 protein, Protein Sci. 21 (2012) 1620–1633, https://doi.org/10.1002/pro.2158.
[18] V.S. Mandala, J.K. Williams, M. Hong, Structure and dynamics of membrane proteins from solid-state NMR, Annu. Rev. Biophys. 47 (2018) 201–222, https://doi.org/10.1146/annurev-biophys-070816-033712.
[19] J. Mao, V. Aladin, X. Jin, A.J. Leeder, L.J. Brown, R.C.D. Brown, X. He, B. Corzilius, C. Glaubitz, Exploring protein structures by DNP-enhanced methyl solid-state NMR spectroscopy, J. Am. Chem. Soc. 141 (2019) 19888–19901, https://doi.org/10.1021/jacs.9b11195.
[20] E. Nimerovsky, K.T. Movellan, X.C. Zhang, M.C. Forster, E. Najbauer, K. Xue, R. Dervişoğlu, K. Giller, C. Griesinger, S. Becker, L.B. Andreas, Proton detected solid-state NMR of membrane proteins at 28 tesla (1.2 GHz) and 100 kHz magic-angle spinning, Biomolecules 11 (2021), https://doi.org/10.3390/biom11050752.
[21] A.K. Schütz, Solid-state NMR approaches to investigate large enzymes in complex with substrates and inhibitors, Biochem. Soc. Trans. 49 (2021) 131–144, https://doi.org/10.1042/BST20200099.
[22] M. Weingarth, M. Baldus, Solid-state NMR-based approaches for supramolecular structure elucidation, Acc. Chem. Res. 46 (2013) 2037–2046, https://doi.org/10.1021/ar300316e.
[23] S. Yan, C.L. Suiter, G. Hou, H. Zhang, T. Polenova, Probing structure and dynamics of protein assemblies by magic angle spinning NMR spectroscopy, Acc. Chem. Res. 46 (2013) 2047–2058, https://doi.org/10.1021/ar300309s.
[24] D. Daube, V. Aladin, J. Heiliger, J.J. Wittmann, D. Barthelmes, C. Bengs, H. Schwalbe, B. Corzilius, Heteronuclear cross-relaxation under solid-state dynamic nuclear polarization, J. Am. Chem. Soc. 138 (2016) 16572–16575, https://doi.org/10.1021/jacs.6b08683.
[25] M.M. Hoffmann, S. Bothe, T. Gutmann, F.-F. Hartmann, M. Reggelin, G. Buntkowsky, Directly vs indirectly enhanced 13 C in dynamic nuclear polarization magic angle spinning NMR experiments of nonionic surfactant systems, J. Phys. Chem. C 121 (2017) 2418–2427, https://doi.org/10.1021/acs.jpcc.6b13087.
[26] A.W. Overhauser, Polarization of nuclei in metals, Phys. Rev. 92 (1953) 411–415, https://doi.org/10.1103/PhysRev.92.411.
[27] V. Aladin, B. Corzilius, Methyl dynamics in amino acids modulate heteronuclear cross relaxation in the solid state under MAS DNP, Solid State Nucl. Magn. Reson. 99 (2019) 27–35, https://doi.org/10.1016/j.ssnmr.2019.02.004.
[28] V. Aladin, M. Vogel, R. Binder, I. Burghardt, B. Suess, B. Corzilius, Complex formation of the tetracycline-binding aptamer investigated by specific cross-relaxation under DNP, Angew. Chem. Int. Ed. 58 (2019) 4863–4868, https://doi.org/10.1002/anie.201811941.
[29] Q.Z. Ni, E. Markhasin, T.V. Can, B. Corzilius, K.O. Tan, A.B. Barnes, E. Daviso, Y. Su, J. Herzfeld, R.G. Griffin, Peptide and protein dynamics and low-temperature/DNP magic angle spinning NMR, J. Phys. Chem. B 121 (2017) 4997–5006, https://doi.org/10.1021/acs.jpcb.7b02066.
[30] H. Park, B. Uluca-Yazgi, S. Heumann, R. Schlögl, J. Granwehr, H. Heise, P.P. M. Schleker, Heteronuclear cross-relaxation effect modulated by the dynamics of N-functional groups in the solid state under 15N DP-MAS DNP, J. Magn. Reson. 312 (2020), 106688, https://doi.org/10.1016/j.jmr.2020.106688.
[31] M.M. Hoffmann, S. Bothe, T. Gutmann, G. Buntkowsky, Unusual local molecular motions in the solid state detected by dynamic nuclear polarization enhanced NMR spectroscopy, J. Phys. Chem. C 121 (2017) 22948–22957, https://doi.org/10.1021/acs.jpcc.7b07965.
[32] M.M. Hoffmann, S. Bothe, M. Brodrecht, V. Klimavicius, N.B. Haro-Mares, T. Gutmann, G. Buntkowsky, Direct and indirect dynamic nuclear polarization transfer observed in mesoporous materials impregnated with nonionic surfactant solutions of polar polarizing agents, J. Phys. Chem. C 124 (2020) 5145–5156, https://doi.org/10.1021/acs.jpcc.9b10504.
[33] A.S. Lilly Thankamony, J.J. Wittmann, M. Kaushik, B. Corzilius, Dynamic nuclear polarization for sensitivity enhancement in modern solid-state NMR, Prog. Nucl. Magn. Reson. Spectrosc. 102–103 (2017) 120–195, https://doi.org/10.1016/j.pnmrs.2017.06.002.
[34] J. Heiliger, T. Matzel, E.C. Çetiner, H. Schwalbe, G. Kuenze, B. Corzilius, Site-specific dynamic nuclear polarization in a Gd(III)-labeled protein, Phys. Chem. Chem. Phys. 22 (2020) 25455–25466, https://doi.org/10.1039/d0cp05021k.
[35] M. Juramy, R. Chèvre, P. Cerreia Vioglio, F. Ziarelli, E. Besson, S. Gastaldi, S. Viel, P. Thureau, K.D.M. Harris, G. Mollica, Monitoring crystallization processes in confined porous materials by dynamic nuclear polarization solid-state nuclear magnetic resonance, J. Am. Chem. Soc. 143 (2021) 6095–6103, https://doi.org/10.1021/jacs.0c12982.
[36] S.Y. Liao, M. Lee, T. Wang, I.V. Sergeyev, M. Hong, Efficient DNP NMR of membrane proteins: sample preparation protocols, sensitivity, and radical location, J. Biomol. NMR 64 (2016) 223–237, https://doi.org/10.1007/s10858-016-0023-3.
[37] C.A.F. de Oliveira, C.R.W. Guimares, R.B. de Alencastro, Molecular dynamics study on liquid 1-octanol, Int. J. Quant. Chem. 80 (2000) 999–1006, https://doi.org/10.1002/1097-461X(2000)80:4/5<999:AID-QUA48>3.0.CO;2-K.
[38] P. Sassi, M. Paolantoni, R.S. Cataliotti, F. Palombo, A. Morresi, Water/alcohol mixtures: a spectroscopic study of the water-saturated 1-octanol solution, J. Phys. Chem. B 108 (2004) 19557–19565, https://doi.org/10.1021/jp046647d.
[39] C. Sauvée, M. Rosay, G. Casano, F. Aussenac, R.T. Weber, O. Ouari, P. Tordo, Highly efficient, water-soluble polarizing agents for dynamic nuclear polarization at high frequency, Angew. Chem. 52 (2013) 10858–10861, https://doi.org/10.1002/anie.201304657.
[40] C. Song, K.-N. Hu, C.-G. Joo, T.M. Swager, R.G. Griffin, TOTAPOL: a biradical polarizing agent for dynamic nuclear polarization experiments in aqueous media, J. Am. Chem. Soc. 128 (2006) 11385–11390, https://doi.org/10.1021/ja061284b.
[41] Y. Matsuki, T. Maly, O. Ouari, H. Karoui, F. Le Moigne, E. Rizzato, S. Lyubenova, J. Herzfeld, T. Prisner, P. Tordo, R.G. Griffin, Dynamic nuclear polarization with a rigid biradical, Angew. Chem. 48 (2009) 4996–5000, https://doi.org/10.1002/anie.200805940.
[42] F. Mentink-Vigier, I. Marin-Montesinos, A.P. Jagtap, T. Halbritter, J. van Tol, S. Hediger, D. Lee, S.T. Sigurdsson, G. de Paëpe, Computationally assisted design of polarizing agents for dynamic nuclear polarization enhanced NMR: the AsymPol family, J. Am. Chem. Soc. 140 (2018) 11013–11019, https://doi.org/10.1021/jacs.8b04911.
[43] L.J. Kirschenbaum, P. Riesz, Sonochemical degradation of cyclic nitroxides in aqueous solution, Ultrason. Sonochem. 19 (2012) 1114–1119, https://doi.org/10.1016/j.ultsonch.2012.01.014.

[44] B.M. Fung, A.K. Khitrin, K. Ermolaev, An improved broadband decoupling sequence for liquid crystals and solids, J. Magn. Reson. 142 (2000) 97–101, https://doi.org/10.1006/jmre.1999.1896.
[45] AIST, Spectral Database for Organic Compounds, vol. 1, Octanol, 1999. https://sdbs.db.aist.go.jp/. (Accessed 17 May 2022).
[46] K.-N. Hu, C. Song, H.-H. Yu, T.M. Swager, R.G. Griffin, High-frequency dynamic nuclear polarization using biradicals: a multifrequency EPR lineshape analysis, J. Chem. Phys. 128 (2008), 52302, https://doi.org/10.1063/1.2816783.
[47] S.C. Döller, M. Brodrecht, N.B. Haro Mares, H. Breitzke, T. Gutmann, M. Hoffmann, G. Buntkowsky, Deuterium NMR studies of the solid–liquid phase transition of octanol- d17 confined in SBA-15, J. Phys. Chem. C 125 (2021) 25155–25164, https://doi.org/10.1021/acs.jpcc.1c05873.
[48] F. Mentink-Vigier, Ü. Akbey, H. Oschkinat, S. Vega, A. Feintuch, Theoretical aspects of magic angle spinning - dynamic nuclear polarization, J. Magn. Reson. 258 (2015) 102–120, https://doi.org/10.1016/j.jmr.2015.07.001.
[49] A.B. Barnes, G. de Paëpe, P.C.A. van der Wel, K.-N. Hu, C.-G. Joo, V.S. Bajaj, M. L. Mak-Jurkauskas, J.R. Sirigiri, J. Herzfeld, R.J. Temkin, R.G. Griffin, High-field dynamic nuclear polarization for solid and solution biological NMR, Appl. Magn. Reson. 34 (2008) 237–263, https://doi.org/10.1007/s00723-008-0129-1.
[50] A. Pines, M.G. Gibby, J.S. Waugh, Proton-enhanced nuclear induction spectroscopy. A method for high resolution NMR of dilute spins in solids, J. Chem. Phys. 56 (1972) 1776–1777, https://doi.org/10.1063/1.1677439.
[51] Y. Hovav, A. Feintuch, S. Vega, Theoretical aspects of Dynamic Nuclear Polarization in the solid state - the cross effect, J. Magn. Reson. 214 (2012) 29–41, https://doi.org/10.1016/j.jmr.2011.09.047.
[52] T. Gutmann, B. Kumari, L. Zhao, H. Breitzke, S. Schöttner, C. Rüttiger, M. Gallei, Dynamic nuclear polarization signal amplification as a sensitive probe for specific functionalization of complex paper substrates, J. Phys. Chem. C 121 (2017) 3896–3903, https://doi.org/10.1021/acs.jpcc.6b11751.
[53] G. Buntkowsky, S. Döller, N. Haro-Mares, T. Gutmann, M. Hoffmann, Solid-state NMR studies of non-ionic surfactants confined in mesoporous silica, Z. Phys. Chem. 236 (2022) 939–960, https://doi.org/10.1515/zpch-2021-3132.
[54] K. Hu, Y. Zhou, J. Shen, Z. Ji, G. Cheng, Microheterogeneous structure of 1-octanol in neat and water-saturated state, J. Phys. Chem. B 111 (2007) 10160–10165, https://doi.org/10.1021/jp072847o.
[55] N.P. Franks, M.H. Abraham, W.R. Lieb, Molecular organization of liquid n-octanol: an X-ray diffraction analysis, J. Pharmacol. Sci. 82 (1993) 466–470, https://doi.org/10.1002/jps.2600820507.
[56] H.A. Shallard-Brown, D.J. Watkin, A.R. Cowley, n-Octanol, Acta Crystallogr. 61 (2005) o213–o214, https://doi.org/10.1107/S1600536804032775.
[57] B. Kumari, M. Brodrecht, H. Breitzke, M. Werner, B. Grünberg, H.-H. Limbach, S. Forg, E.P. Sanjon, B. Drossel, T. Gutmann, G. Buntkowsky, Mixtures of alcohols and water confined in mesoporous silica: a combined solid-state NMR and molecular dynamics simulation study, J. Phys. Chem. C 122 (2018) 19540–19550, https://doi.org/10.1021/acs.jpcc.8b04745.

4.3 Elucidation of PEG and Surfactant Alignment in Mesoporous Silica Materials through Direct and Indirect DNP Enhanced NMR spectroscopy

Direct/indirect DNP enhanced ssNMR spectroscopy is an important tool to elucidate the interactions of guest molecules with their host material.[212] Hence, it was utilized to probe the interactions of two economically relevant, polydisperse surfactants as well as of two different PEGs with two PMS materials. The choice of SBA-15 as well as MCM-41 enabled the investigation of pore size effects on the behavior of the guest molecules. At the same time, care was taken to use a SBA-15 material without commonly present micropores[213] as to ensure adequate comparability between the silica materials.

In the previously presented chapter, a relative method for the analysis of spectra obtained from direct/indirect DNP enhanced NMR spectroscopy was developed. As it has shown to be powerful in allowing the direct and quantitative comparison of data obtained from different samples, it is again employed here to process the information obtained from the measured ^{13}C ssNMR spectra. By illustrating the amount of direct polarization reaching the different carbons in the PEG moieties of each molecule, it could be demonstrated that the amphiphilic surfactants prefer a different arrangement in the pores compared to the hydrophilic PEGs. It could also be shown that pore size appears to have a negligible effect on the arrangement of the guest molecules, potentially due to their small size compared to the pore diameters of the SBA-15 and MCM-41. Additional line width analysis verified the findings of the direct/indirect DNP enhanced NMR spectra.

In previous works concerning surfactant systems, the insights gathered from ssNMR methods were confirmed *via* molecular dynamics (MD) simulations.[108] However, this methodology was not available at the time. Hence, the findings of the one-dimensional direct/indirect DNP enhanced NMR spectroscopy were verified through two-dimensional ^{1}H-^{29}Si FSLG HETCOR spectroscopy.

Based on the comprehensive data collected *via* ssNMR spectroscopy, a model of the arrangement of the surfactant as well as of the PEG molecules in the PMS pores was developed. This shows the extended applicability of ssNMR and especially of direct/indirect DNP enhanced NMR spectroscopy to systems relevant for the green transformation of chemistry towards a more sustainable approach. It also improves the previously difficult quantitative analysis of the signal intensity data obtained from multiple different samples, which was formerly omitted[212] or done through the determination of peak heights.[203] This harbors the potential risk of introducing more error than integrating the signals because signal height is more susceptible to influence through noise. Furthermore, the model of the surfactant arrangement was developed solely using data obtained from one-dimensional NMR spectra, theoretically omitting the need for more sophisticated two-dimensional methods which were merely used for verification purposes.

Reprinted with permission from S. C. Döller, M. Brodrecht, T. Gutmann, M. Hoffmann and G. Buntkowsky, *J. Phys. Chem. C*, **2023**, *127*, 12125–12134. Copyright 2023 American Chemical Society.

THE JOURNAL OF PHYSICAL CHEMISTRY C
A JOURNAL OF THE AMERICAN CHEMICAL SOCIETY

pubs.acs.org/JPCC

Article

Direct and Indirect DNP NMR Uncovers the Interplay of Surfactants with Their Mesoporous Host Material

Sonja C. Döller, Martin Brodrecht, Torsten Gutmann, Markus Hoffmann, and Gerd Buntkowsky*

Cite This: *J. Phys. Chem. C* 2023, 127, 12125−12134

Read Online

ACCESS | Metrics & More | Article Recommendations | Supporting Information

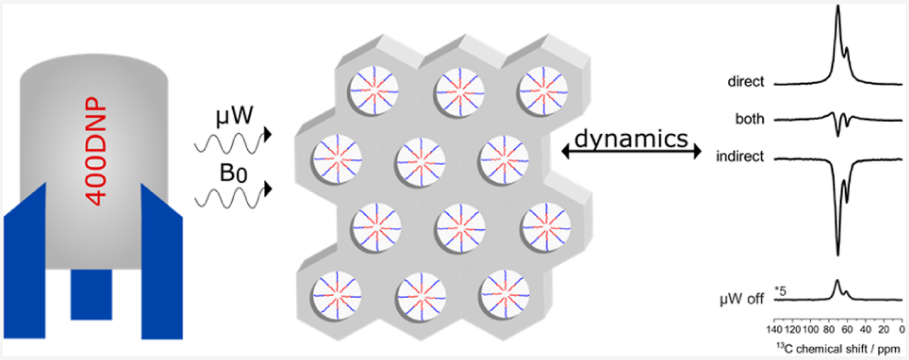

ABSTRACT: Two different mesoporous silica materials (SBA-15 and MCM 41) were impregnated with four different, commercially available surfactants, namely, E_5, PEG 200, $C_{10}E_6$, and Triton X-100. Differential scanning calorimetry was employed to confirm the confinement of the surfactants in the pores of their host materials. Dynamic nuclear polarization enhanced solid state ^{13}C magic angle spinning (MAS) nuclear magnetic resonance (NMR) spectra were recorded for these materials, showing that both the direct as well as the indirect polarization transfer pathways are active for the carbons of the polyethylene glycol moieties of the surfactants. The presence of the indirect polarization pathway implies the presence of molecular motion with correlation times faster than the inverse Larmor frequency of the observed signals. The intensities of the signals were determined, and an approach based on relative intensities was employed to ensure comparability throughout the samples. From these data, the interactions of the surfactants with the pore walls could be determined. Additionally, a model describing the surfactants' arrangement in the pores was developed. It was concluded that all carbons of the hydrophilic surfactants, E_5 and PEG 200, interact with the silica walls in a similar fashion, leading to similar polarization transfer pathway patterns for all observed signals. For the amphiphilic surfactants $C_{10}E_6$ and Triton X-100, the terminal hydroxyl group mediates the majority of the interactions with the pore walls and the polarizing agent.

Downloaded via UNIV DARMSTADT on August 25, 2023 at 08:45:23 (UTC).
See https://pubs.acs.org/sharingguidelines for options on how to legitimately share published articles.

1. INTRODUCTION

High-surface materials are of relevance for a plethora of applications such as chromatography,[1] support materials for precious metal catalysts,[2] adsorbents,[3] drug-delivery systems,[4] and many more.[3] All of these systems rely on the interactions of a liquid phase with a solid interface. In particular, amorphous, mesoporous silica materials are of interest for industrial and academic applications since they are relatively easy to synthesize as well as due to their large surface areas and the facile functionalization of their surfaces to specific tasks.[2,5,6] Hence, silica materials have been found to be the ideal model systems to probe surface interactions and dynamics at a molecular level. Especially the class of Santa Barbara Amorphous[7] (SBA) and M41S phases,[8] such as MCM 41, have been used to study confinement effects on a number of guest molecules.[9−19]

Due to their non-toxicity, surfactants (surface-active agents) as well as polyethylene glycols (PEGs) play a key role in establishing green chemistry principles[20,21] throughout chemical synthesis including catalysis[22] or the production of polymers[23] through the replacement of typical organic solvents.[24] Thanks to their amphiphilic nature, surfactants are able to form supramolecular aggregates. These aggregates are typically in the form of micelles in aqueous solution but may also be of other types such as lamellae, especially at high surfactant concentration or in the bulk of the neat surfactant.[25−27] The presence of such aggregates provides lipophilic spaces in aqueous environments where reactions can take place.[24]

Received: March 23, 2023
Revised: May 31, 2023
Published: June 16, 2023

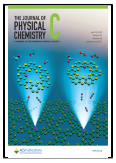

ACS Publications

© 2023 American Chemical Society

Typically, the interplay of a guest molecule with a solid surface strongly alters the guest molecule's properties due to solid−liquid-interactions.[15,28] These interactions are not well understood because they are generally difficult to probe at a molecular level.[29] Solid state nuclear magnetic resonance (ssNMR) has been established as an important tool to investigate surface chemistry and structural details, both of which further the understanding of host−guest interactions and dynamics. By utilizing ^{2}H NMR,[28,30,31] T_1 measurements,[32,33] or NMR diffusometry,[34] the dynamics of systems can be uncovered in ssNMR. To overcome sensitivity issues inherent to ssNMR, dynamic nuclear polarization (DNP) is usually employed, enhancing signals by several orders of magnitude.[35−37] Recently, new methods enabling the investigation of molecular motion have been discovered by the observation of two competing polarization transfer pathways in solid state DNP NMR.[38−45] In the direct pathway, the polarization proceeds from the utilized polarizing agent, usually a radical or a metal ion,[46] directly to the investigated nucleus. The indirect polarization transfer pathway is facilitated by ^{1}H−X (X = ^{13}C, ^{15}N) cross-relaxation of molecular groups due to the presence of adequate dynamics for which the nuclear Overhauser effect type of mechanism is operative.[38,40] The two pathways show opposite signs in the recorded NMR signal, leading to a superposition of two sets of resonances. This distinction allows for site-specific probing in crowded spectra like those obtained from protein samples[42,47] or RNA,[48] the investigation of protein−ligand binding,[43] or the determination of active dynamics under low-temperature DNP conditions.[41,49]

In previous works,[50] it has been shown that DNP-enhanced ssNMR is a suitable method to probe the interactions of guest molecules with a mesoporous host materials, allowing the development of models and the description of dynamic processes inside of the pores. Therefore, the aim of this work is to apply this methodology in an attempt to understand how different classes of surfactants interact with a host material with a hydrophilic surface, namely mesoporous silica, for the purpose of developing a model of their arrangement in the pores. Additionally, the influence of pore size on the confinement is investigated to conclude whether it has a significant effect on the self-assembly of the surfactants.

In this work, the four different analyte molecules shown in Figure 1, pentaethylene glycol (E_5), PEG 200, as well as the surfactants decylhexaglycol ($C_{10}E_6$) and Triton X-100 (Triton), are confined in the pores of two mesoporous silica materials with different pore sizes, namely SBA-15 and MCM 41. For simplification, all analyte molecules are further referred to as surfactants. PEG 200, $C_{10}E_6$, and Triton are produced at an industrial scale and are used as polydisperse mixtures.[40] ^{1}H → ^{13}C CP MAS ssNMR spectra are recorded to estimate an enhancement factor for each sample, employing the hydrophilic binitroxyl radical AMUPol as polarization agent.[51] To analyze the interactions of the surfactants with the walls of the mesopores, ^{13}C MAS DNP-enhanced ssNMR measurements are performed at different buildup times. The contribution of the direct and indirect polarization transfer pathways is analyzed for the carbons located in the PEG moiety of each surfactant. To achieve comparability for all investigated samples, an approach based on relative intensities is employed.[49] Finally, differential scanning calorimetry (DSC) is employed to probe the phase behavior of the different surfactants while confined in the mesoporous silica materials, which is compared to those of the AMUPol dissolved in the bulk surfactants.

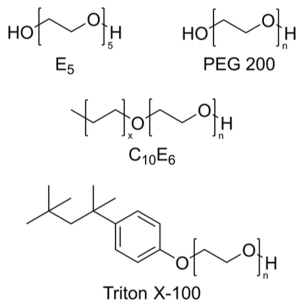

Figure 1. Structures of the surfactants studied in this work. Except for E_5, the surfactants are polydisperse mixtures, and their exact compositions can be found in a prior report[40] and are collected in the Supporting Information in Table S1.

2. MATERIALS AND METHODS

2.1. General. All chemicals were used as received. E_5 was purchased from Alfa Aesar. AMUPol was purchased from CortecNet.[51] The utilized polydisperse surfactants PEG 200, $C_{10}E_6$, and Triton were generously donated by Rochester Midland Corporation. Further details on the mixture composition of the polydisperse surfactants were published in a prior report[40] and are collected in the Supporting Information in Table S1. The chemicals used for the synthesis of the mesoporous silica materials were purchased from Acros, Sigma-Aldrich, Carl Roth, and ABCR. All chemicals were used without further purification unless explicitly mentioned. Details on all chemicals (including the surfactants) used in this work are shown in Table S2 in the Supporting Information.

2.2. Synthesis of the Mesoporous Silica Materials. *2.2.1. Synthesis of SBA-15.* Mesoporous SBA-15 was synthesized according to the literature.[52,53] 21.3 g (0.017 equiv) of Pluronic123 was dissolved in 574.0 mL (165.0 equiv) of demineralized water overnight. To this solution, 108.0 mL (6.0 equiv) of 37 wt % hydrochloric acid was added to yield a concentration of HCl of 1.9 mol L^{-1}. The solution was heated to 40 °C and allowed to equilibrate overnight. Afterward, 47.9 g (1.0 equiv) of tetraethyl orthosilicate (TEOS) was slowly added while stirring. Stirring was continued for 1 h, resulting in a white precipitate. This suspension was stirred at 40 °C for 24 h and was then transferred into a polytetrafluoroethylene (PTFE) bottle. The bottle was stored under static conditions at 90 °C for 48 h. The obtained white precipitate was washed with demineralized water twice and with ethanol once by centrifugation. The leftover template was removed by calcination at 650 °C, yielding 11.70 g of SBA-15 mesoporous silica.

2.2.2. Synthesis of MCM 41. MCM-41 (C_{18}) was synthesized by an optimized protocol based on a protocol reported previously.[34] For this, 14.2 g (36.3 mmol, 0.13 equiv) trimethyloctadecylammonium bromide (C_{18}TAB/stearyltrimethylammonium bromide) was dissolved in 672 mL demineralized water. The mixture was heated to 35 °C. After that, 58.5 mL ammonia solution (25 wt %) was added and the solution was stirred for another 1.5 h until everything was fully dissolved. Afterward, 60.0 g (269 mmol, 1.00 equiv) TEOS was slowly added. After the addition was complete, the suspension was stirred for 1 h. This suspension was then

https://doi.org/10.1021/acs.jpcc.3c01946
J. Phys. Chem. C 2023, 127, 12125−12134

transferred into a PTFE bottle and aged under static conditions at 80 °C for 72 h. After ageing, the white precipitate was filtered off. The porous silica was washed with demineralized water and the leftover template was removed by calcination at 650 °C.

2.3. Characterization of the Mesoporous Silica Materials. *2.3.1. Sample Preparation.* The wet samples were transferred into a glass burette and predried at mild vacuum (approximately 10 mbar) over night. After predrying, the samples were dried using a turbomolecular pump (10^{-6} mbar) over night. During all drying steps, the samples were heated to 80 °C. The dried samples were directly transferred to the Brunauer–Emmett–Teller (BET) analyzer. The masses of the dried samples were used for the evaluation of the adsorption/desorption measurements.

2.3.2. Adsorption–Desorption Measurements. The porosity, pore volume, and specific surface area of the materials were characterized by nitrogen adsorption at 77 K, employing a Thermo Fisher Scientific Surfer BET analyzer using N_2 gas as adsorbent. The specific surface was obtained by the BET method[54] analyzing the curve in the p/p^0 range between 0.1 and 0.4. The pore volume was obtained by the Gurvich method,[55] the p/p^0 value at 0.95 was used. Blank measurements were performed using He gas. Pore size distributions were obtained by applying the Barrett–Joyner–Halenda method,[56] analyzing the adsorption–desorption isotherms in the p/p^0 range between 0.3 and 0.95. Pore sizes obtained by nonlocal density functional theory[57] (NLDFT) used a model for N_2 adsorption on silicon at 77 K. The model for the adsorption of nitrogen on silica surfaces with cylindrical pore geometries of the Advanced Data Processing (ADP) software (V 6.2.4) was used for evaluation. Interpretation of the results follow our previous reports.[34,58]

2.4. Sample Preparation for DNP NMR and DSC Experiments. 2 mg (2.75 μmol) of AMUPol was dissolved into 0.183 mL of the surfactants in small plastic vials to obtain a concentration of ca. 15 mmol L^{-1}. It was necessary to employ ultrasonication for up to 20 min to achieve complete dissolution. As it has been shown that ultrasonication might lead to degradation of the polarizing agents,[59] the effective AMUPol concentrations may have been lower than the nominal concentration of 15 mmol L^{-1}.

In preparation for the impregnation with the surfactants, the utilized mesoporous silica materials SBA-15 and MCM 41 were dried utilizing a turbomolecular pump at room temperature for at least 24 h. The dried silica was then transferred into a glovebox to prevent unwanted adsorption of atmospheric water.

The surfactant solutions were then transferred into aliquots of the respective silicas to fill approximately 80% of the pore volume obtained from the adsorption–desorption measurements, and the materials were left in the glovebox overnight to allow for full absorption of the surfactant solutions. Afterward, the samples were transferred into a freezer in the glovebox to prevent any further degradation of the radicals.

2.5. DSC Measurements. For the measurements of the surfactants confined in the silica materials, approximately 3 mg of the respective sample was transferred into a 5 mm aluminum crucible, which was sealed with an appropriate press by Netzsch. For the pure surfactant solutions, approximately 20 μL of the sample was used for the DSC measurements.

All DSC measurements were performed on the DSC 214 Polyma apparatus by Netzsch in dynamic mode. Liquid nitrogen was employed as cooling agent. An empty cubicle served as reference. A heating/cooling rate of 10 K min^{-1} was used in the temperature range between 100 and 300 K.

The results and discussion of the DSC measurements are shown in Section S3 of the Supporting Information.

2.6. DNP-Enhanced ^{13}C Solid State NMR Spectroscopy. Approximately 10 mg of the respective sample was transferred into a 3.2 mm sapphire rotor. The rotor was sealed with a Teflon plug and closed with a ZrO_2 driving cap.

All DNP ssNMR measurements were conducted on a Bruker AVANCE III 400 DNP NMR spectrometer operating at 9.4 T (401.63 MHz for ^1H, 100.99 MHz for ^{13}C) at a MAS rate of 8 kHz. A 9.7 T Bruker gyrotron system was used to generate microwaves (μw) at 263 GHz frequency. The spectrometer is equipped with a 3.2 mm low temperature H/X/Y triple resonance probe that was used in $^1H/^{13}C/Y$ triple mode throughout the measurements. Sample temperatures were nominally 112 and 122 K for data obtained without and with μw irradiation of the sample, respectively. Heteronuclear decoupling was performed during data acquisition employing the SPINAL-64 decoupling sequence.[60]

Enhancement factors for ^{13}C were evaluated based on $^1H \rightarrow {}^{13}C$ cross-polarization (CP) MAS experiments. The contact time in these experiments was set to 2 ms; a ramped pulse was applied on the ^1H-channel. 512 scans with a recycle delay of 4 s were recorded. Nominal values of the enhancement factors were obtained by scaling the peak maxima of the μw off spectra to those of the μw on spectra. The errors of the enhancement factors were estimated by adding the percentage error of the noise level of both acquired spectra. The corresponding spectra and enhancement factors are shown in Section S4 of the Supporting Information.

Saturation recovery experiments were employed to determine the polarization buildup of the investigated carbon atoms. These experiments were performed with microwave irradiation (μw on). A pulse train consisting of twenty $\pi/2$-pulses with a respective pulse length of 3.5 μs and a spacing of 5 ms between the pulses was used to initially quench the ^{13}C magnetization. Buildup times τ_b of 16, 32, 64, 128, 250, 500, and 1400 s were used, recording 64 scans for Triton and 32 scans for all other surfactant samples.

To selectively address the direct polarization transfer path, a pulse sequence introduced by the authors in an earlier publication was applied.[40] In this pulse sequence, the standard saturation recovery experiment was modified by the addition of a train of rotor-synchronized π-pulses with a pulse length of 6 μs and a pulse spacing of 500 ms on the ^1H channel during the buildup of ^{13}C magnetization, which purges the buildup of ^1H magnetization.

The obtained spectra of the direct polarization pathway were subtracted from the spectra showing the superposition of the direct and indirect pathways to obtain the spectra only displaying the indirect polarization pathway. The spectra were deconvoluted using Lorentzian line shapes to determine intensities for all signals. The intensities of the signals of interests, namely the PEG units of the surfactants, were plotted against the utilized τ_b to allow for further analysis.

Additionally, exemplary heteronuclear correlation (HETCOR) experiments were conducted to verify the data obtained from the DNP NMR spectra and to confirm the model developed in this work. The data as well as the experimental details are shown in Section S7 of the Supporting Information.

https://doi.org/10.1021/acs.jpcc.3c01946
J. Phys. Chem. C 2023, 127, 12125−12134

3. RESULTS AND DISCUSSION

3.1. Characterization of the Mesoporous Silica Materials. To characterize the utilized silica materials and in order to understand their pore structure, the materials were inspected by adsorption/desorption experiments utilizing the BET model for analysis.[54] Table 1 summarizes the results of these measurements.

Table 1. Characterization Results Obtained by the Adsorption/Desorption Measurements

method/material	SBA-15	MCM 41
BET surface area/m^2 g^{-1}	555	899
pore size (NLDFT)/nm	7.0	4.0
pore volume (Gurvich)/cm^3 g^{-1}	0.76	0.89
pore surface/m^2 g^{-1}	534	1040

Unlike MCM 41, SBA-15 usually features micropores in the form of channels connecting the mesopores.[61] However, the contribution of these micropores to the total pore volume is small,[62] especially for SBA-15 materials with a moderate surface area, as the one utilized in this study.[63] Therefore, the micropores are not discussed further in this work. The pore size distribution obtained by NLDFT is shown in Figure S1 in the Supporting Information.

As the goal of this work was to probe a potential influence of confinement on the polarization transfer behavior of polarizing agents dissolved in surfactants, two different pore sizes were chosen for investigation. To achieve that, SBA-15 and MCM 41 mesoporous silica materials were used. In order to understand how the surfactants interact with the pore surface, it is integral to consider the size of these molecules in comparison to the size of the pore they are confined in. To evaluate whether the pores could accommodate the guest molecules, their maximum size is estimated based on their stretched conformation using a 3D modeling program, namely Chem3D. The amount of ethylene glycol units considered for the length estimation for each of the polydisperse surfactants is based on their composition analysis published previously.[40]

The shortest surfactant investigated in this work is PEG 200, with an average of four ethylene glycol units and an approximate length of 1.6 nm. The other estimated lengths are 1.9 nm for E_5, 3.5 nm for $C_{10}E_6$ and 4.1 nm for Triton. As interactions of the surfactants and the pore wall are certainly taking place, an at least partially perpendicular orientation of the surfactant molecules on the pore wall is assumed. Hence, the dimension of relevance for the adsorption of the surfactants into the pores is the pore diameter. A conceivable lengthwise adsorption along the pore axis is entropically unfavorable as it would not represent the structure with the largest cohesive force.[64]

A comparison of these estimated lengths to the pore diameters reveals that all surfactants can be accommodated by the SBA-15 material in an arbitrary orientation, even in their longest assumed conformation. As for the MCM 41 porous material, especially the larger surfactants investigated in this work, $C_{10}E_6$ and Triton with an average of six and nine ethylene glycol units, respectively, are approximately as long or longer than the pore diameter. However, as the investigated surfactants are not rigid molecules, they are expected to coil via the formation of inter- and intramolecular hydrogen bonds for the PEG units and van der Waals interactions for the hydrocarbons, as well as by entropic forces.[65−68] This behavior reduces the effective length of the surfactants to a fraction of their length in the stretched conformation,[69,70] therefore allowing for the absorption into the pores.

For AMUPol, a size of 1.8 nm is estimated with its polyethylene chain fully stretched. Therefore, the polarizing agent is significantly smaller than the pores of the utilized silica materials, enabling the radical to be absorbed into the pores easily.

3.2. ^{13}C MAS DNP Spectra. Figure 2 shows the ^{13}C MAS ssNMR spectra obtained for the samples investigated in this study for a long buildup time of 1400 s where the signal-to-noise ratio is the highest and, thus, spectral features are best observable. In Figure 2, each column represents one of the surfactants, while each row corresponds to one of the two amorphous silica materials. The spectra for the direct and indirect pathway, their superposition as well as the spectra without microwave irradiation (with their respective magnification factors for better visibility, if applicable) are displayed.

PEG 200 and E_5 only display two resonances for all recorded spectra. The signal at approximately 60 ppm corresponds to the carbon atoms at the end of the PEG chain, next to the terminal hydroxyl group. The signal at 70 ppm is attributed to all other carbon atoms in the PEG chain, as they are not discernible under the utilized experimental conditions.

For these two surfactants, the resonances assigned to the direct and indirect polarization transfer pathway are almost of the same size for the sample confined in SBA-15. Both signals are evenly enhanced through the direct polarization experiments for both sets of resonances. For the samples confined in MCM 41, the resonances assigned to the indirect polarization transfer pathway are predominant, leading to overall negative signals in the superposition of both polarization transfer pathways.

$C_{10}E_6$ and Triton display additional signals to those caused by the PEG unit. As can be seen in Figure 1, $C_{10}E_6$ contains an aliphatic decyl unit that causes signals between 0 and 40 ppm. However, these signals overlap severely so that only four distinct signals are discernible under the present conditions. For both utilized amorphous silica materials, the resonances assigned to the indirect polarization transfer pathway of those carbon atoms are larger than those for the direct polarization transfer pathway. As indirect polarization transfer is favored on certain nuclei based on their dynamics or their proximity to the polarizing agent,[15,40,50] this implies that these carbons take part in motional fluctuations with correlation times shorter than the inverse resonance frequency or that there is a large distance between them and the AMUPol molecules.[71−73] Aliphatic chains are lipophilic, therefore hindering interactions with the hydrophilic AMUPol. Hence, a larger indirect signal is expected here.

Triton features a tetramethylbutylphenyl moiety in addition to the PEG units, which causes signals between 0 and 40 ppm for the aliphatic carbons as well as between 105 and 160 ppm for the aromatic carbons (see Figure 1).

Due to their poor signal quality, the signals not corresponding to PEG units were not analyzed and discussed in this work.

To get more insights into the relation of the polarizing agent with the investigated confined surfactants, the signals attributed to the PEG units were deconvoluted, resulting in the signal intensities for the direct and indirect pathway, respectively. The signal intensity produced by direct polarization is expressed as percentage of the total signal intensity,

https://doi.org/10.1021/acs.jpcc.3c01946
J. Phys. Chem. C 2023, 127, 12125−12134

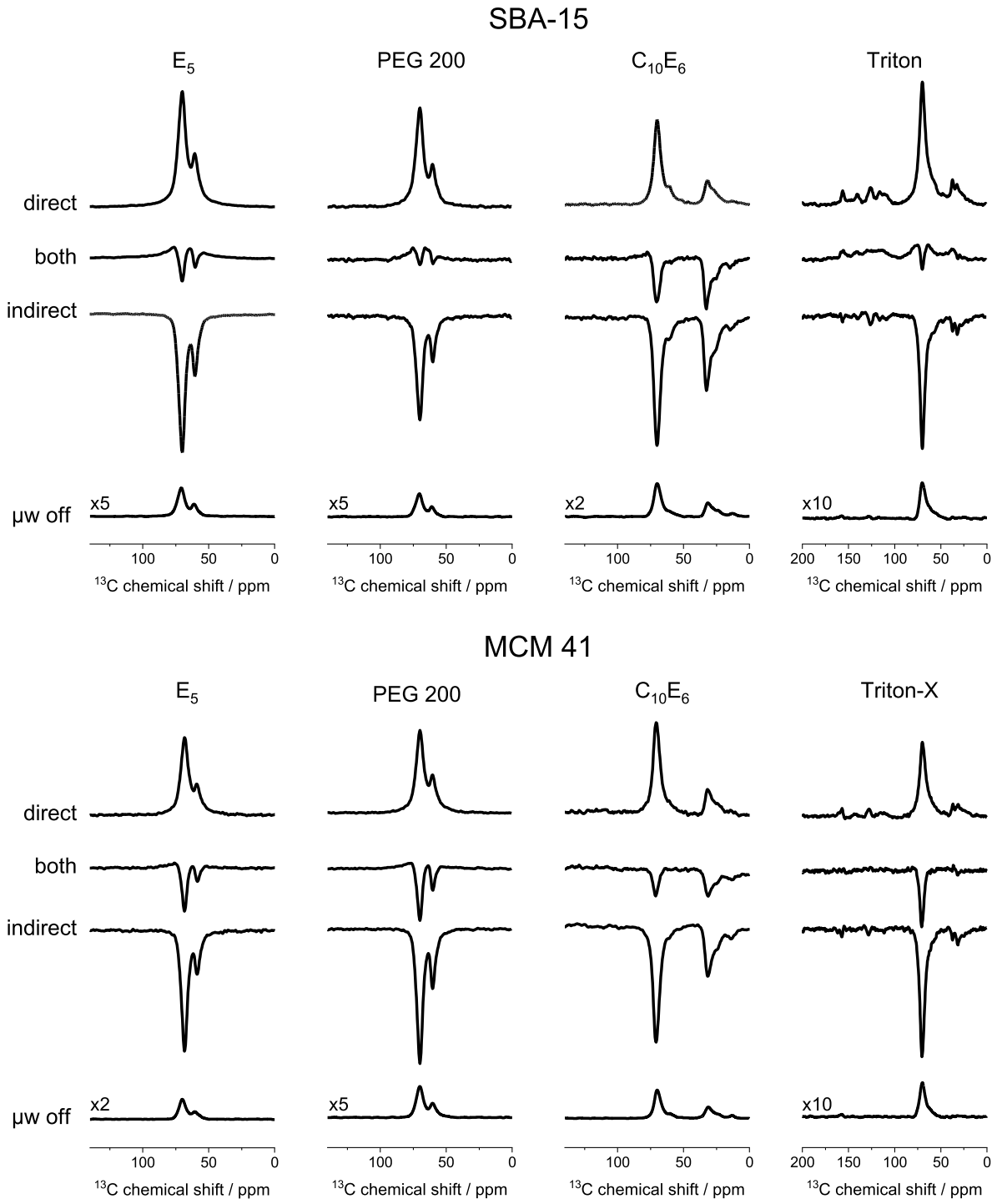

Figure 2. ^{13}C MAS ssNMR spectra acquired in this work at a buildup time of 1400 s. The spectra obtained for the direct and indirect polarization as well as their superposition are displayed in the first three rows of spectra for each spectra set. Also shown are the spectra measured without μw irradiation with their respective scaling factors for better visibility. The upper panel shows the spectra obtained for SBA-15, and the lower panel shows the spectra obtained for MCM 41.

as established in our previous work.[15] Figure 3 summarizes the obtained results for all investigated samples, allowing a comparison of the polarizing behavior of the different samples.

For E_5 and for PEG 200, similar curves are observed in Figure 3. Both the carbons at the end of the PEG chain at 60 ppm as well as the carbons in the chain itself at 70 ppm display approximately 40−60% of direct polarization expressed as percentage of the total signal intensity. However, the silica materials in which the surfactants are confined appear to have significant influence on the polarization transfer pathway. On average, the E_5 and the PEG 200 confined in MCM 41 display less direct polarization transfer than those confined in SBA-15. This indicates the involvement of motions of the PEG units on a timescale shorter than the inverse resonance frequency or a larger spatial distance between the carbons of the surfactants confined in the MCM 41 as compared to those in the SBA-15

https://doi.org/10.1021/acs.jpcc.3c01946
J. Phys. Chem. C 2023, 127, 12125−12134

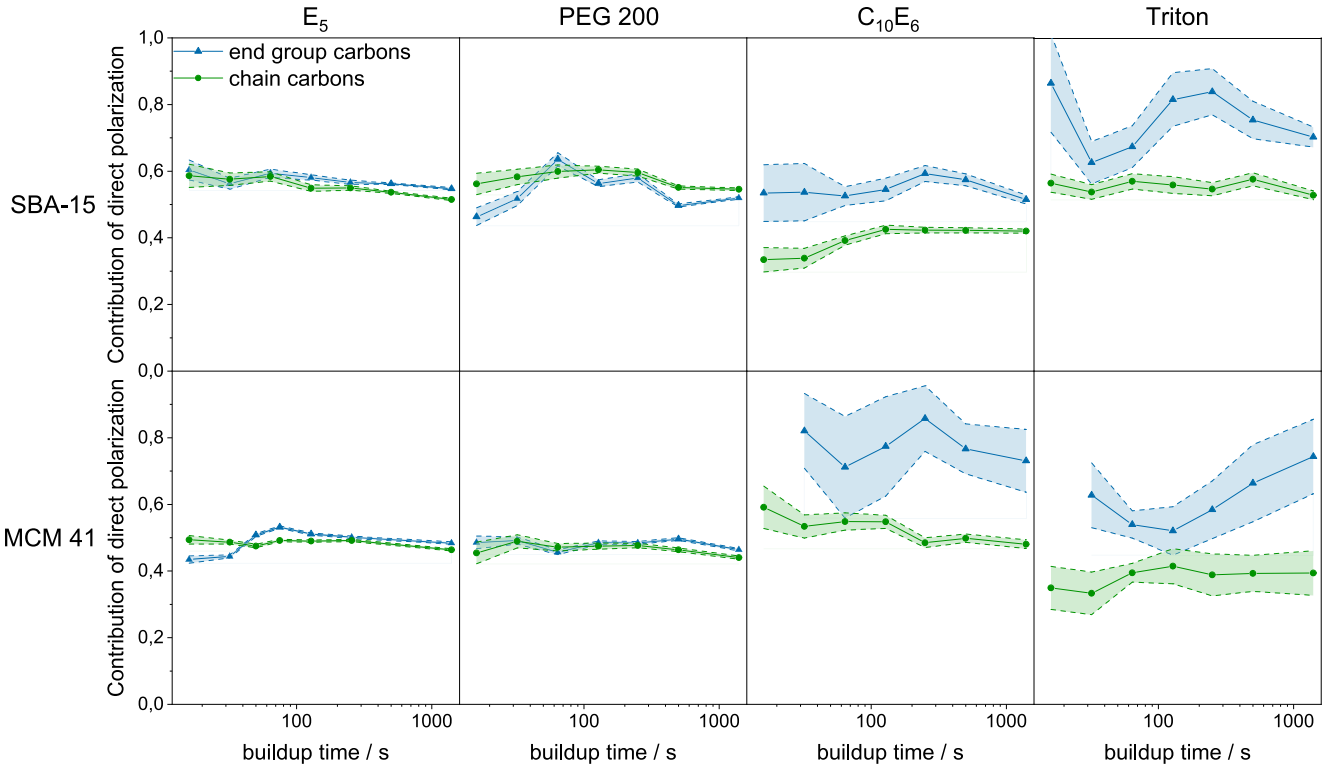

Figure 3. Ratios of signal intensity produced via direct polarization compared to the total signal intensity for the carbons of the PEG unit for all surfactants confined in the two mesoporous silica materials, SBA-15 and MCM 41.

.[49,50] As discussed above, the AMUPol molecule is small enough to be confined into the pores of the mesoporous MCM 41. Therefore, it is unlikely that the smaller pore size leads to considerably higher distance between the carbon atoms of the surfactants and the polarizing agent. It is more likely that the smaller pore size increases the statistical disorder of the confined molecules, therefore impeding interactions between the molecules and allowing for higher mobility of the PEG chains.

For $C_{10}E_6$ and Triton, differences between the carbons at the end of the PEG moieties and those in the middle of the chain become apparent. The carbons at the end show a significantly higher amount of direct polarization than the ones in the middle of the chain. This might seem counterintuitive, since a high mobility is expected for these carbons, as observed for bulk $C_{10}E_6$ in an earlier report by some of the authors.[41] This high mobility would substantiate ideal conditions for the indirect polarization transfer pathway, assuming the time scale of the dynamics is different from the corresponding Larmor frequencies.[74,75] However, specific interactions with the amorphous silica material need to be considered as well. For E_5 and PEG 200, it is assumed that the majority of the carbon atoms interact with the silica materials in a similar manner since they have very similar properties in terms of hydrophilicity. Additionally, all carbons are neighboring oxygen atoms that are able to accept hydrogen bonds. Statistically, any carbon can point toward the silica surface and the terminal hydroxyl group could also point inward into the coiled PEG to form hydrogen bonds.[65] The molecules $C_{10}E_6$ and Triton consist of a hydrophilic moiety (the PEG unit) and a hydrophobic moiety (the aliphatic carbon chain and the tetramethylbutylphenyl group, respectively) and are amphiphilic. The hydrophobic groups cannot interact with the surface of the silica pores and cannot form hydrogen bonds. It is, therefore, assumed that these moieties are oriented toward the pore center, leaving the PEG unit pointing toward the wall of the pore. Since AMUPol is a hydrophilic radical,[51] it is also assumed that it is concentrated primarily toward the pore wall where the PEG units of the amphiphilic surfactants are located. From the data presented in Figure 3, it is assumed that the terminal hydroxyl group of the amphiphilic surfactants is responsible for the main interactions with the surface of the silica pores as it shows a high amount of direct pathway polarization, indicating low mobility due to the strong hydrogen bonds and close proximity to the polarizing agent. The lipophilic part of the surfactants, which cannot fold onto the hydrophilic PEG units, points toward the pore center, away from the AMUPol, causing the observed larger amount of indirect channel polarization.

3.3. Line Width Analysis. To further illustrate the effect of the confinement on the surfactants as well as to confirm the results obtained by analyzing the contributions of the direct and indirect pathways, the full widths at half maximum (FWHM) of the signals are evaluated. The FWHM of the investigated signals for all samples at τ_b = 1400 s are shown in Figure 4.

For all observed signals, the indirect pathway resonances display a smaller line width than the corresponding resonances assigned to the direct polarization pathway, as shown in Figure 4 and observed in Figure 2. This is in agreement with observations made in earlier works concerning similar surfactant systems.[41,49,50] The signals of the indirect polarization pathway are caused by the transfer of polarization from the proton reservoir to the observed carbon nucleus. This allows for the observation of nuclei farther away from the polarizing agent, since the polarization can travel through the

https://doi.org/10.1021/acs.jpcc.3c01946
J. Phys. Chem. C 2023, 127, 12125−12134

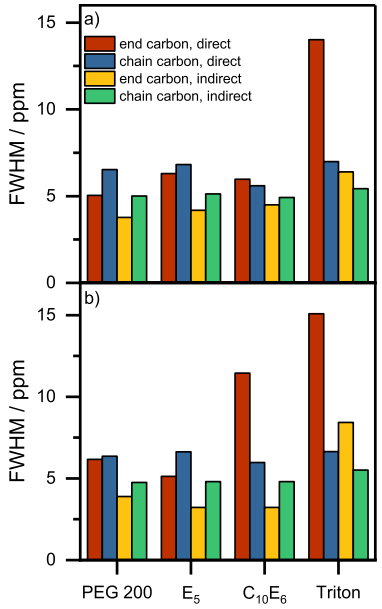

Figure 4. FWMH of the signals caused by direct polarization and those caused by indirect polarization corresponding to the end group and the chain carbons of the PEG units of all investigated surfactants confined in (a) SBA-15 and (b) MCM 41.

whole sample via the proton reservoir. Carbon atoms polarized by the direct polarization pathway need to be in direct contact with the radical moiety to be polarized. Hence, the carbons corresponding to the indirect signal do not experience the same amount of paramagnetic broadening, leading to narrower signals.

For E_5 and PEG 200, the signals corresponding to the PEG chain are approximately as broad as or slightly broader than those corresponding to the end group carbons, indicating a similar proximity of the end group carbons and the chain carbons to the polarizing agent.

For the amphiphilic surfactants, $C_{10}E_6$ and Triton, a different trend is observable. Despite the signal at 70 ppm corresponding to more nuclei that all experience a slightly different environment, the signal assigned to the direct polarization pathway that corresponds to the end groups is as broad (for the case of $C_{10}E_6$ confined in SBA-15) or significantly broader than that of the ethylene glycol chain (for $C_{10}E_6$ confined in MCM 41 and for all confined Triton samples). Additionally, upon closer inspection of the spectra displayed in Figure 2, it is apparent that the end group carbons exhibit substantially less signal than those in the PEG units. As the end groups have been observed to display more direct than indirect polarization and are therefore more likely to be closer to the hydrophilic polarizing agent AMUPol, they are likely to experience large broadening due to the contact with the paramagnetic radical moiety, rendering the signal unobservable in the most severe cases. Unlike the chain carbons, there are no end group carbons facing away from the polarizing agent that could contribute to a narrow indirect polarization transfer pathway signal for Triton. Hence, the broadening translates into the observed indirect signals corresponding to the end group carbons, leading to unusually broad signals for the resonances assigned to the indirect polarization transfer pathway. This indicates that the polarizing agent highly localized at the end group carbons. For $C_{10}E_6$, a strong broadening of the indirect signal of the end group carbons is not observed, suggesting a slightly better mixing of the AMUPOL with the PEG units of the $C_{10}E_6$.

3.4. Development of a Model for the Surfactant Arrangement in the Pores. According to the data obtained by the line width analysis and the determination of the relative contribution of the direct and indirect polarization pathway, a schematic representation is developed to show the arrangement of the surfactant in the silica pores. The corresponding illustration can be found in Figure 5. Here, the silica walls are displayed in a stylized manner, with the surfactants being represented in two different arrangements, depending on whether they are hydro- or amphiphilic.

The hydrophilic surfactants, E_5 and PEG 200, coil and mix with the hydrophilic polarizing agent AMUPol, forming a homogeneous mixture. Additionally, each carbon of the two investigated PEGs has an equal opportunity to be in close proximity to the silica wall, since each carbon neighbors an oxygen atom capable of forming hydrogen bonds. Therefore, no differences in polarization behavior or line width are observed for the end group carbon atoms compared to the chain carbon atoms.

For the amphiphilic surfactants, $C_{10}E_6$ and Triton, it has been shown that the carbon atoms in the end group experience more direct polarization than those located in the PEG chains. To explain the larger amount of direct polarization experienced by the end groups, they have to be located in a close proximity to the polarizing agent, closer than the rest of the PEG chain carbons. The dominance of the direct polarization transfer

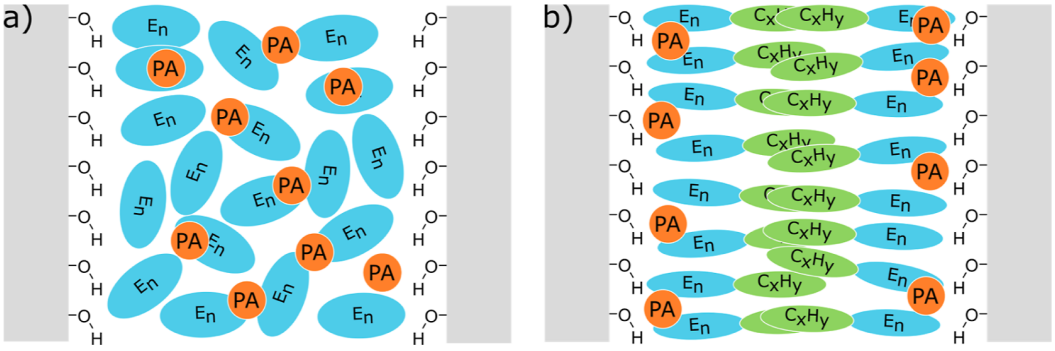

Figure 5. Schematic illustration of (a) the hydrophilic surfactants (E_5 and PEG 200) and (b) the amphiphilic surfactants ($C_{10}E_6$ and Triton) oriented in the pores of the mesoporous silica host material. E_n represents the PEG units, C_xH_y represents the lipophilic moiety of the amphiphilic surfactants and PA represents the polarizing agent AMUPol (not to scale).

https://doi.org/10.1021/acs.jpcc.3c01946
J. Phys. Chem. C 2023, 127, 12125−12134

pathway also indicates a lack of dynamics, indicating that the hydroxyl group at the end of the PEG unit mediates the interactions of the molecule with the silica walls, forming hydrogen bonds. In addition, the analysis of the FWHM has shown a large broadening of the signal of the end groups for both surfactants that is caused by the interactions of the carbons with a paramagnetic moiety, namely the radical centers of the polarizing agent. This further confirms the adjacency of the polarizing agent and the end group carbon atoms. Considering the present data, an arrangement of the amphiphilic surfactants as shown in Figure 5b is highly likely.

Interestingly, this work has shown that the influence of the pore size on the arrangement of the surfactants in the pore is negligible. Both systems, those with surfactants confined in SBA-15 as well as in MCM 41, show very similar patterns of polarization transfer and line widths.

4. CONCLUSIONS

DNP-enhanced ssNMR of two different classes of surfactants employing AMUPol as polarization agent was used to investigate how four commercially available surfactants (E_5, PEG 200, $C_{10}E_6$, and Triton) interact with two different mesoporous silica materials, SBA-15 and MCM 41. DSC measurements were performed to confirm that the surfactants are indeed confined in the pores of the silica materials and to observe the changes in their melting and crystallization behavior while confined.

A previously established relative method was used to quantify the proportion of directly transferred polarization expressed as a percentage of the total signal intensity in order to achieve comparable results across all samples, independent of radical concentration and amount of sample used. Employing this method, it could be shown that each of the carbon atoms in PEG 200 and E_5 interacts with the silica pore and the polarizing agent in a similar manner, leading to an even pattern of polarization transfer across all of them. Both the terminal carbon atom as well as the atoms in the PEG chain receive equal amounts of direct polarization.

For $C_{10}E_6$ and Triton, the terminal carbon of the PEG chain receives more direct polarization than the ones in the chain, indicating that the terminal carbons are less mobile due to the interactions of the hydroxyl group with the wall of the silica pores. It also indicates a close proximity of the hydrophilic AMUPol with the PEG units of the surfactants.

Through the analysis of the signal line widths of the investigated signals, it could be shown that the signals corresponding to the end groups of the PEG chains are broader for the amphiphilic surfactants compared to those of the hydrophilic surfactants. This indicates a close spatial proximity of the radical moieties of the polarizing agent to the end group carbons, leading to paramagnetic broadening and bleaching of the signal.

Combining the data collected in this work, a model of the arrangement of the surfactants in the silica mesopores could be developed, illustrating that the hydrophilic surfactants interact with the pore surface in a significantly different manner than the amphiphilic ones.

This work illustrates that the method of measuring direct polarization DNP-enhanced ssNMR spectra aids in understanding the complex interplay of confined molecules with their host system. Especially, the combination of direct and indirect polarization with line width analyses allows for the development of a model of how different classes of surfactants arrange themselves within the pores of their mesoporous silica host materials. It also extends the use of a relative method of spectral analysis of direct and indirect DNP NMR spectra, enabling the comparison of different samples without having to account for sample mass or the exact concentration of the polarizing agent.

■ ASSOCIATED CONTENT

Supporting Information

The Supporting Information is available free of charge at https://pubs.acs.org/doi/10.1021/acs.jpcc.3c01946.

Details on utilized chemicals including structural analysis detailing the lengths of the polydisperse surfactants; pore size distribution of the utilized SBA-15; DSC data and their interpretation; $^1H \rightarrow {}^{13}C$ CP MAS DNP NMR spectra and their interpretation; exemplary deconvolution of ^{13}C DNP NMR spectra; ^{13}C buildup curves; and exemplary HETCOR spectra (PDF)

■ AUTHOR INFORMATION

Corresponding Author

Gerd Buntkowsky − *Department of Chemistry, Eduard-Zintl-Institute for Inorganic and Physical Chemistry, Technical University of Darmstadt, 64287 Darmstadt, Germany;* orcid.org/0000-0003-1304-9762; Email: gerd.buntkowsky@chemie.tu-darmstadt.de

Authors

Sonja C. Döller − *Department of Chemistry, Eduard-Zintl-Institute for Inorganic and Physical Chemistry, Technical University of Darmstadt, 64287 Darmstadt, Germany*

Martin Brodrecht − *Department of Chemistry, Eduard-Zintl-Institute for Inorganic and Physical Chemistry, Technical University of Darmstadt, 64287 Darmstadt, Germany*

Torsten Gutmann − *Department of Chemistry, Eduard-Zintl-Institute for Inorganic and Physical Chemistry, Technical University of Darmstadt, 64287 Darmstadt, Germany;* orcid.org/0000-0001-6214-2272

Markus Hoffmann − *Department of Chemistry and Biochemistry, State University of New York College at Brockport, Brockport, New York 14420, United States;* orcid.org/0000-0002-5469-8665

Complete contact information is available at: https://pubs.acs.org/10.1021/acs.jpcc.3c01946

Notes

The authors declare no competing financial interest.

■ ACKNOWLEDGMENTS

Financial support by the Deutsche Forschungsgemeinschaft under Contract Bu-911-24-2 and by the National Science Foundation under grant no. 1953428 are gratefully acknowledged. We thank Rochester Midland Corporation for donating the polydisperse surfactants.

■ REFERENCES

(1) François, I.; Sandra, K.; Sandra, P. Comprehensive Liquid Chromatography: Fundamental Aspects and Practical Considerations—A Review. *Anal. Chim. Acta* **2009**, *641*, 14−31.

(2) Li, Z.; Rösler, L.; Wissel, T.; Breitzke, H.; Gutmann, T.; Buntkowsky, G. Immobilization of a Chiral Dirhodium Catalyst on SBA-15 via Click-Chemistry: Application in the Asymmetric Cyclo-

propanation of 3-Diazooxindole With Aryl Alkenes. *J. CO2 Util.* **2021**, *52*, 101682−101690.
(3) Costa, J. A. S.; de Jesus, R. A.; Santos, D. O.; Neris, J. B.; Figueiredo, R. T.; Paranhos, C. M. Synthesis, Functionalization, and Environmental Application of Silica-Based Mesoporous Materials of the M41S and SBA-n Families: A Review. *J. Environ. Chem. Eng.* **2021**, *9*, 105259−105288.
(4) Murillo-Cremaes, N.; López-Periago, A. M.; Saurina, J.; Roig, A.; Domingo, C. Nanostructured Silica-Based Drug Delivery Vehicles for Hydrophobic and Moisture Sensitive Drugs. *J. Supercrit. Fluids* **2013**, *73*, 34−42.
(5) Brodrecht, M.; Kumari, B.; Thankamony, A. S. S. L.; Breitzke, H.; Gutmann, T.; Buntkowsky, G. Structural Insights into Peptides Bound to the Surface of Silica Nanopores. *Chem.—Eur. J.* **2019**, *25*, 5214−5221.
(6) Brodrecht, M.; Kumari, B.; Breitzke, H.; Gutmann, T.; Buntkowsky, G. Chemically Modified Silica Materials as Model Systems for the Characterization of Water-Surface Interactions. *Z. Phys. Chem.* **2018**, *232*, 1127−1146.
(7) Zhao, D.; Feng, J.; Huo, Q.; Melosh, N.; Fredrickson, G. H.; Chmelka, B. F.; Stucky, G. D. Triblock Copolymer Syntheses of Mesoporous Silica with Periodic 50 to 300 Angstrom Pores. *Science* **1998**, *279*, 548−552.
(8) Beck, J. S.; Vartuli, J. C.; Roth, W. J.; Leonowicz, M. E.; Kresge, C. T.; Schmitt, K. D.; Chu, C. T. W.; Olson, D. H.; Sheppard, E. W.; McCullen, S. B.; et al. A New Family of Mesoporous Molecular Sieves Prepared with Liquid Crystal Templates. *J. Am. Chem. Soc.* **1992**, *114*, 10834−10843.
(9) Kumari, B.; Brodrecht, M.; Breitzke, H.; Werner, M.; Grünberg, B.; Limbach, H.-H.; Forg, S.; Sanjon, E. P.; Drossel, B.; Gutmann, T.; et al. Mixtures of Alcohols and Water confined in Mesoporous Silica: A Combined Solid-State NMR and Molecular Dynamics Simulation Study. *J. Phys. Chem. C* **2018**, *122*, 19540−19550.
(10) Ben Shir, I.; Kababya, S.; Schmidt, A. Binding Specificity of Amino Acids to Amorphous Silica Surfaces: Solid-State NMR of Glycine on SBA-15. *J. Phys. Chem. C* **2012**, *116*, 9691−9702.
(11) Dosseh, G.; Xia, Y.; Alba-Simionesco, C. Cyclohexane and Benzene Confined in MCM-41 and SBA-15: Confinement Effects on Freezing and Melting. *J. Phys. Chem. B* **2003**, *107*, 6445−6453.
(12) Alba-Simionesco, C.; Coasne, B.; Dosseh, G.; Dudziak, G.; Gubbins, K. E.; Radhakrishnan, R.; Sliwinska-Bartkowiak, M. Effects of Confinement on Freezing and Melting. *J. Phys.: Condens. Matter* **2006**, *18*, R15−R68.
(13) Gedat, E.; Schreiber, A.; Albrecht, J.; Emmler, T.; Shenderovich, I.; Findenegg, G. H.; Limbach, H.-H.; Buntkowsky, G. ^{2}H-Solid-State NMR Study of Benzene-d_6 Confined in Mesoporous Silica SBA-15. *J. Phys. Chem. B* **2002**, *106*, 1977−1984.
(14) Hassan, J. Analysis of 2H NMR Spectra of Water Molecules on the Surface of Nano-Silica Material MCM-41: Deconvolution of the Signal Into a Lorentzian and a Powder Pattern Line Shapes. *Phys. B* **2012**, *407*, 179−183.
(15) Buntkowsky, G.; Döller, S. C.; Haro-Mares, N.; Gutmann, T.; Hoffmann, M. Solid-State NMR Studies of Non-Ionic Surfactants Confined in Mesoporous Silica. *Z. Phys. Chem.* **2022**, *236*, 939−960.
(16) Amitay-Rosen, T.; Kababya, S.; Vega, S. A Dynamic Magic Angle Spinning NMR Study of the Local Mobility of Alanine in an Aqueous Environment at the Inner Surface of Mesoporous Materials. *J. Phys. Chem. B* **2009**, *113*, 6267−6282.
(17) Amitay-Rosen, T.; Vega, S. A Deuterium MAS NMR Study of the Local Mobility of Dissolved Methionine and Di-Alanine at the Inner Surface of SBA-15. *Phys. Chem. Chem. Phys.* **2010**, *12*, 6763−6773.
(18) Werner, M.; Rothermel, N.; Breitzke, H.; Gutmann, T.; Buntkowsky, G. Recent Advances in Solid State NMR of Small Molecules in Confinement. *Isr. J. Chem.* **2014**, *54*, 60−73.
(19) Buntkowsky, G.; Breitzke, H.; Adamczyk, A.; Roelofs, F.; Emmler, T.; Gedat, E.; Grünberg, B.; Xu, Y.; Limbach, H.-H.; Shenderovich, I.; et al. Structural and Dynamical Properties of Guest Molecules Confined in Mesoporous Silica Materials Revealed by NMR. *Phys. Chem. Chem. Phys.* **2007**, *9*, 4843−4853.
(20) Anastas, P. T.; Warner, J. C. *Green Chemistry: Theory and Practice*; Oxford University Press: Oxford, 1998.
(21) Hoffmann, M. M. Polyethylene Glycol as a Green Chemical Solvent. *Curr. Opin. Colloid Interface Sci.* **2022**, *57*, 101537.
(22) La Sorella, G.; Strukul, G.; Scarso, A. Recent Advances in Catalysis in Micellar Media. *Green Chem.* **2015**, *17*, 644−683.
(23) Fernandez, A. M.; Held, U.; Willing, A.; Breuer, W. H. New Green Surfactants for Emulsion Polymerization. *Prog. Org. Coat.* **2005**, *53*, 246−255.
(24) Andrade, C. Z.; Alves, L. Environmentally Benign Solvents in Organic Synthesis: Current Topics. *Curr. Org. Chem.* **2005**, *9*, 195−218.
(25) de Oliveira, C. A. F.; Guimares, C. R. W.; de Alencastro, R. B. Molecular Dynamics Study on Liquid 1-Octanol. *Int. J. Quantum Chem.* **2000**, *80*, 999−1006.
(26) Huyskens, P.; Ruelle, P. Dynamic Equilibrium Time Fractions or Fractional Lifetimes? The Final Chapter. *J. Mol. Liq.* **2000**, *88*, 87−108.
(27) Hu, K.; Zhou, Y.; Shen, J.; Ji, Z.; Cheng, G. Micro-heterogeneous Structure of 1-Octanol in Neat and Water-Saturated State. *J. Phys. Chem. B* **2007**, *111*, 10160−10165.
(28) Döller, S. C.; Brodrecht, M.; Haro Mares, N. B.; Breitzke, H.; Gutmann, T.; Hoffmann, M.; Buntkowsky, G. Deuterium NMR Studies of the Solid−Liquid Phase Transition of Octanol-d_{17} Confined in SBA-15. *J. Phys. Chem. C* **2021**, *125*, 25155−25164.
(29) Zaera, F. Probing Liquid/Solid Interfaces at the Molecular Level. *Chem. Rev.* **2012**, *112*, 2920−2986.
(30) Blum, F. D.; Xu, G.; Liang, M.; Wade, C. G. Dynamics of Poly(vinyl acetate) in Bulk and on Silica. *Macromolecules* **1996**, *29*, 8740−8745.
(31) Buntkowsky, G.; Vogel, M. Small Molecules, Non-Covalent Interactions, and Confinement. *Molecules* **2020**, *25*, 3311−3342.
(32) Rorschach, H.; Hazlewood, C. Protein Dynamics and the NMR Relaxation Time T_1 of Water in Biological Systems. *J. Magn. Reson.* **1986**, *70*, 79−88.
(33) Brown, M. F.; Ribeiro, A. A.; Williams, G. D. New View of Lipid Bilayer Dynamics from ^{2}H and ^{13}C NMR Relaxation Time Measurements. *Proc. Natl. Acad. Sci. U.S.A.* **1983**, *80*, 4325−4329.
(34) Weigler, M.; Winter, E.; Kresse, B.; Brodrecht, M.; Buntkowsky, G.; Vogel, M. Static Field Gradient NMR Studies of Water Diffusion in Mesoporous Silica. *Phys. Chem. Chem. Phys.* **2020**, *22*, 13989−13998.
(35) Ni, Q. Z.; Daviso, E.; Can, T. V.; Markhasin, E.; Jawla, S. K.; Swager, T. M.; Temkin, R. J.; Herzfeld, J.; Griffin, R. G. High Frequency Dynamic Nuclear Polarization. *Acc. Chem. Res.* **2013**, *46*, 1933−1941.
(36) Griffin, R. G.; Prisner, T. F. High Field Dynamic Nuclear Polarization−The Renaissance. *Phys. Chem. Chem. Phys.* **2010**, *12*, 5737−5740.
(37) Lesage, A.; Lelli, M.; Gajan, D.; Caporini, M. A.; Vitzthum, V.; Miéville, P.; Alauzun, J.; Roussey, A.; Thieuleux, C.; Mehdi, A.; et al. Surface Enhanced NMR Spectroscopy by Dynamic Nuclear Polarization. *J. Am. Chem. Soc.* **2010**, *132*, 15459−15461.
(38) Daube, D.; Aladin, V.; Heiliger, J.; Wittmann, J. J.; Barthelmes, D.; Bengs, C.; Schwalbe, H.; Corzilius, B. Heteronuclear Cross-Relaxation under Solid-State Dynamic Nuclear Polarization. *J. Am. Chem. Soc.* **2016**, *138*, 16572−16575.
(39) Bothe, S.; Hoffmann, M. M.; Gutmann, T.; Buntkowsky, G. Comparative Study of the Magnetic Field Dependent Signal Enhancement in Solid-State Dynamic Nuclear Polarization Experiments. *J. Phys. Chem. C* **2017**, *121*, 27089−27097.
(40) Hoffmann, M. M.; Bothe, S.; Gutmann, T.; Hartmann, F.-F.; Reggelin, M.; Buntkowsky, G. Directly vs. Indirectly Enhanced ^{13}C in Dynamic Nuclear Polarization Magic Angle Spinning NMR Experiments of Nonionic Surfactant Systems. *J. Phys. Chem. C* **2017**, *121*, 2418−2427.

https://doi.org/10.1021/acs.jpcc.3c01946
J. Phys. Chem. C 2023, 127, 12125−12134

(41) Hoffmann, M. M.; Bothe, S.; Gutmann, T.; Buntkowsky, G. Unusual Local Molecular Motions in the Solid State Detected by Dynamic Nuclear Polarization Enhanced NMR Spectroscopy. *J. Phys. Chem. C* **2017**, *121*, 22948−22957.
(42) Aladin, V.; Corzilius, B. Methyl Dynamics in Amino Acids Modulate Heteronuclear Cross Relaxation in the Solid State Under MAS DNP. *Solid State Nucl. Magn. Reson.* **2019**, *99*, 27−35.
(43) Aladin, V.; Vogel, M.; Binder, R.; Burghardt, I.; Suess, B.; Corzilius, B. Complex Formation of the Tetracycline-Binding Aptamer Investigated by Specific Cross-Relaxation under DNP. *Angew. Chem., Int. Ed.* **2019**, *58*, 4863−4868.
(44) Ni, Q. Z.; Markhasin, E.; Can, T. V.; Corzilius, B.; Tan, K. O.; Barnes, A. B.; Daviso, E.; Su, Y.; Herzfeld, J.; Griffin, R. G. Peptide and Protein Dynamics and Low-Temperature/DNP Magic Angle Spinning NMR. *J. Phys. Chem. B* **2017**, *121*, 4997−5006.
(45) Park, H.; Uluca-Yazgi, B.; Heumann, S.; Schlögl, R.; Granwehr, J.; Heise, H.; Schleker, P. P. M. Heteronuclear Cross-Relaxation Effect Modulated by the Dynamics of N-Functional Groups in the Solid State Under ^{15}N DP-MAS DNP. *J. Magn. Reson.* **2020**, *312*, 106688−106694.
(46) Biedenbänder, T.; Aladin, V.; Saeidpour, S.; Corzilius, B. Dynamic Nuclear Polarization for Sensitivity Enhancement in Biomolecular Solid-State NMR. *Chem. Rev.* **2022**, *122*, 9738−9794.
(47) Aladin, V.; Sreemantula, A. K.; Biedenbänder, T.; Marchanka, A.; Corzilius, B. Specific Signal Enhancement on an RNA-Protein Interface by Dynamic Nuclear Polarization. *Chem.—Eur. J.* **2023**, *29*, e202203443−e202203454.
(48) Biedenbänder, T.; de Jesus, V.; Schmidt-Dengler, M.; Helm, M.; Corzilius, B.; Fürtig, B. RNA Modifications Stabilize the Tertiary Structure of tRNAfMet by Locally Increasing Conformational Dynamics. *Nucleic Acids Res.* **2022**, *50*, 2334−2349.
(49) Döller, S. C.; Gutmann, T.; Hoffmann, M.; Buntkowsky, G. A Case Study on the Influence of Hydrophilicity on the Signal Enhancement by Dynamic Nuclear Polarization. *Solid State Nucl. Magn. Reson.* **2022**, *122*, 101829−101837.
(50) Hoffmann, M. M.; Bothe, S.; Brodrecht, M.; Klimavicius, V.; Haro-Mares, N. B.; Gutmann, T.; Buntkowsky, G. Direct and Indirect Dynamic Nuclear Polarization Transfer Observed in Mesoporous Materials Impregnated with Nonionic Surfactant Solutions of Polar Polarizing Agents. *J. Phys. Chem. C* **2020**, *124*, 5145−5156.
(51) Sauvée, C.; Rosay, M.; Casano, G.; Aussenac, F.; Weber, R. T.; Ouari, O.; Tordo, P. Highly Efficient, Water-Soluble Polarizing Agents for Dynamic Nuclear Polarization at High Frequency. *Angew. Chem., Int. Ed.* **2013**, *52*, 10858−10861.
(52) Brodrecht, M.; Breitzke, H.; Gutmann, T.; Buntkowsky, G. Biofunctionalization of Nano Channels by Direct In-Pore Solid-Phase Peptide Synthesis. *Chem.—Eur. J.* **2018**, *24*, 17814−17822.
(53) Wang, X.; Lin, K. S. K.; Chan, J. C. C.; Cheng, S. Direct Synthesis and Catalytic Applications of Ordered Large Pore Aminopropyl-Functionalized SBA-15 Mesoporous Materials. *J. Phys. Chem. B* **2005**, *109*, 1763−1769.
(54) Brunauer, S.; Emmett, P. H.; Teller, E. Adsorption of Gases in Multimolecular Layers. *J. Am. Chem. Soc.* **1938**, *60*, 309−319.
(55) Klyachko-Gurvich, A. L. An Improved Method of Determining Surface Area by the Adsorption of Air. *Russ. Chem. Bull.* **1961**, *10*, 1756−1758.
(56) Barrett, E. P.; Joyner, L. G.; Halenda, P. P. The Determination of Pore Volume and Area Distributions in Porous Substances. I. Computations from Nitrogen Isotherms. *J. Am. Chem. Soc.* **1951**, *73*, 373−380.
(57) Ravikovitch, P. I.; Haller, G. L.; Neimark, A. V. Density Functional Theory Model for Calculating Pore Size Distributions: Pore Structure of Nanoporous Catalysts. *Adv. Colloid Interface Sci.* **1998**, *76*−*77*, 203−226.
(58) Schneider, S.; Säckel, C.; Brodrecht, M.; Breitzke, H.; Buntkowsky, G.; Vogel, M. NMR Studies on the Influence of Silica Confinements on Local and Diffusive Dynamics in LiCl Aqueous Solutions Approaching their Glass Transitions. *J. Chem. Phys.* **2020**, *153*, 244501−244513.
(59) Kirschenbaum, L. J.; Riesz, P. Sonochemical Degradation of Cyclic Nitroxides in Aqueous Solution. *Ultrason. Sonochem.* **2012**, *19*, 1114−1119.
(60) Fung, B. M.; Khitrin, A. K.; Ermolaev, K. An Improved Broadband Decoupling Sequence for Liquid Crystals and Solids. *J. Magn. Reson.* **2000**, *142*, 97−101.
(61) Kruk, M.; Jaroniec, M.; Ko, C. H.; Ryoo, R. Characterization of the Porous Structure of SBA-15. *Chem. Mater.* **2000**, *12*, 1961−1968.
(62) Janus, R.; Wądrzyk, M.; Lewandowski, M.; Natkański, P.; Łątka, P.; Kuśtrowski, P. Understanding Porous Structure of SBA-15 upon Pseudomorphic Transformation into MCM-41: Non-Direct Investigation by Carbon Replication. *J. Ind. Eng. Chem.* **2020**, *92*, 131−144.
(63) Matos, J. R.; Mercuri, L. P.; Kruk, M.; Jaroniec, M. Toward the Synthesis of Extra-Large-Pore MCM-41 Analogues. *Chem. Mater.* **2001**, *13*, 1726−1731.
(64) Drach, M.; Narkiewicz-Michałek, J.; Rudziński, W.; Findenegg, G. H.; Király, Z. Calorimetric Study of Adsorption of Non-Ionic Surfactants on Silica Gels: Estimating the Role of Lateral Interactions Between Surface Aggregates. *Phys. Chem. Chem. Phys.* **2002**, *4*, 2307−2319.
(65) Hoffmann, M. M.; Too, M. D.; Paddock, N. A.; Horstmann, R.; Kloth, S.; Vogel, M.; Buntkowsky, G. On the Behavior of the Ethylene Glycol Components of Polydisperse Polyethylene Glycol PEG 200. *J. Phys. Chem. B* **2023**, *127*, 1178−1196.
(66) Kawai, S.; Foster, A. S.; Björkman, T.; Nowakowska, S.; Björk, J.; Canova, F. F.; Gade, L. H.; Jung, T. A.; Meyer, E. Van der Waals Interactions and the Limits of Isolated Atom Models at Interfaces. *Nat. Commun.* **2016**, *7*, 11559−11565.
(67) Margenau, H. Van der Waals Forces. *Rev. Mod. Phys.* **1939**, *11*, 1−35.
(68) Schauperl, M.; Podewitz, M.; Waldner, B. J.; Liedl, K. R. Enthalpic and Entropic Contributions to Hydrophobicity. *J. Chem. Theory Comput.* **2016**, *12*, 4600−4610.
(69) Dohmen, M. P. J.; Pereira, A. M.; Timmer, J. M. K.; Benes, N. E.; Keurentjes, J. T. F. Hydrodynamic Radii of Polyethylene Glycols in Different Solvents Determined from Viscosity Measurements. *J. Chem. Eng. Data* **2008**, *53*, 63−65.
(70) Linegar, K. L.; Adeniran, A. E.; Kostko, A. F.; Anisimov, M. A. Hydrodynamic Radius of Polyethylene Glycol in Solution Obtained by Dynamic Light Scattering. *Colloid J.* **2010**, *72*, 279−281.
(71) Macdonald, P. M.; Soong, R. The Truncated Driven NOE and ^{13}C NMR Sensitivity Enhancement in Magnetically-Aligned Bicelles. *J. Magn. Reson.* **2007**, *188*, 1−9.
(72) Mao, J.; Aladin, V.; Jin, X.; Leeder, A. J.; Brown, L. J.; Brown, R. C. D.; He, X.; Corzilius, B.; Glaubitz, C. Exploring Protein Structures by DNP-Enhanced Methyl Solid-State NMR Spectroscopy. *J. Am. Chem. Soc.* **2019**, *141*, 19888−19901.
(73) Lilly Thankamony, A. S.; Wittmann, J. J.; Kaushik, M.; Corzilius, B. Dynamic Nuclear Polarization for Sensitivity Enhancement in Modern Solid-State NMR. *Prog. Nucl. Magn. Reson. Spectrosc.* **2017**, *102*−*103*, 120−195.
(74) Luo, X.-L.; Howard, J. A. K.; Crabtree, R. H. ^{1}H NMR T_1(min) Data and Structure in a Series of Rhenium Polyhydride Complexes and the Contribution of M-H Dipole-Dipole Relaxation. *Org. Magn. Reson.* **1991**, *29*, S89−S93.
(75) Jarymowycz, V. A.; Stone, M. J. Fast Time Scale Dynamics of Protein Backbones: NMR Relaxation Methods, Applications, and Functional Consequences. *Chem. Rev.* **2006**, *106*, 1624−1671.

https://doi.org/10.1021/acs.jpcc.3c01946
J. Phys. Chem. C 2023, 127, 12125−12134

Direct and indirect DNP NMR uncovers the interplay of surfactants with their mesoporous host material

Supporting Information

*Sonja C. Döller,[a] Martin Brodrecht,[a] Torsten Gutmann,[a] Markus Hoffmann,[b] Gerd Buntkowsky[a]**

a) Technical University of Darmstadt, Department of Chemistry, Eduard-Zintl-Institute for Inorganic and Physical Chemistry, Peter-Grünberg-Straße 8, 64287 Darmstadt, Germany

b) Department of Chemistry and Biochemistry, State University of New York College at Brockport, Brockport, NY, 14420, USA

1. Details on utilized chemicals

Table S1. Summary of the average structural composition of the polydisperse surfactants investigated in this work.[1]

Sample	PEG 200	$C_{10}E_6$		Triton X-100
		C_x	E_n	
Average length	4.13	10.03	6.27	8.62

Table S2. Details on all chemicals utilized in this report.[1]

Chemical	CAS Nr.	Source	Mass fraction purity
Water	7732-18-5	VWR	> 0.99[a]
Tetraethyl orthosilicate	78-10-4	ACROS Organics	0.98
Ammonia solution (25 %)	1336-21-6	Carl Roth	Ph. Eur.[b]
Pluronic P123	9003-11-6	Sigma-Aldrich	not applicable[c]
HCl (37.0 %)	7647-01-0	Carl Roth	36.5-38.0 %
E_5	4792-15-8	Alfa Aesar	> 98 %
PEG 200[d]	25322-68-3	Dow Chemical Company	not applicable
$C_{10}E_6$[e]	68439-46-3	Air Products	not applicable
Triton X-100[f]	9002-93-1	Dow Chemical Company	not applicable

[a] HiPerSolv CHROMANORM for HPLC - super gradient grade
[b] Ph. Eur. according to Carl Roth 25,0 - 27,0 %
[c] Average Mn ~5,800; PEG, composition: 30 wt%; feed ratio: 20:70:20 (EO:PO:EO)
[d] Polyethylene glycol, vendor specifies < 4 % diethylene and 1 % ethylene glycol by mass
[e] alcohols, C_9-C_{11}, ethoxylated
[f] Polyethylene glycol octylphenyl ether, vendor specifies < 3 % polyethylene oxide by mass

2. Pore size distribution for SBA-15 obtained by NLDFT

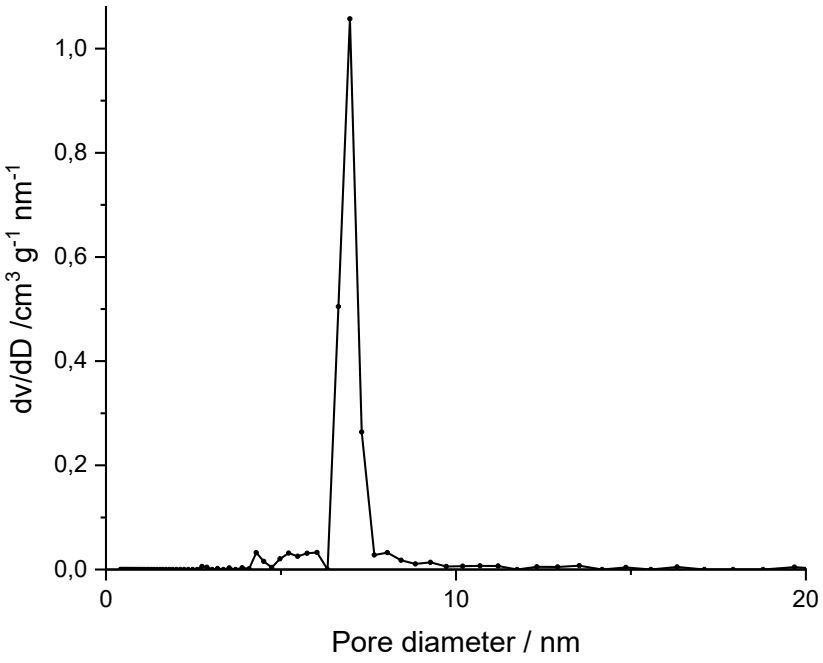

Figure S1. Pore distribution obtained by NLDFT for the utilized SBA-15.

3. Differential Scanning Calorimetry (DSC) Data

Confining a molecule has been shown to significantly alter its phase behavior, strongly influencing crystallization and melting as well as dynamic processes.[2–4] To inspect these processes, DSC measurements were conducted. Figure S2 displays the heating and cooling curves for AMUPol dissolved in the surfactants as well as those for the surfactants confined in SBA-15 and MCM 41.

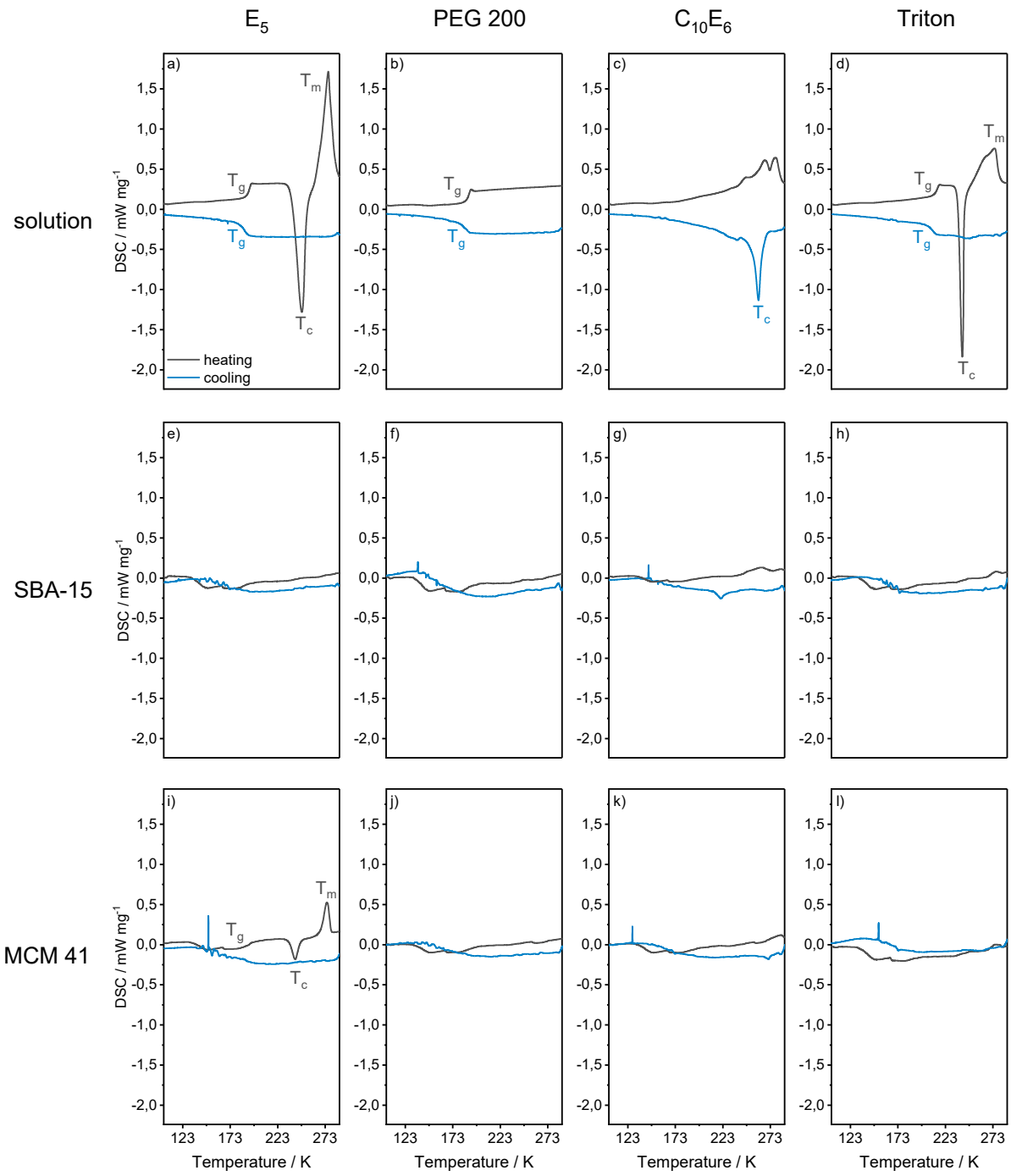

Figure S2. DSC heating and cooling curves of AMUPol dissolved in the surfactants (solution) as well as the surfactants confined in SBA-15 and MCM 41 for a heating rate of 10 K min^{-1}. Glass transitions (T_g) as well as crystallization (T_c) and melting points (T_m) are labelled.

Due to the small amount of sample which can be applied in the DSC crucible, the DSC curves for the surfactants confined in the mesoporous materials show little signal intensity in

Figure S2e – f. However, it is still possible to compare their general shape to those of the AMUPol dissolved in the bulk surfactants (hereinafter referred to as solution) shown in Figure S2a – d. The recorded DSC curves show a significantly different behavior for all surfactants once they were confined in the mesoporous silica materials. For the solution of E_5, an exo- as well as an endothermic peak at 248 K (crystallization after glass transition) and 276 K (melting point) respectively and a glass transition at approximately 193 K can be observed in Figure S2a for the heating procedure. For the cooling procedure, only the glass transition is observable. These features are not at all observable for the E_5 confined in SBA-15 (compare Figure S2e). For E_5 in MCM 41, these features are observable for the heating procedure in Figure S2i, but they are shifted to lower temperatures (286 K for the endothermic and 275 °C for the exothermic peak). Additionally, the glass transition is broadened, indicating at least some form of interaction between the silica material and the surfactant.

The PEG 200 solution does not crystallize while cooling but rather forms a glass, which is indicated by the pronounced glass transition observable in the corresponding DSC curve in Figure S2b at approximately 193 K. This distinct glass transition signal cannot be observed in the DSC curves for the confined surfactant where only broad features are present in Figure S2f and j.

The DSC data in Figure S2c for the $C_{10}E_6$ solution shows an exothermic signal at 260 K for the cooling procedure, which indicates a crystallization process. This signal undergoes a shift to 221 K and is significantly broadened for the surfactant confined in SBA-15 (Figure S2g). The features of the heating curve are also broadened. For the DSC curve in Figure S2k obtained for MCM 41 impregnated with $C_{10}E_6$, a broad exothermic signal is observed at 267 K for the cooling curve. The features of the corresponding heating curve are all significantly broadened.

The DSC curve in Figure S2d for the Triton solution displays a distinct glass transition at approximately 213 K and an exothermic signal at 238 K, again referring to a crystallization

process. None of these features are observable for the DSC curves of the confined Triton in Figure h and l, where the observed features are so broad that they become indeterminable.

The changes of the DSC curves displayed in Figure S2e – l of the surfactants confined in the mesoporous silica materials compared to those from the surfactant solutions shown in Figure S2a – d indicate an altered response of the confined surfactants to temperature changes, which in turn indicates interactions of the surfactants with the SBA-15 and MCM 41 surfaces. Therefore, it can be safely assumed that the majority of the surfactant molecules are absorbed inside the pores of the mesoporous silica materials.

4. $^{1}H \rightarrow {}^{13}C$ CP MAS DNP experiments

To estimate enhancement factors for all samples, $^{1}H \rightarrow {}^{13}C$ CP MAS DNP experiments were performed. The corresponding spectra of all surfactants confined in the two mesoporous silica materials are displayed in Figure S3. Table S3 summarizes the obtained enhancement factors.

Table S3. Surfactants used in this work and obtained enhancement factors for both silica materials and the corresponding errors, determined from the $^{1}H \rightarrow {}^{13}C$ CP MAS DNP experiments.

Material	E_5	PEG 200	$C_{10}E_6$	Triton
SBA-15	81 ± 2	46 ± 4	26 ± 1	38 ± 1
MCM 41	37 ± 1	33 ± 1	19 ± 1	21 ± 2

From the enhancement factors presented in Table S3, a general trend can be described. For all surfactants, the enhancement factors are larger in SBA-15 than in MCM 41. The larger pore size of the SBA-15 material might lead to more molecules being absorbed into each pore, therefore forming a larger proton reservoir and allowing the polarization to spread more evenly. This hypothesis could be underlined utilizing experiments investigating the proton dipolar

coupling or by measuring the buildup in $^{1}H \rightarrow {}^{13}C$ CP MAS DNP spectra. As the optimizing of the enhancement is not the main goal of this work and the enhancement factors are not of interest for the analysis of the data, such experiments are out of the scope of this work.

The largest enhancement can be observed for E_5 confined in SBA-15, with an enhancement of 81. This leads to a time saving factor of circa 6600. This means that, to acquire the data with a similar signal-to-noise ratio as the one present in the DNP NMR spectra ($t_{exp} \approx 34$ min), a measurement time of approximately 160 days would be necessary. The smallest enhancement factor, $\varepsilon = 19$, still leads to a time saving factor of circa 400 ($t_{exp} \approx 34$ min *versus* $t_{exp} \approx 9$ d).

In $^{1}H \rightarrow {}^{13}C$ CP MAS DNP experiments, μw irradiation is utilized to transfer the significantly higher spin polarization of unpaired electrons to the surrounding hydrogen nuclei *via* the solid effect or cross effect. This polarization then spreads through the proton reservoir of the sample *via* homonuclear ^{1}H-^{1}H spin diffusion before being transferred to the carbon nuclei through cross polarization.[5–10] In case of homogeneous ^{1}H-^{1}H spin diffusion nearly the same enhancements for all signals are obtained, which is desirable in regular DNP NMR.

However, these CP MAS experiments do not allow the investigation of interactions of the surfactant molecules with the polarizing agent or with their surroundings. Therefore, direct polarization ^{13}C MAS DNP spectra were recorded in this study.

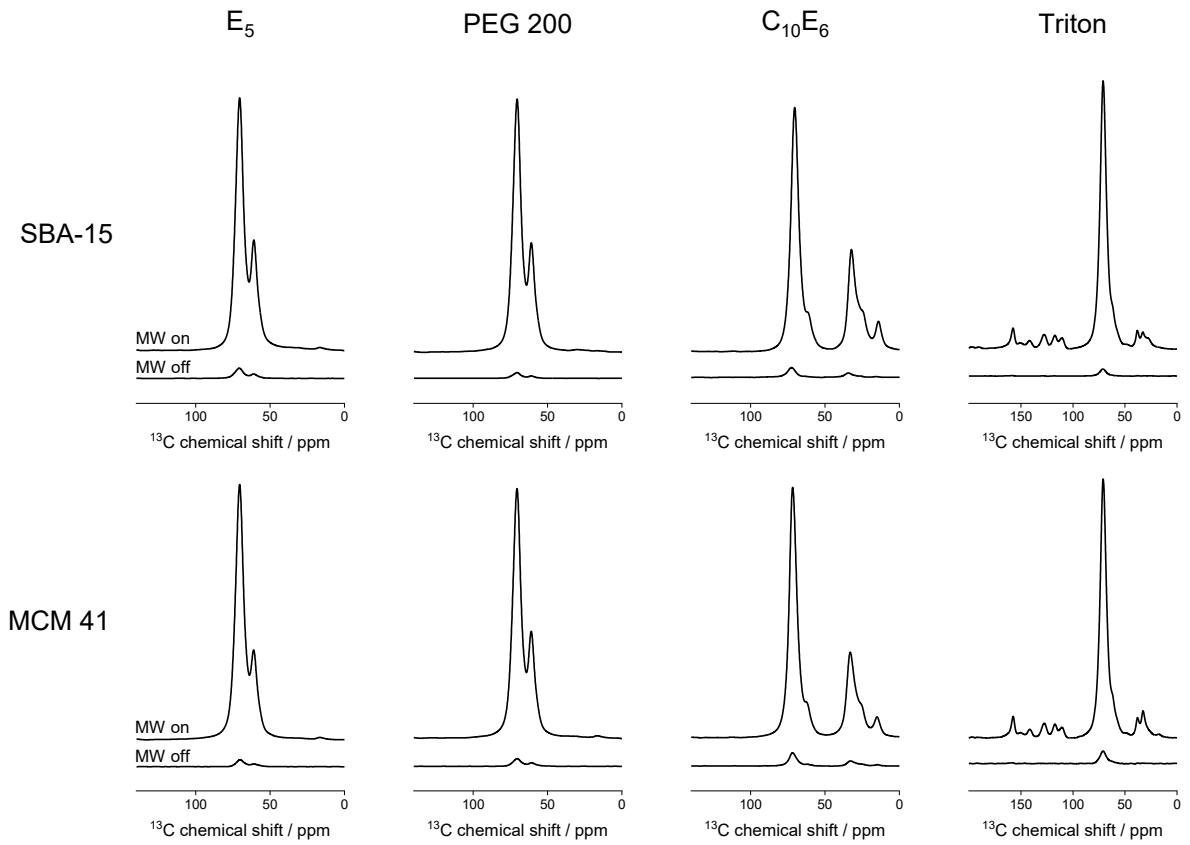

Figure S3. Overview of the μw off and μw on $^{1}H \rightarrow {}^{13}C$ CP MAS ssNMR spectra of all samples recorded in this work.

5. Deconvolution of the signals

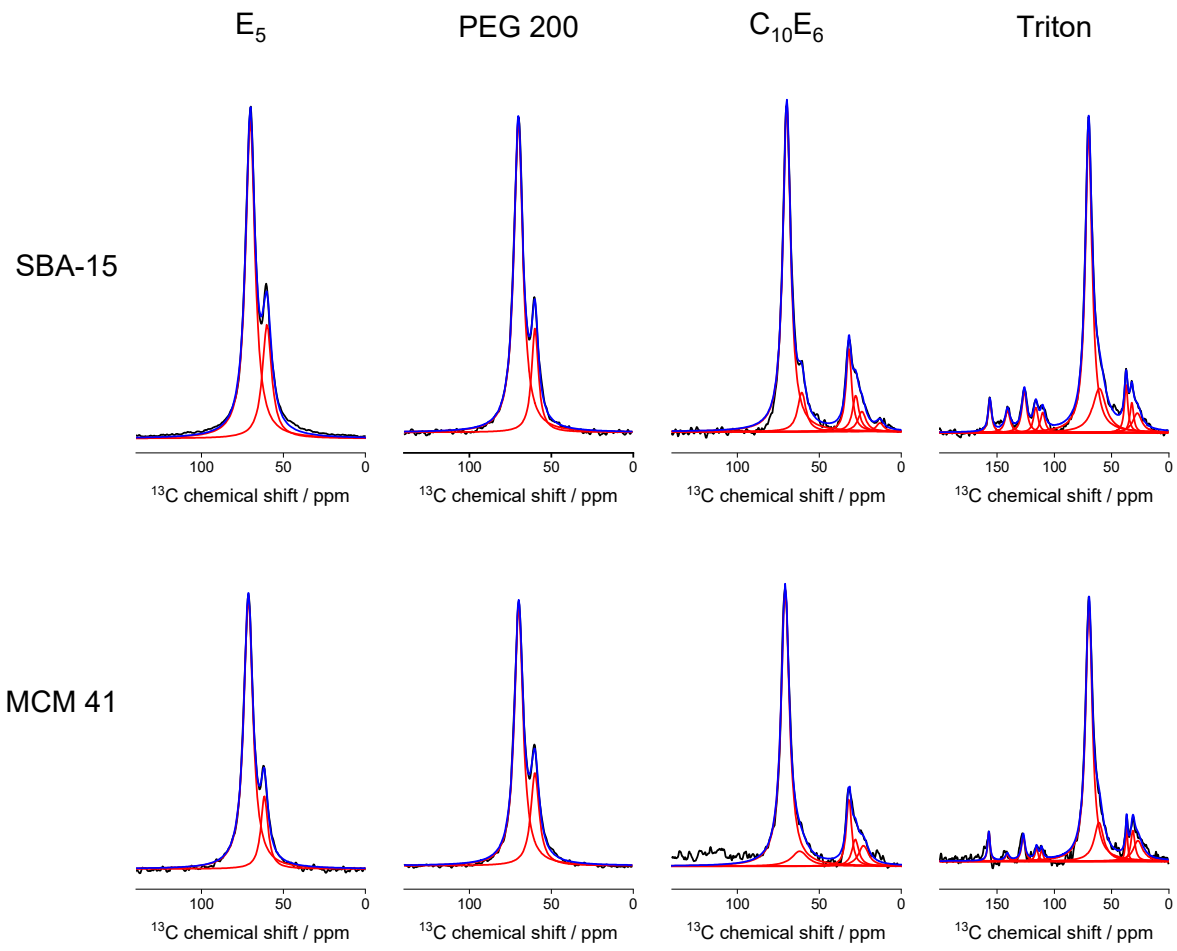

Figure S4. Deconvolution of the signals, exemplary shown for the direct signals at 1400 s buildup time. The signals of all other spectra, including the indirect spectra, were deconvoluted in the same manner. Black: experimental data, red: individual Lorentzian signals, blue: overall fit.

6. Buildup curves

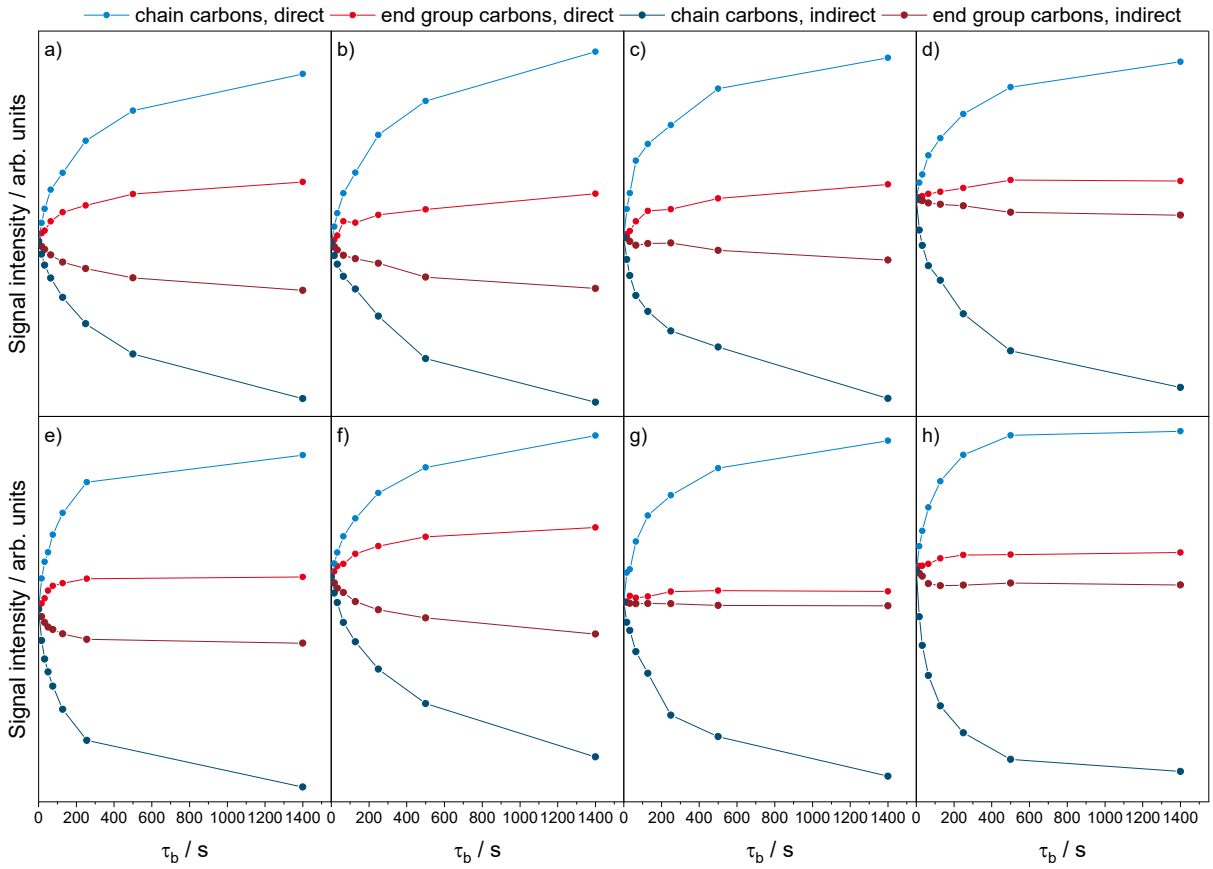

Figure S5. Individual buildup curves for all investigated samples. E_5, PEG 200, $C_{10}E_6$ and Triton in SBA-15 (a-d) and MCM 41 (e-h), respectively.

7. DNP enhanced $^{1}H \rightarrow {}^{29}Si$ FSLG HETCOR Spectra

DNP enhanced $^{1}H \rightarrow {}^{29}Si$ FSLG HETCOR spectra were acquired at 8 kHz spinning rate and referenced according to the literature utilizing the corresponding 2D $^{1}H \rightarrow {}^{1}H$ MAS frequency switched Lee-Goldburg (FSLG) spectra.[11,12] 64 slices with 128 scans for each slice were acquired, using a recycle delay of 3 s. Heteronuclear tppm15[13] decoupling was applied during data acquisition while homonuclear FSLG decoupling[14] employing a decoupling field of 100 kHz was used during the evolution of the chemical shift. Contact times of 3 ms and 7 ms were used.

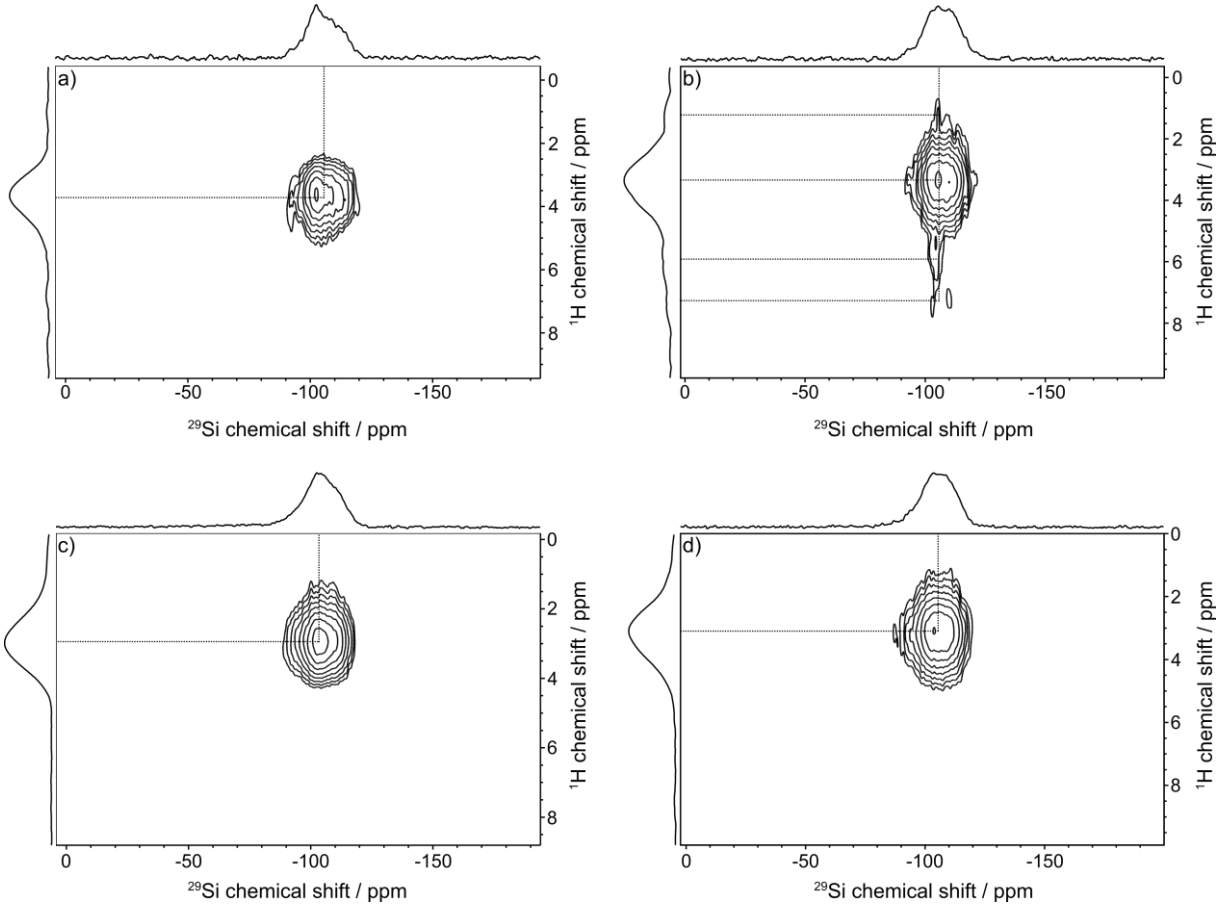

Figure S6. Exemplary DNP enhanced $^{1}H \rightarrow {}^{29}Si$ FSLG HETCOR spectra of Triton X-100 in MCM 41 (a and b) and E_5 in MCM 41 (c and d). Spectra a and d were acquired with 3 ms contact time to observe short and intermediate correlations, while spectra b and d were acquired with 7 ms contact time for the observation of long-range correlations.

For Triton X-100, only the correlation of the ethylene glycol units with the silicon nuclei at a proton chemical shift of 3.6 ppm and a ^{29}Si chemical shift of -100.9 ppm (peak center) is visible in the spectrum acquired with the short contact time (Figure S6a). In the spectrum with the long contact time (Figure S6b), additional correlations are observed. These correlations occur at the approximate ^{1}H/^{29}Si chemical shift values of 1.3 ppm/-103.8 ppm, 6.1 ppm/-102.2 ppm and 7.5/-103.8 ppm, leading us to assign the high field signal to the aliphatic and the low field signals to the aromatic moieties of the Triton X-100 molecule. Since these correlations are not observed at a short contact time, a spatial proximity of the aliphatic/aromatic moieties of the Triton X-100 molecule to the silica surface is unlikely, therefore strengthening the argument towards the model arrangement showcased in the manuscript.

As a comparison, spectra of E_5 in MCM 41 were acquired (Figure S6b and c). These spectra only show a single correlation between the ethylene glycol protons and the silicon nuclei at 3.2 ppm/103.0 ppm. This correlation does not change significantly as the contact time is varied, implying that all nuclei have a similar proximity to the silica surface.

As the ^{1}H $\rightarrow$ ^{29}Si FSLG HETCOR spectra are not the main focus of this work, it was not attempted to resolve the individual correlations of the surfactant protons to the different kinds of silica groups (Q_1 – Q_4).

8. References

(1) Hoffmann, M. M.; Bothe, S.; Gutmann, T.; Hartmann, F.-F.; Reggelin, M.; Buntkowsky, G. Directly vs. Indirectly Enhanced ^{13}C in Dynamic Nuclear Polarization Magic Angle Spinning NMR Experiments of Nonionic Surfactant Systems. *J. Phys. Chem. C* **2017**, *121*, 2418–2427.

(2) Döller, S. C.; Brodrecht, M.; Haro Mares, N. B.; Breitzke, H.; Gutmann, T.; Hoffmann, M.; Buntkowsky, G. Deuterium NMR Studies of the Solid–Liquid Phase Transition of Octanol-d_{17} Confined in SBA-15. *J. Phys. Chem. C* **2021**, *125*, 25155–25164.

(3) Buntkowsky, G.; Döller, S. C.; Haro-Mares, N.; Gutmann, T.; Hoffmann, M. Solid-State NMR Studies of Non-Ionic Surfactants Confined in Mesoporous Silica. *Z. Phys. Chem.* **2022**, *236*, 939–960.

(4) Buntkowsky, G.; Vogel, M. Small Molecules, Non-Covalent Interactions, and Confinement. *Molecules* **2020**, *25*, 3311-3342.
(5) Barnes, A. B.; Paëpe, G. de; van der Wel, P. C. A.; Hu, K.-N.; Joo, C.-G.; Bajaj, V. S.; Mak-Jurkauskas, M. L.; Sirigiri, J. R.; Herzfeld, J.; Temkin, R. J. et al. High-Field Dynamic Nuclear Polarization for Solid and Solution Biological NMR. *Appl. Magn. Reson.* **2008**, *34*, 237–263.
(6) Pines, A.; Gibby, M. G.; Waugh, J. S. Proton-Enhanced Nuclear Induction Spectroscopy. A Method for High Resolution NMR of Dilute Spins in Solids. *J. Chem. Phys.* **1972**, *56*, 1776–1777.
(7) Hovav, Y.; Feintuch, A.; Vega, S. Theoretical aspects of Dynamic Nuclear Polarization in the Solid State - the Cross Effect. *J. Magn. Reson.* **2012**, *214*, 29–41.
(8) Lilly Thankamony, A. S.; Wittmann, J. J.; Kaushik, M.; Corzilius, B. Dynamic Nuclear Polarization for Sensitivity Enhancement in Modern Solid-State NMR. *Prog. Nucl. Magn. Reson. Spectrosc.* **2017**, *102-103*, 120–195.
(9) Rossini, A. J.; Zagdoun, A.; Hegner, F.; Schwarzwälder, M.; Gajan, D.; Copéret, C.; Lesage, A.; Emsley, L. Dynamic Nuclear Polarization NMR Spectroscopy of Microcrystalline Solids. *J. Am. Chem. Soc.* **2012**, *134*, 16899–16908.
(10) Pinon, A. C.; Schlagnitweit, J.; Berruyer, P.; Rossini, A. J.; Lelli, M.; Socie, E.; Tang, M.; Pham, T.; Lesage, A.; Schantz, S. et al. Measuring Nano- to Microstructures from Relayed Dynamic Nuclear Polarization NMR. *J. Phys. Chem. C* **2017**, *121*, 15993–16005.
(11) Kumari, B.; Brodrecht, M.; Breitzke, H.; Werner, M.; Grünberg, B.; Limbach, H.-H.; Forg, S.; Sanjon, E. P.; Drossel, B.; Gutmann, T. et al. Mixtures of Alcohols and Water confined in Mesoporous Silica: A Combined Solid-State NMR and Molecular Dynamics Simulation Study. *J. Phys. Chem. C* **2018**, *122*, 19540–19550.
(12) Kumari, B.; Brodrecht, M.; Gutmann, T.; Breitzke, H.; Buntkowsky, G. Efficient Referencing of FSLG CPMAS HETCOR Spectra Using 2D ^{1}H–^{1}H MAS FSLG. *Appl. Magn. Reson.* **2019**, *50*, 1399–1407.
(13) Bennett, A. E.; Rienstra, C. M.; Auger, M.; Lakshmi, K. V.; Griffin, R. G. Heteronuclear Decoupling in Rotating Solids. *J. Chem. Phys.* **1995**, *103*, 6951–6958.
(14) van Rossum, B.-J.; Förster, H.; Groot, H. de. High-Field and High-Speed CP-MAS 13C NMR Heteronuclear Dipolar-Correlation Spectroscopy of Solids with Frequency-Switched Lee–Goldburg Homonuclear Decoupling. *J. Mag. Res.* **1997**, *124*, 516–519.

5 Conclusion and Outlook

The present work utilizes two different methods, deuterium as well as DNP enhanced ssNMR spectroscopy, in order to elucidate molecular arrangements in bulk as well as at the solid-liquid interface. For this purpose, systems relevant for the sustainable transformation of chemistry (according to the twelve principles of Green Chemistry) were investigated.

Through the application of deuterium ssNMR spectroscopy, the arrangement of *n*-octanol-d_{17} within the pores of the mesoporous silica material SBA-15 was determined. By varying the temperature of the sample, the melting behavior of the *n*-octanol-d_{17} was studied. It was shown that, despite the confinement, the formation of a true glass is unlikely. Instead, the *n*-octanol-d_{17} forms small crystallites, each with an individual, size-dependent melting temperature and therefore melting activation energy.

This approach can be expanded to more complex systems. Especially the synthesis and ^{2}H ssNMR investigation of selectively labeled surfactants would be of considerable interest. These kind of measurements could provide new insights into the dynamics of different moieties of the surfactants. It was shown that PEG, $C_{10}E_6$ and Triton display dynamics even at cryogenic temperatures and in confinement, yet the determination of the actual motion taking place has not yet been carried out. By regioselective deuteration of the analyte molecules at different positions and by subsequent observation of the activation of the various degrees of freedom in the process of thawing, this might be feasible.

In addition, the deuterium ssNMR studies were carried out on blank SBA-15 although the process of immobilizing a catalyst usually requires the functionalization of the silica surface.[36] As this changes the surface characteristics significantly, the interactions of the solvent with the surface are expected to change as well. Preliminary studies carried out in this work have already shown a significant change in melting behavior for *n*-octanol-d_{17} confined in functionalized pores compared to blank ones. Still, more work is necessary to interpret the obtained complicated spectral shape. A cooperation with another research group for the purpose of conducting the necessary MD simulations has already been formed.

To further understand the interplay of PAs with analyte molecules, studies of four different, commercially available organic nitroxide radicals dissolved in *n*-octanol were carried out. In this context, a novel approach of analyzing data obtained from direct/indirect DNP enhanced NMR experiments was developed and successfully applied to illustrate the manner in which polarization travels through the sample, shedding light on how the PAs interact with the amphiphilic *n*-octanol. This work highlights the importance of

carefully choosing the PA for DNP enhanced ssNMR experiments for samples where the formation of supramolecular structures is conceivable.

Likewise, direct/indirect DNP enhanced ssNMR spectroscopy was employed to elucidate the arrangement of surfactants as well as PEGs in mesoporous host materials. Detailed information on the way the analyte molecules interact with the present silica surface was obtained by utilizing the novel method developed in the previous study, omitting the need to account for sample-specific qualities and enabling a quantitative analysis of the data which was not possible previously. From the NMR data, a detailed model of the analyte molecules' arrangement was derived which was confirmed by two-dimensional NMR spectroscopy in a later step.

The results of this work provide valuable insights into the interplay of surfactants and PEGs with each other as well as into their behavior at solid-liquid interfaces. Based on the present findings, it is possible to better understand the interactions of solvent molecules with solid support materials of immobilized catalysts, thereby enabling the potential rational design of catalytically active systems. Since the novel method of data analysis for spectra obtained in direct/indirect DNP enhanced ssNMR experiments herein established is universally applicable for a multitude of systems, it is expected to become an important tool in illustrating the interactions taking place in these systems.

Potential further applications lay in the choice of the investigated solid support material as well as of the surfactant. As support material, other solids with high inner surface areas like zeolites, metal-organic frameworks or polymer-based systems are suitable candidates. As surfactants, molecules from renewable sources ought to be considered in order to eliminate petroleum-based chemicals and stay within the framework of the twelve principles of Green Chemistry. Appropriate steps towards the development of such surfactants have already been undertaken.[17] Furthermore, covalently attaching a PA to the wall of a solid support material, as previously demonstrated,[214] could further enhance the investigations presented herein. As immobilized catalysts usually feature a linker moiety tethering them to the silica wall, such systems resemble actual catalyst systems more closely. Through the application of the newly developed analytical approach, it might be possible to follow the polarization from the PA attached to the pore wall to the analyte molecule, therefore directly illustrating which moiety of the analyte molecule governs the relevant interactions.

Bibliography

[1] J. B. Zimmerman, P. T. Anastas, H. C. Erythropel, W. Leitner, *Science* **2020**, *367*, 397–400.

[2] P. T. Anastas, J. C. Warner, *Green Chemistry: Theory and Practice*, Oxford University Press, Oxford, **1998**.

[3] D. J. C. Constable, C. Jimenez-Gonzalez, R. K. Henderson, *Org. Process Res. Dev.* **2007**, *11*, 133–137.

[4] D. Reinhardt, F. Ilgen, D. Kralisch, B. König, G. Kreisel, *Green Chem.* **2008**, *10*, 1170–1181.

[5] C. J. Clarke, W.-C. Tu, O. Levers, A. Bröhl, J. P. Hallett, *Chem. Rev.* **2018**, *118*, 747–800.

[6] L. Lajoie, A.-S. Fabiano-Tixier, F. Chemat, *Pharmaceuticals* **2022**, *15*, 1–22.

[7] A. Zdziennicka, J. Krawczyk, K. Szymczyk, B. Jańczuk, *Int. J. Mol. Sci.* **2018**, *19*, 1–18.

[8] N. A. Isley, R. T. H. Linstadt, S. M. Kelly, F. Gallou, B. H. Lipshutz, *Org. Lett.* **2015**, *17*, 4734–4737.

[9] B. H. Lipshutz, T. B. Petersen, A. R. Abela, *Org. Lett.* **2008**, *10*, 1333–1336.

[10] P. Klumphu, B. H. Lipshutz, *J. Org. Chem.* **2014**, *79*, 888–900.

[11] B. H. Lipshutz, N. A. Isley, J. C. Fennewald, E. D. Slack, *Angew. Chem. Int. Ed.* **2013**, *52*, 10952–10958.

[12] B. H. Lipshutz, G. T. Aguinaldo, S. Ghorai, K. Voigtritter, *Org. Lett.* **2008**, *10*, 1325–1328.

[13] B. H. Lipshutz, S. Ghorai, *Tetrahedron* **2010**, *66*, 1057–1063.

[14] B. H. Lipshutz, S. Ghorai, *Org. Lett.* **2012**, *14*, 422–425.

[15] F. Gallou, P. Guo, M. Parmentier, J. Zhou, *Org. Process Res. Dev.* **2016**, *20*, 1388–1391.

[16] C. M. Gabriel, M. Keener, F. Gallou, B. H. Lipshutz, *Org. Lett.* **2015**, *17*, 3968–3971.

[17] V. S. Nagtode, C. Cardoza, H. K. A. Yasin, S. N. Mali, S. M. Tambe, P. Roy, K. Singh, A. Goel, P. D. Amin, B. R. Thorat, J. N. Cruz, A. P. Pratap, *ACS Omega* **2023**, *8*, 11674–11699.

[18] J. Chen, S. K. Spear, J. G. Huddleston, R. D. Rogers, *Green Chem.* **2005**, *7*, 64–82.

[19] B. Sauvagnat, F. Lamaty, R. Lazaro, J. Martinez, *C. R. Acad. Sci. Paris* **1998**, *1*, 777–780.

[20] J. Soni, N. Sahiba, A. Sethiya, S. Agarwal, *J. Mol. Liq.* **2020**, *315*, 113766–113797.

[21] E. Santaniello, A. Manzocchi, P. Sozzani, *Tetrahedron Lett.* **1979**, *20*, 4581–4582.

[22] P. W. McGarvey, M. M. Hoffmann, *Tenside Surfactants Deterg.* **2018**, *55*, 203–209.

[23] N. F. Leininger, J. L. Gainer, D. J. Kirwan, *AlChE J.* **2004**, *50*, 511–517.

[24] D. Badone, G. Jommi, R. Pagliarin, P. Tavecchia, *Synthesis* **1987**, *1987*, 920–921.

[25] N. Suzuki, T. Azuma, Y. Kaneko, Y. Izawa, H. Tomioka, T. Nomoto, *J. Chem. Soc. Perkin Trans. 1* **1987**, 645–647.

[26] M. Pires, S. Purificação, A. Santos, M. Marques, *Synthesis* **2017**, *49*, 2337–2350.

[27] A. Haimov, R. Neumann, *Chem. Commun.* **2002**, 876–877.

[28] E. Santaniello, A. Fiecchi, A. Manzocchi, P. Ferraboschi, *J. Org. Chem.* **1983**, *48*, 3074–3077.

[29] D. J. Heldebrant, P. G. Jessop, *J. Am. Chem. Soc.* **2003**, *125*, 5600–5601.

[30] R. A. Sheldon, *Chem. Soc. Rev.* **2012**, *41*, 1437–1451.

[31] L. Rösler, M. V. Höfler, H. Breitzke, T. Wissel, K. Herr, H. Heise, T. Gutmann, G. Buntkowsky, *Cellulose* **2022**, *29*, 6283–6299.

[32] H. M. L. Davies, A. M. Walji, T. Nagashima, *J. Am. Chem. Soc.* **2004**, *126*, 4271–4280.

[33] H. M. Hultman, M. de Lang, M. Nowotny, I. W. Arends, U. Hanefeld, R. A. Sheldon, T. Maschmeyer, *J. Catal.* **2003**, *217*, 264–274.

[34] J. Liu, Y. Xu, P. B. Groszewicz, M. Brodrecht, C. Fasel, K. Hofmann, X. Tan, T. Gutmann, G. Buntkowsky, *Catal. Sci. Technol.* **2018**, *8*, 5190–5200.

[35] F. G. Adly, A. Ghanem, *Tetrahedron Lett.* **2016**, *57*, 852–857.

[36] P. Verma, Y. Kuwahara, K. Mori, R. Raja, H. Yamashita, *Nanoscale* **2020**, *12*, 11333–11363.

[37] M. Brodrecht, H. Breitzke, T. Gutmann, G. Buntkowsky, *Chem. Eur. J.* **2018**, *24*, 17814–17822.

[38] P. S. Shinde, P. S. Suryawanshi, K. K. Patil, V. M. Belekar, S. A. Sankpal, S. D. Delekar, S. A. Jadhav, *J. Compos. Sci.* **2021**, *5*, 75–91.

[39] G. Buntkowsky, M. Vogel, *Molecules* **2020**, *25*, 3311–3342.

[40] S. Zou, C. T. Williams, E. K.-Y. Chen, M. J. Weaver, *J. Am. Chem. Soc.* **1998**, *120*, 3811–3812.

[41] A. R. Hind, S. K. Bhargava, A. McKinnon, *Adv. Colloid. Interface. Sci.* **2001**, *93*, 91–114.

[42] M. Raposo, R. S. Pontes, L. H. C. Mattoso, O. N. Oliveira, *Macromolecules* **1997**, *30*, 6095–6101.

[43] A. G. Serrano, E. J. Cabré, J. M. Oviedo, A. Cruz, B. González, A. Palacios, P. Estrada, J. Pérez-Gil, *Biochim. Biophys. Acta* **2006**, *1758*, 1621–1632.

[44] P. Fenter, N. C. Sturchio, *Prog. Surf. Sci.* **2004**, *77*, 171–258.

[45] C. Alba-Simionesco, G. Dosseh, E. Dumont, B. Frick, B. Geil, D. Morineau, V. Teboul, Y. Xia, *Eur. Phys. J. E* **2003**, *12*, 19–28.

[46] F. Zaera, *Chem. Rev.* **2012**, *112*, 2920–2986.

[47] G. Buntkowsky, S. C. Döller, N. Haro-Mares, T. Gutmann, M. Hoffmann, *Z. Phys. Chem.* **2022**, *236*, 939–960.

[48] S. C. Döller, M. Brodrecht, T. Gutmann, M. Hoffmann, G. Buntkowsky, *J. Phys. Chem. C* **2023**, *127*, 12125–12134.

[49] F. D. Blum, G. Xu, M. Liang, C. G. Wade, *Macromolecules* **1996**, *29*, 8740–8745.

[50] H. Rorschach, C. Hazlewood, *J. Magn. Reson.* **1986**, *70*, 79–88.

[51] M. F. Brown, A. A. Ribeiro, G. D. Williams, *Proc. Natl. Acad. Sci. U.S.A.* **1983**, *80*, 4325–4329.

[52] M. Weigler, E. Winter, B. Kresse, M. Brodrecht, G. Buntkowsky, M. Vogel, *Phys. Chem. Chem. Phys.* **2020**, *22*, 13989–13998.

[53] M. Hoffmann, S. Bothe, T. Gutmann, F.-F. Hartmann, M. Reggelin, G. Buntkowsky, *J. Phys. Chem. C* **2017**, *121*, 2418–2427.

[54] H. Park, B. Uluca-Yazgi, S. Heumann, R. Schlögl, J. Granwehr, H. Heise, P. P. M. Schleker, *J. Magn. Reson.* **2020**, *312*, 106688–106694.

[55] V. Aladin, B. Corzilius, *Solid State Nucl. Magn. Reson.* **2019**, *99*, 27–35.

[56] V. Aladin, M. Vogel, R. Binder, I. Burghardt, B. Suess, B. Corzilius, *Angew. Chem. Int. Ed.* **2019**, *58*, 4863–4868.

[57] V. Aladin, P. A. Trenkler, B. Corzilius, *Exp. Results* **2020**, *1*, 1–8.

[58] D. Zhao, J. Feng, Q. Huo, N. Melosh, G. H. Fredrickson, B. F. Chmelka, G. D. Stucky, *Science* **1998**, *279*, 548–552.

[59] J. S. Beck, J. C. Vartuli, W. J. Roth, M. E. Leonowicz, C. T. Kresge, K. D. Schmitt, C. T. W. Chu, D. H. Olson, E. W. Sheppard, S. B. McCullen, J. B. Higgins, J. L. Schlenker, *J. Am. Chem. Soc.* **1992**, *114*, 10834–10843.

[60] C. T. Kresge, M. E. Leonowicz, W. J. Roth, J. C. Vartuli, J. S. Beck, *Nature* **1992**, *359*, 710–712.

[61] R. A. Jesus, A. S. Rabelo, R. T. Figueiredo, L. C. Da Cides Silva, I. C. Codentino, M. Fantini, G. Araújo, A. Araújo, M. E. Mesquita, *J. Drug Deliv. Sci. Technol.* **2016**, *31*, 153–159.

[62] Z. Li, L. Rösler, T. Wissel, H. Breitzke, T. Gutmann, G. Buntkowsky, *J. CO2 Util.* **2021**, *52*, 101682–101690.

[63] F. Bloch, W. W. Hansen, M. Packard, *Phys. Rev.* **1946**, *69*, 127.

[64] E. M. Purcell, H. C. Torrey, R. V. Pound, *Phys. Rev.* **1945**, *69*, 37–38.

[65] M. J. E. Hewlins, *J. Labelled Compd. Radiopharm.* **1991**, *29*, 861–862.

[66] A. G. Palmer, *Chem. Rev.* **2004**, *104*, 3623–3640.

[67] A. Cavalli, X. Salvatella, C. M. Dobson, M. Vendruscolo, *Proc. Natl. Acad. Sci. U.S.A.* **2007**, *104*, 9615–9620.

[68] J. Mao, V. Aladin, X. Jin, A. J. Leeder, L. J. Brown, R. C. D. Brown, X. He, B. Corzilius, C. Glaubitz, *J. Am. Chem. Soc.* **2019**, *141*, 19888–19901.

[69] A. G. Palmer, H. Koss in *Electron Paramagnetic Resonance Investigations of Biological Systems by Using Spin Labels, Spin Probes, and Intrinsic Metal Ions*, (Eds.: P. Z. Qin, K. Warncke), Methods in enzymology, Elsevier, Amsterdam, **2015**, pp. 177–236.

[70] C. Farès, J. B. Lingnau, C. Wirtz, U. Sternberg, *Molecules* **2019**, *24*, 1–25.

[71] O. Pecher, J. Carretero-González, K. J. Griffith, C. P. Grey, *Chem. Mater.* **2017**, *29*, 213–242.

[72] J. P. de Almeida Martins, C. M. W. Tax, F. Szczepankiewicz, D. K. Jones, C.-F. Westin, D. Topgaard, *Magn. Reson.* **2020**, *1*, 27–43.

[73] A. J. Sim, E. Kaza, L. Singer, S. A. Rosenberg, *Clin. Transl. Radiat. Oncol.* **2020**, *24*, 16–22.

[74] F. Midiri, F. Vernuccio, P. Purpura, P. Alongi, T. V. Bartolotta, *Diagnostics* **2021**, *11*, 1829–1839.

[75] L. M. Janssen, B. M. den Dekker, K. G. A. Gilhuijs, P. J. van Diest, E. van der Wall, S. G. Elias, *NPJ Breast Cancer* **2022**, *8*, 107–113.

[76] K. S. Nayak, Y. Lim, A. E. Campbell-Washburn, J. Steeden, *J. Magn. Reson. Imaging* **2022**, *55*, 81–99.

[77] J. Keeler, *Understanding NMR Spectroscopy*, John Wiley & Sons, Ltd, Hoboken, **2002**.

[78] M. H. Levitt, *Spin Dynamics: Basics of Nuclear Magnetic Resonance*, 2nd edition, Wiley, Chichester, **2008**.

[79] C. P. Slichter, *Principles of Magnetic Resonance*, 3rd edition, Springer, Berlin and Heidelberg, **1990**.

[80] H. Friebolin, *Ein- und Zweidimensionale NMR-Spektroskopie: Eine Einführung*, 5th edition, Wiley-VCH, Weinheim, **2013**.

[81] M. J. Duer, *Solid State NMR Spectroscopy: Principles and Applications*, John Wiley & Sons, Ltd, Hoboken, **2008**.

[82] P. Zeeman, *Nature* **1897**, *55*, 347.

[83] J. B. J. Fourier, *Théorie Analytique de la Chaleur*, Didot, Paris, **1822**.

[84] P. J. McDonald, J.-P. Korb, J. Mitchell, L. Monteilhet, *Phys. Rev. E* **2005**, *72*, 11409–11417.

[85] C. D'Agostino, J. Mitchell, M. D. Mantle, L. F. Gladden, *Chem. Eur. J.* **2014**, *20*, 13009–13015.

[86] S. Rengan, M. Khakhar, B. Prabhananda, B. Venkataraman, *J. Magn. Reson.* **1974**, *16*, 35–43.

[87] E. L. Hahn, *Phys. Rev.* **1950**, *80*, 580–594.

[88] H. Y. Carr, E. M. Purcell, *Phys. Rev.* **1954**, *94*, 630–638.

[89] K. Chen, *Int. J. Mol. Sci.* **2020**, *21*, 5666–5687.

[90] J. E. Gready, *J. Am. Chem. Soc.* **1981**, *103*, 3682–3691.

[91] G. E. Pake, *J. Chem. Phys.* **1948**, *16*, 327–336.

[92] X. Xu, A. V. Struts, M. F. Brown, *eMagRes* **2014**, *3*, 275–286.

[93] J. P. Amoureux, *Solid State Nucl. Magn. Reson.* **1993**, *2*, 83–88.

[94] F. A. Perras, *Pure Appl. Chem.* **2016**, *88*, 95–111.

[95] S. E. Ashbrook, J. McManus, M. J. Thrippleton, S. Wimperis, *Prog. Nucl. Magn. Reson. Spectrosc.* **2009**, *55*, 160–181.

[96] M. Werner, N. Rothermel, H. Breitzke, T. Gutmann, G. Buntkowsky, *Isr. J. Chem.* **2014**, *54*, 60–73.

[97] J. G. Powles, J. H. Strange, *Proc. Phys. Soc.* **1963**, *82*, 6–15.

[98] J. G. Powles, P. Mansfield, *Phys. Lett.* **1962**, *2*, 58–59.

[99] B. Reif, S. E. Ashbrook, L. Emsley, M. Hong, *Nat. Rev. Methods Primers* **2021**, *1*, 1–23.

[100] T. Polenova, R. Gupta, A. Goldbourt, *Anal. Chem.* **2015**, *87*, 5458–5469.

[101] E. R. Andrew, A. Bradbury, R. G. Eades, *Nature* **1958**, *182*, 1659.

[102] A. Pines, M. G. Gibby, J. S. Waugh, *J. Chem. Phys.* **1972**, *56*, 1776–1777.

[103] F. A. L. Anet, A. J. R. Bourn, *J. Am. Chem. Soc.* **1965**, *87*, 5250–5251.

[104] S. R. Hartmann, E. L. Hahn, *Phys. Rev.* **1962**, *128*, 2042–2053.

[105] J. Schaefer, E. O. Stejskal, R. Buchdahl, *Macromolecules* **1975**, *8*, 291–296.

[106] G. Metz, X. L. Wu, S. O. Smith, *J. Magn. Reson. A* **1994**, *110*, 219–227.

[107] I. Ben Shir, S. Kababya, A. Schmidt, *J. Phys. Chem. C* **2012**, *116*, 9691–9702.

[108] B. Kumari, M. Brodrecht, H. Breitzke, M. Werner, B. Grünberg, H.-H. Limbach, S. Forg, E. P. Sanjon, B. Drossel, T. Gutmann, G. Buntkowsky, *J. Phys. Chem. C* **2018**, *122*, 19540–19550.

[109] J. Trebosc, J. W. Wiench, S. Huh, V. S.-Y. Lin, M. Pruski, *J. Am. Chem. Soc.* **2005**, *127*, 7587–7593.

[110] J. W. Wiench, Y. S. Avadhut, N. Maity, S. Bhaduri, G. K. Lahiri, M. Pruski, S. Ganapathy, *J. Phys. Chem. B* **2007**, *111*, 3877–3885.

[111] P. B. Groszewicz, P. Mendes, B. Kumari, J. Lins, M. Biesalski, T. Gutmann, G. Buntkowsky, *Cellulose* **2020**, *27*, 1239–1254.

[112] A. A. Maudsley, R. R. Ernst, *Chem. Phys. Lett.* **1977**, *50*, 368–372.

[113] J. Farjon, W. Bermel, C. Griesinger, *J. Mag. Res.* **2006**, *180*, 72–82.

[114] M. Lee, W. I. Goldburg, *Phys. Rev.* **1965**, *140*, A1261–A1271.

[115] B.-J. van Rossum, H. Förster, H. de Groot, *J. Mag. Res.* **1997**, *124*, 516–519.

[116] A. Abraham, G. Crull, *Mol. Pharmaceutics* **2014**, *11*, 3754–3759.

[117] M. E. Halse, *Trends Anal. Chem.* **2016**, *83*, 76–83.

[118] T. Biedenbänder, V. Aladin, S. Saeidpour, B. Corzilius, *Chem. Rev.* **2022**, *122*, 9738–9794.

[119] G. A. Morris, R. Freeman, *J. Am. Chem. Soc.* **1979**, *101*, 760–762.

[120] A. Hassan, C. M. Quinn, J. Struppe, I. V. Sergeyev, C. Zhang, C. Guo, B. Runge, T. Theint, H. H. Dao, C. P. Jaroniec, M. Berbon, A. Lends, B. Habenstein, A. Loquet, R. Kuemmerle, B. Perrone, A. M. Gronenborn, T. Polenova, *J. Magn. Reson.* **2020**, *311*, 106680–106690.

[121] K. Takeda, *Solid State Nucl. Magn. Reson.* **2012**, *47-48*, 1–9.

[122] J. Natterer, J. Bargon, *Prog. Nucl. Magn. Reson. Spectrosc.* **1997**, *31*, 293–315.

[123] P. F. Seidler, H. E. Bryndza, J. E. Frommer, L. S. Stuhl, R. G. Bergman, *Organometallics* **1983**, *2*, 1701–1705.

[124] C. R. Bowers, D. P. Weitekamp, *Phys. Rev. Lett.* **1986**, *57*, 2645–2648.

[125] T. C. Eisenschmid, R. U. Kirss, P. P. Deutsch, S. I. Hommeltoft, R. Eisenberg, J. Bargon, R. G. Lawler, A. L. Balch, *J. Am. Chem. Soc.* **1987**, *109*, 8089–8091.

[126] C. R. Bowers, D. P. Weitekamp, *J. Am. Chem. Soc.* **1987**, *109*, 5541–5542.

[127] G. Buntkowsky, B. Walaszek, A. Adamczyk, Y. Xu, H.-H. Limbach, B. Chaudret, *Phys. Chem. Chem. Phys.* **2006**, *8*, 1929–1935.

[128] R. A. Green, R. W. Adams, S. B. Duckett, R. E. Mewis, D. C. Williamson, G. G. R. Green, *Prog. Nucl. Magn. Reson. Spectrosc.* **2012**, *67*, 1–48.

[129] S. Wagner, *Magn. Reson. Mater. Phy.* **2014**, *27*, 195–199.

[130] G. Buntkowsky, F. Theiss, J. Lins, Y. A. Miloslavina, L. Wienands, A. Kiryutin, A. Yurkovskaya, *RSC Adv.* **2022**, *12*, 12477–12506.

[131] S. B. Duckett, C. L. Newell, R. Eisenberg, *J. Am. Chem. Soc.* **1993**, *115*, 1156–1157.

[132] S. E. Korchak, K. L. Ivanov, A. V. Yurkovskaya, H.-M. Vieth, *Phys. Chem. Chem. Phys.* **2009**, *11*, 11146–11156.

[133] P. J. Carson, C. R. Bowers, D. P. Weitekamp, *J. Am. Chem. Soc.* **2001**, *123*, 11821–11822.

[134] T. Ratajczyk, T. Gutmann, S. Dillenberger, S. Abdulhussaein, J. Frydel, H. Breitzke, U. Bommerich, T. Trantzschel, J. Bernarding, P. C. M. M. Magusin, G. Buntkowsky, *Solid State Nucl. Magn. Reson.* **2012**, *43-44*, 14–21.

[135] G. Buntkowsky, T. Gutmann, M. V. Petrova, K. L. Ivanov, U. Bommerich, M. Plaumann, J. Bernarding, *Solid State Nucl. Magn. Reson.* **2014**, *63-64*, 20–29.

[136] R. W. Adams, J. A. Aguilar, K. D. Atkinson, M. J. Cowley, P. I. P. Elliott, S. B. Duckett, G. G. R. Green, I. G. Khazal, J. López-Serrano, D. C. Williamson, *Science* **2009**, *323*, 1708–1711.

[137] T. Theis, M. L. Truong, A. M. Coffey, R. V. Shchepin, K. W. Waddell, F. Shi, B. M. Goodson, W. S. Warren, E. Y. Chekmenev, *J. Am. Chem. Soc.* **2015**, *137*, 1404–1407.

[138] T. Theis, M. Truong, A. M. Coffey, E. Y. Chekmenev, W. S. Warren, *J. Magn. Reson.* **2014**, *248*, 23–26.

[139] F. Shi, A. M. Coffey, K. W. Waddell, E. Y. Chekmenev, B. M. Goodson, **2014**, *53*, 7495–7498.

[140] T. G. Walker, W. Happer, *Rev. Mod. Phys.* **1997**, *69*, 629–642.

[141] M. S. Albert, G. D. Cates, B. Driehuys, W. Happer, B. Saam, C. S. Springer, A. Wishnia, *Nature* **1994**, *370*, 199–201.

[142] A. L. Kern, J. Vogel-Claussen, *Br. J. Radiol.* **2018**, *91*, 20170647–20170662.

[143] J. Demarquay, J. Fraissard, *Chem. Phys. Lett.* **1987**, *136*, 314–318.

[144] V. V. Terskikh, I. L. Mudrakovskii, V. M. Mastikhin, *J. Chem. Soc. Faraday Trans.* **1993**, *89*, 4239–4243.

[145] K. J. Ooms, R. E. Wasylishen, *Microporous Mesoporous Mater.* **2007**, *103*, 341–351.

[146] K. V. Romanenko, X. Py, J.-B. d'Espinose de Lacaillerie, O. B. Lapina, J. Fraissard, *J. Phys. Chem. B* **2006**, *110*, 3055–3060.

[147] J. Bargon, H. Fischer, U. Johnsen, *Z. Naturforsch. A* **1967**, *22*, 1551–1555.

[148] G. L. Closs, L. E. Closs, *J. Am. Chem. Soc.* **1969**, *91*, 4549–4550.

[149] R. Kaptein, J. L. Oosterhoff, *Chem. Phys. Lett.* **1969**, *4*, 195–197.

[150] J. Hore, R. W. Broadhurst, *Prog. Nucl. Magn. Reson. Spectrosc.* **1993**, *25*, 345–402.

[151] E. Duynstee, M. L. Esser, R. Schellekens, **1980**, *16*, 1127–1134.

[152] R. Kaptein in *Biological Magnetic Resonance*, (Eds.: L. J. Berliner, J. Reuben), Biological Magnetic Resonance, Springer, New York, **1982**, pp. 145–191.

[153] G. Gitlin, I. Khait, E. A. Bayer, M. Wilchek, K. A. Muszkat, *Biochem. J.* **1989**, *259*, 493–498.

[154] M. Goez, *Top. Curr. Chem.* **2013**, *338*, 1–32.

[155] M. Najdanova, G. J. Janssen, H. J. M. de Groot, J. Matysik, A. Alia, **2015**, *152*, 261–271.

[156] X.-J. Wang, S. S. Thamarath, A. Alia, B. E. Bode, J. Matysik, *Acta Phys. Chim. Sin.* **2016**, *32*, 399–404.

[157] S. S. Thamarath, A. Alia, E. Roy, K. B. Sai Sankar Gupta, J. H. Golbeck, J. Matysik, *Photosynth. Res.* **2013**, *117*, 461–469.

[158] S. S. Thamarath, B. E. Bode, S. Prakash, K. B. Sai Sankar Gupta, A. Alia, G. Jeschke, J. Matysik, *J. Am. Chem. Soc.* **2012**, *134*, 5921–5930.

[159] T. R. Carver, C. P. Slichter, *Phys. Rev.* **1953**, *92*, 212–213.

[160] A. W. Overhauser, *Phys. Rev.* **1953**, *92*, 411–415.

[161] H. G. Beljers, L. van der Kint, J. S. van Wieringen, *Phys. Rev.* **1954**, *95*, 1683.

[162] R. A. Wind, M. J. Duijvestijn, C. van der Lugt, A. Manenschijn, J. Vriend, *Prog. Nucl. Magn. Reson. Spectrosc.* **1985**, *17*, 33–67.

[163] L. R. Becerra, G. J. Gerfen, R. J. Temkin, D. J. Singel, R. G. Griffin, *Phys. Rev. Lett.* **1993**, *71*, 3561–3564.

[164] G. J. Gerfen, L. R. Becerra, D. A. Hall, R. G. Griffin, R. J. Temkin, D. J. Singel, *J. Chem. Phys.* **1995**, *102*, 9494–9497.

[165] B. Plainchont, P. Berruyer, J.-N. Dumez, S. Jannin, P. Giraudeau, *Anal. Chem.* **2018**, *90*, 3639–3650.

[166] C. Sauvée, M. Rosay, G. Casano, F. Aussenac, R. T. Weber, O. Ouari, P. Tordo, *Angew. Chem. Int. Ed.* **2013**, *52*, 10858–10861.

[167] C. Song, K.-N. Hu, C.-G. Joo, T. M. Swager, R. G. Griffin, *J. Am. Chem. Soc.* **2006**, *128*, 11385–11390.

[168] O. Haze, B. Corzilius, A. A. Smith, R. G. Griffin, T. M. Swager, *J. Am. Chem. Soc.* **2012**, *134*, 14287–14290.

[169] M. K. Kiesewetter, B. Corzilius, A. A. Smith, R. G. Griffin, T. M. Swager, *J. Am. Chem. Soc.* **2012**, *134*, 4537–4540.

[170] M. Abraham, M. A. H. McCausland, F. N. H. Robinson, *Phys. Rev. Lett.* **1959**, *2*, 449–451.

[171] B. Corzilius, *eMagRes* **2018**, *7*, 179–194.

[172] S. Hediger, D. Lee, F. Mentink-Vigier, G. De Paëpe, *eMagRes* **2018**, *7*, 105–116.

[173] B. Corzilius, *Annu. Rev. Phys. Chem.* **2020**, *71*, 143–170.

[174] K. R. Thurber, R. Tycko, *J. Chem. Phys.* **2012**, *137*, 084508–084521.

[175] F. Mentink-Vigier, Ü. Akbey, H. Oschkinat, S. Vega, A. Feintuch, *J. Magn. Reson.* **2015**, *258*, 102–120.

[176] T. R. Carver, C. P. Slichter, *Phys. Rev.* **1956**, *102*, 975–980.

[177] A. S. Lilly Thankamony, J. J. Wittmann, M. Kaushik, B. Corzilius, *Prog. Nucl. Magn. Reson. Spectrosc.* **2017**, *102-103*, 120–195.

[178] D. Yoon, A. I. Dimitriadis, M. Soundararajan, C. Caspers, J. Genoud, S. Alberti, E. de Rijk, J.-P. Ansermet, *Anal. Chem.* **2018**, *90*, 5620–5626.

[179] D. Dai, X. Wang, Y. Liu, X.-L. Yang, C. Glaubitz, V. Denysenkov, X. He, T. Prisner, J. Mao, *Nat. Commun.* **2021**, *12*, 6880–6894.

[180] T. Orlando, R. Dervişoğlu, M. Levien, I. Tkach, T. F. Prisner, L. B. Andreas, V. P. Denysenkov, M. Bennati, *Angew. Chem. Int. Ed.* **2019**, *58*, 1402–1406.

[181] T. Dubroca, S. Wi, J. van Tol, L. Frydman, S. Hill, *Phys. Chem. Chem. Phys.* **2019**, *21*, 21200–21204.

[182] T. Prisner, V. Denysenkov, D. Sezer, *J. Magn. Reson.* **2016**, *264*, 68–77.

[183] D. Sezer, *Phys. Chem. Chem. Phys.* **2014**, *16*, 1022–1032.

[184] I. Solomon, *Phys. Rev.* **1955**, *99*, 559–565.

[185] P. Neugebauer, J. G. Krummenacker, V. P. Denysenkov, G. Parigi, C. Luchinat, T. F. Prisner, *Phys. Chem. Chem. Phys.* **2013**, *15*, 6049–6056.

[186] C. D. Jeffries, *Phys. Rev.* **1957**, *106*, 164–165.

[187] J. Uebersfeld, J. L. Motchane, E. Erb, *J. Phys. Radium* **1958**, *19*, 843–844.

[188] K. Herr, M. Fleckenstein, M. Brodrecht, M. V. Höfler, H. Heise, F. Aussenac, T. Gutmann, M. Reggelin, G. Buntkowsky, *Sci. Rep.* **2021**, *11*, 13714–13725.

[189] B. Corzilius, *Phys. Chem. Chem. Phys.* **2016**, *18*, 27190–27204.

[190] M. Jorgensen, F. Rise, S. Andersson, T. Almen, A. Aabye, L. G. Wistrand, H. Wikstroem, K. Golman, R. Servin, P. Michelsen, *pat.*, EP0515458 (A1), **1992**.

[191] T. V. Can, Q. Z. Ni, R. G. Griffin, *J. Magn. Reson.* **2015**, *253*, 23–35.

[192] D. Wisser, G. Karthikeyan, A. Lund, G. Casano, H. Karoui, M. Yulikov, G. Menzildjian, A. C. Pinon, A. Purea, F. Engelke, S. R. Chaudhari, D. Kubicki, A. J. Rossini, I. B. Moroz, D. Gajan, C. Copéret, G. Jeschke, M. Lelli, L. Emsley, A. Lesage, O. Ouari, *J. Am. Chem. Soc.* **2018**, *140*, 13340–13349.

[193] U. Akbey, W. T. Franks, A. Linden, M. Orwick-Rydmark, S. Lange, H. Oschkinat, *Top. Curr. Chem.* **2013**, *338*, 181–228.

[194] A. V. Kessenikh, V. I. Lushchikov, A. A. Manenkov, Y. V. Taran, *Soviet Phys. Solid State (English Transl.)* **1963**, *5*, 321–329.

[195] A. V. Kessenikh, A. A. Manenkov, G. I. Pyatnitskii, *Soviet Phys. Solid State (English Transl.)* **1964**, *6*, 827–830.

[196] D. S. Wollan, *Phys. Rev. B* **1976**, *13*, 3671–3685.

[197] D. S. Wollan, *Phys. Rev. B* **1976**, *13*, 3686–3696.

[198] Y. Matsuki, T. Maly, O. Ouari, H. Karoui, F. Le Moigne, E. Rizzato, S. Lyubenova, J. Herzfeld, T. Prisner, P. Tordo, R. G. Griffin, *Angew. Chem. Int. Ed.* **2009**, *48*, 4996–5000.

[199] A. Zagdoun, G. Casano, O. Ouari, M. Schwarzwälder, A. J. Rossini, F. Aussenac, M. Yulikov, G. Jeschke, C. Copéret, A. Lesage, P. Tordo, L. Emsley, *J. Am. Chem. Soc.* **2013**, *135*, 12790–12797.

[200] M. Kaushik, M. Qi, A. Godt, B. Corzilius, *Angew. Chem. Int. Ed.* **2017**, *56*, 4295–4299.

[201] C. T. Farrar, D. A. Hall, G. J. Gerfen, S. J. Inati, R. G. Griffin, *J. Chem. Phys.* **2001**, *114*, 4922–4933.

[202] D. Daube, V. Aladin, J. Heiliger, J. J. Wittmann, D. Barthelmes, C. Bengs, H. Schwalbe, B. Corzilius, *J. Am. Chem. Soc.* **2016**, *138*, 16572–16575.

[203] M. Hoffmann, S. Bothe, T. Gutmann, G. Buntkowsky, *J. Phys. Chem. C* **2017**, *121*, 22948–22957.

[204] F. Palombo, P. Sassi, M. Paolantoni, A. Morresi, R. S. Cataliotti, *J. Phys. Chem. B* **2006**, *110*, 18017–18025.

[205] C. L. Jackson, G. B. McKenna, *J. Chem. Phys.* **1990**, *93*, 9002–9011.

[206] E. Rössler, M. Taupitz, K. Börner, M. Schulz, H.-M. Vieth, *J. Chem. Phys.* **1990**, *92*, 5847–5855.

[207] E. S. Salnikov, S. Abel, G. Karthikeyan, H. Karoui, F. Aussenac, P. Tordo, B. Bechinger, O. Ouari, *ChemPhysChem* **2017**, *18*, 2103–2113.

[208] D. Gauto, O. Dakhlaoui, I. Marin-Montesinos, S. Hediger, G. de Paëpe, *Chem. Sci.* **2021**, *12*, 6223–6237.

[209] B. Oberg, *Antiviral Res.* **2006**, *71*, 90–95.

[210] I. V. Sergeyev, C. M. Quinn, J. Struppe, A. Gronenborn, T. Polenova, *Magn. Reson.* **2021**, *2*, 239–249.

[211] C. A. F. de Oliveira, C. R. W. Guimares, R. B. de Alencastro, *Int. J. Quantum Chem.* **2000**, *80*, 999–1006.

[212] M. Hoffmann, S. Bothe, M. Brodrecht, V. Klimavicius, N. B. Haro-Mares, T. Gutmann, G. Buntkowsky, *J. Phys. Chem. C* **2020**, *124*, 5145–5156.

[213] M. Kruk, M. Jaroniec, C. H. Ko, R. Ryoo, *Chem. Mater.* **2000**, *12*, 1961–1968.

[214] M. de Oliveira, Jr., K. Herr, M. Brodrecht, N. B. Haro-Mares, T. Wissel, V. Klimavicius, H. Breitzke, T. Gutmann, G. Buntkowsky, *Phys. Chem. Chem. Phys.* **2021**, *23*, 12559–12568.

List of Abbreviations

Abbreviation	Description	Unit
α	Spin state alpha	
B_0	External magnetic field	T
B_1	Oscillating magnetic field	T
β	Spin state beta	
CE	Cross effect	
CIDNP	Chemically Induced Dynamic Nuclear Polarization	
CP	Cross polarization	
C_Q	Quadrupolar coupling constant	Hz
CR	Cross relaxation	
δ	Electron Paramagnetic Resonance transition line width	
δ_σ	Chemical shielding anisotropy	
DNP	Dynamic Nuclear Polarization	
DQ	Double quantum	
DSC	Differential Scanning Calorimetry	
E	Energy	J
e	Elementary charge	C
EDS	Electron dipolar system	
EFG	Electric field gradient	V m^{-2}
EPR	Electron Paramagnetic Resonance	
ϵ	Enhancement factor	
eQ	Nuclear quadrupole moment	C m^2
η	Asymmetry parameter	
η_σ	Chemical shielding asymmetry	
EZS	Electron Zeeman system	
f	Leakage factor	
FID	Free induction decay	
FSLG	Frequency-switched Lee-Goldburg	
γ	Gyromagnetic ratio	rad s^{-1} T^{-1}
$\mathcal{H}$	Hamiltonian	
$\hbar$	Reduced Planck constant	J s^{-1}
HETCOR	Heteronuclear Correlation	
HFI	Hyperfine interaction	
INEPT	Insensitive Nuclei Enhancement by Polarization Transfer	
k_B	Boltzmann constant	J K^{-1}
LG	Lee-Goldburg	
LN_2	Liquid nitrogen	
M	Magnetization	

Abbreviation	Description	Unit
MAS	Magic angle spinning	
MCM	Mobil Composition of Matter	
MD	Molecular dynamics	
MRI	Magnetic Resonance Imaging	
μ_0	Vacuum permeability	kg m s^{-2} A^{-2}
µw	Microwave	
NOE	Nuclear Overhauser Effect	
NZS	Nuclear Zeeman system	
OE	Overhauser effect	
ω	Frequency	Hz
P	Polarization	
PA	Polarizing agent	
PEG	Polyethylene glycol	
ϕ	Angle phi	°
PHIP	Parahydrogen Induced Polarization	
PMS	Periodic mesoporous silica	
q	Charge	C
r	Distance	m
RF	Radio frequency	
s	Saturation factor	
SABRE	Signal Amplification by Reversible Exchange	
SBA	Santa Barbara Amorphous	
SCREAM	Specific Cross Relaxation Enhancement by Active Motions	
SE	Solid effect	
SEOP	Spin-Exchange Optical Pumping	
σ_{iso}	Isotropic chemical shielding	
SQ	Single quantum	
ssNMR	Solid-state Nuclear Magnetic Resonance	
T	Temperature	K
t_{d}	Dead time	s
T_1	Spin-lattice or longitudinal relaxation time constant	s
T_2	Spin-spin or transversal relaxation time constant	s
τ	Incremental period in a pulse sequence	s
θ	Angle theta	°
θ_{M}	Magic angle	°
TM	Thermal mixing	
Triton	Triton X-100	
UV/Vis	Ultraviolet/visible	
V	Electrical field gradient tensor	
W_{i}	Probability for transition i	
ξ	Coupling factor	
ZQ	Zero quantum	

Erklärung zum Eigenanteil an den Veröffentlichungen

Im Folgenden ist aufgelistet, mit welchem Anteil ich an den Veröffentlichungen beteiligt war.

Mein Anteil an der folgenden Veröffentlichung beträgt 90 %.

S. C. Döller, M. Brodrecht, N. B. Haro Mares, H. Breitzke, T. Gutmann, M. Hoffmann and G. Buntkowsky, *J. Phys. Chem. C*, **2021**, *125*, 25155–25164.

Mein Anteil an der folgenden Veröffentlichung beträgt 100 %.

S. C. Döller, T. Gutmann, M. Hoffmann and G. Buntkowsky, *Solid State Nucl. Magn. Reson.*, **2022**, *122*, 101829–101837.

Mein Anteil an der folgenden Veröffentlichung beträgt 90 %.

S. C. Döller, M. Brodrecht, T. Gutmann, M. Hoffmann and G. Buntkowsky, *J. Phys. Chem. C*, **2023**, *127*, 12125–12134.

Ort, Datum

Sonja Carina Döller

Erklärung zur Begutachtung der Veröffentlichungen

Weder Referent (Prof. Dr. Gerd Buntkowsky) noch Co-Referent (apl. Prof. Dr. Torsten Gutmann) der vorliegenden kumulativen Doktorarbeit waren an der Begutachtung der nachfolgenden Veröffentlichungen beteiligt:

1. S. C. Döller, M. Brodrecht, T. Gutmann, M. Hoffmann and G. Buntkowsky, *J. Phys. Chem. C*, **2023**, *127*, 12125–12134.
2. S. C. Döller, T. Gutmann, M. Hoffmann and G. Buntkowsky, *Solid State Nucl. Magn. Reson.*, **2022**, *122*, 101829–101837.
3. S. C. Döller, M. Brodrecht, T. Gutmann, M. Hoffmann and G. Buntkowsky, *J. Phys. Chem. C*, **2023**, *127*, 12125–12134.

Datum: _____

Referent Prof. Dr. Gerd Buntkowsky	Co-Referent apl. Prof. Dr. Torsten Gutmann